The Use of 3D-Printing in the Study of Chromatographic Packed Bed Microstructures

A thesis submitted in partial fulfilment of the requirements for the degree of

Doctor of Philosophy in Chemical and Process Engineering

University of Canterbury

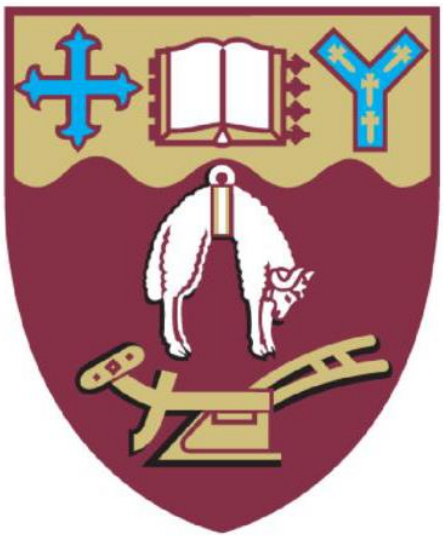

Written by

Suhas H. Nawada

Department of Chemical and Process Engineering,

University of Canterbury,

Christchurch, New Zealand

2018

Abstract

Liquid chromatographic separations are typically performed in cylindrical columns with a random packing of spherical beads. The emergence of additive manufacturing, or 3D-printing has meant that novel column geometries can be printed to minimize band-broadening. Porous beds with perfectly ordered micro-structures, novel flow-distributor and column housing designs can be reliably manufactured achieve more efficient separations. This thesis investigates the effects of 3D-printed column mico-structures on a column's plate height.

First, the thesis describes the manufacturing and testing of proof-of-principle 3D-printed columns consisting of ordered porous beds, column walls, flow distributors, collectors and standard liquid chromatography fittings in a single printed artefact. Porous bed structures based on channels and particle-like elements were tested with radial and fractal distributor layouts, with the fractal distributor significantly reducing in the channel based geometries. Within particle-like elements, the effects of bed porosity, element shape and arrangement were tested using printed models.

Additionally, the effects of defects in porous beds were quantified by deliberately introducing well defined line defects into the bed design and experimentally testing the residence time distribution profiles. The penultimate chapter describes a set of geometries known as triply periodic minimal surfaces (TPMS) that were printed and experimentally tested. Monolithic structures known as network TPMS were shown to out-perform the best sphere packing column in minimizing band-broadening and flow resistance.

To the best of my knowledge, the work presented here represent the first steps towards 3D-printed liquid chromatography columns. The adoption of 3D-printing as a column production method is currently limited by several key challenges such as resolution, material choice and print times. However, the methods and results reported here can serve as a foundation for future research, in particular in developing and testing more effective porous bed micro-structures.

Acknowledgements

First and foremost, I would like to thank the Biomolecular Interaction Centre and New Zealand's Ministry of Business, Innovation and Employment for funding this work.

I would like to thank my supervisor, Dr. Simone Dimartino for the numerous stimulating discussions and creative ideas. I am also immensely grateful for all the help and encouragement that the technical staff has provided over the years: Rayleen Fredericks-Short for all her help, patience and encouragement in the lab. Bruce Sparks of the Ara Institute, Christchurch and Dave Read in UC's mechanical engineering department for all their help with operating and maintaining the 3D-printers that made this project possible. Manfred Ingerfeld for help on microscopy and philosophical discussions.

Thank you to my friends, family and my partner Michelle for supporting me in numerous ways during this rather satisfying and eventful journey. Finally, and most importantly, I would like to thank my senior supervisor Prof. Conan Fee for encouraging and supporting me every step of the way during and after my studies in Canterbury.

UNIVERSITY OF CANTERBURY
Te Whare Wānanga o Waitaha
CHRISTCHURCH NEW ZEALAND

Deputy Vice-Chancellor's Office
Postgraduate Office

Co-Authorship Form

This form is to accompany the submission of any thesis that contains research reported in co-authored work that has been published, accepted for publication, or submitted for publication. A copy of this form should be included for each co-authored work that is included in the thesis. Completed forms should be included at the front (after the thesis abstract) of each copy of the thesis submitted for examination and library deposit.

Please indicate the chapter/section/pages of this thesis that are extracted from co-authored work and provide details of the publication or submission from the extract comes:

1. Chapter 2: Fee, C., Nawada, S. & Dimartino, S. 3D printed porous media columns with fine control of column packing morphology. Journal of Chromatography A 1333, (2014)

2. Chapter 3.1: Nawada, S., Dimartino, S. & Fee, C. The effects of bead overlap on chromatographic performance in 3D printed packed bed columns. Chromatography Today (2014). (Non peer-reviewed journal)

3. Chapter 3.3 and 3.4: Nawada, S., Dimartino, S. & Fee, C. Dispersion behavior of 3D-printed columns with homogeneous microstructures comprising differing element shapes. Chemical Engineering Science 164, (2017).

Please detail the nature and extent (%) of contribution by the candidate:

1. All of the design and experimental work was carried out by the candidate. Drafting of the paper was carried out by co-authors with substantial contributions to the manuscript by the candidate.

2,3. Design and experiments were carried out by the candidate, with revisions of the manuscripts by the co-authors

Certification by Co-authors:

If there is more than one co-author then a single co-author can sign on behalf of all
The undersigned certifys that:

- The above statement correctly reflects the nature and extent of the PhD candidate's contribution to this co-authored work
- In cases where the candidate was the lead author of the co-authored work he or she wrote the text

Name:	Signature:	Date:

Nomenclature

Symbol	Definition
Φ	Flow resistance
Θ	Dimensionless flow volume
μ_1	First moment, mean residence time or volume [m]
α	Particle overlap factor
$\Delta\varepsilon_{CS}$	Cross-sectional porosity difference
ε	Extra-particle porosity
λ	Carman-kozeny empirical constant
σ^2	Second moment, variance [m^2]
τ	Tortuosity
γ_1	Dimensionless peak skewness
Ψ	Wadell sphericity
b	Voxel length [m]
C	Circularity
cfs	Number of connecting faces for solid voxels
cfv	Number of connecting faces for void voxels
D_E	Equivalent diameter [m]
D_H	Hydraulic diameter [m]
d_p	Particle diameter [m]
E	Separation impedence
E_{min}	Minimum separation impedence
e_b	Relative build error
h	Reduced plate height
h_{min}	Minimum reduced plate height
L_U	Unit-cell length [m]
m	Iso-value denoting wall thickness in sheet minimal surfaces
nsf	Nearest surface function
$Pe = v$	Peclet number or reduced velocity
PD	Porosity difference [%]
S	Specific surface area
t	Iso-value in network triply periodic minimal surfaces

u	Superficial velocity [m/s]
v_c	Channel velocity [m/s]
v_b	Bed velocity [m/s]
V_{VOID}	Bed void volume [m^3]

Abbreviation	**Definition**
2PP	Two-photon polymerization
A-Term	Eddy diffusion term in the Van-Deemter equation
BCC	Body-centered cubic arrangement
B-Term	Longitudinal diffusion term in the Van-Deemter equation
CFD	Computational fluid dynamics
C-Term	Mass-transfer term in the Van-Deemter equation
DBR	Discrete bead removal line defect
DLP	Digital light processing
ET	Embedded tube defect
FCC	Face-centered cubic arrangement
FPLC	Fast protein liquid chromatography
HC	Herringbone channel column
HPLC	High performance liquid chromatography
i3DP	Inkjet 3D-printing
LBM	Lattice-boltzmann method
LC	Liquid chromatography
LOM	Laminated object manufacturing
MEMS	Micro-electoremechanical systems
PµSL	Projection microstereolithography
PC	Parallel channel
SC	Simple cubic
SCS	Square cross-section defect
SD	Schwartz diamond
SLA	Stereolithograhy
SLM	Selective laser melting
SP	Schwartz primitive
TD	Tube defect
TPMS	Triply periodic minimal surfaces

List of Figures

List of Tables

Table of Contents

1. Introduction

1.1 Outline

This thesis describes initial work on producing liquid chromatography columns using additive manufacturing, or 3D-printing. The central advantage that this technology provides is the ability to create entirely ordered porous structures as stationary phases, as opposed to random packed columns that currently dominate the field. Chapter 1 gives a general introduction to liquid chromatography, previous computational and experimental studies on ordered stationary phases and a brief overview of state-of-the-art 3D-printing techniques, as of 2018.

Chapter 2 contains the initial proof-of-principle work in building fully 3D-printed chromatography columns with stationary phases and ancillary elements. Particle and channel based porous beds were printed and tested with two different flow distributor layouts. To the best of my knowledge, this remains the first reported use of 3D-printing in liquid chromatography. Chapter 3 investigates several aspects of ordered packed beds, namely porosity (by controlling the extent of particle overlap), arrangement and element shape.

Chapter 4 describes tests performed on columns with deliberately introduced linear defects in an ordered arrangement of elements, with the effects on column performance across a range of element and defect shapes being tested. Chapter 5 explores a category of geometries known as triply periodic minimal surfaces to create monolithic structures as the printed porous beds. The final chapter contains a set of recommendations for future research involving printing rationally designed voxel arrangements, including a set of structures defined by cellular automata.

The body of work reported here does not represent an exhaustive or complete investigation of the effects of stationary phase micro-structure using 3D-printing. Rather, these are the first steps to creating favourable geometries for facilitating more efficient chromatographic separations and exploiting the immense potential that 3D-printing offers in this field.

1.2 Liquid Chromatography and Stationary Phase Geometries

1.2.1 Liquid Chromatography and Band-Broadening

For more than a half a century, liquid chromatography has been one of the most common methods of separating mixtures of compounds. A typical LC system consists of a high-pressure pump to flow the mobile phase, an injection valve, an LC column packed with a stationary phase and a detector[1,2]. A small sample volume is typically injected through an injection valve to the column. The mixture is then separated based on its retention to the stationary phase and elute at different times. The eluents from the column can then be detected using a variety of options such as UV-absorbance, diode Array, conductivity detectors or from a range of mass spectrometric detectors.

These basic principles are applied across a wide range of applications, from analytical scale separations for proteomics with columns under 1 µL to large-scale downstream processing of fermentation products in columns larger than 1 L[1,3]. The central part of the process across all column volumes and applications is the interaction between the mobile and stationary phases within the chromatography column. Typically, a cylindrical column is slurry packed to form a random packing arrangement of particles[4].

For analytical separations, the performance of a column and method is the number of peaks that a method can resolve in a given time-frame[5]. For the purification of a single compound in preparative chromatography, the performance of a process is measured by its yield and recovery[6]. In both cases, lower plate heights, back-pressures and separation times are desirable and are constantly sought.

Martin and Synge developed a model where a column could be imagined as a series of plates in a distillation column[7]. The efficiency of a chromatography column could thus be quantified by the number of plates[8], *N*, or the height of a theoretical plate, *H*. The plate height can be calculated by calculating the first and second moments of the gaussian profile of a tracer that is injected through the column:

$$H = L \frac{\sigma^2}{\mu_1^2}$$

Eq 1.1

where μ_1 and σ^2 are the first and second moments of the tracer curve. To compare columns with differing characteristic dimensions and solvents, Giddings introduced a reduced plate height h [9]

$$h = \frac{H}{d_p}$$

Eq 1.2

where d_p is the particle diameter. The non-dimensionalized superficial velocity through the column is known as the reduced velocity v or the Peclet number, Pe:

$$v = Pe = \frac{u.d_p}{D_m}$$

Eq 1.3

where u is the superficial velocity of the mobile phase. The pressure drop, ΔP, caused by the mobile phase moving through the column can be described using Darcy's law:

$$\Delta P = \frac{u.\ \eta.\ L}{k}$$

Eq 1.4

based on the column length L, mobile phase viscosity η and column permeability k. The relation of particle diameter d_p on permeability can be described using a term for flow resistance φ:

$$\varphi = \frac{d_p^2}{k}$$

Eq 1.5

A standard method to gauge the performance of a column and the quality of the packing is to measure the column's plate heights across a range of velocities. Figure 1.1 shows a typical curve for a chromatography column. In 1956, Van Deemter et al.[10] postulated that the relation of plate height to velocities could be described with three terms:

- A-Term: A constant, velocity-independent metric based on the heterogeneity of packing structures.
- B-Term: Caused by molecular diffusion and is therefore less relevant at higher velocities. The B-term is therefore inversely proportional to the flow velocity.
- C-Term: A parameter that is directly proportional to flow velocity and is caused by limited mass transfer between the stationary and mobile phases.

Because the three causes of band-broadening are additive, the non-dimensional version of the Van Deemter equation is as follows:

$$h = A + \frac{B}{v} + C.v$$

Eq 1.6

The six decades after this first description has seen numerous variants of the Van Deemter equation, the most crucial equations described by Giddings[9], Knox[11] and Horvath and Lin[12]. In all models, the A-term and to a lesser extent, the C-term is determined by the heterogeneities caused by flow through a non-ideal porous structure. The term for flow resistance φ is also an empirical, dimensionless term that is based on the resistance to flow that a porous structure provides.

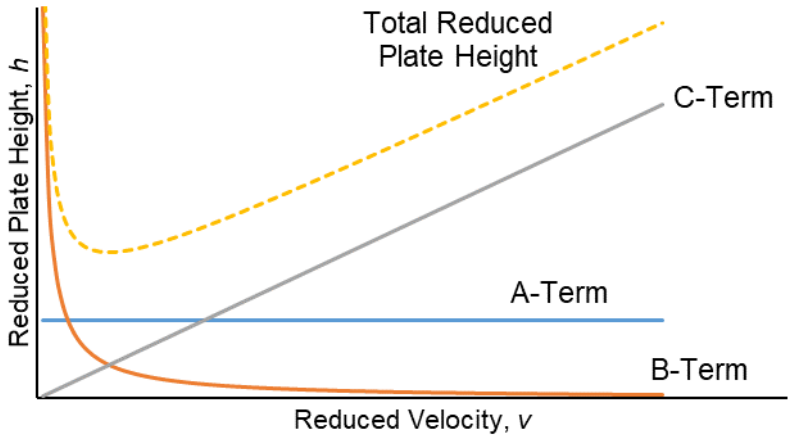

Figure 1.1: Van-Deemter plot showing A, B and C term contributions

Optimizing the packing and its resultant pore structure is therefore a crucial part of creating more efficient liquid chromatography columns. This chapter provides a summary of computational and experimental research on the effects of ordered and random stationary phase geometries. It then covers the current (i.e. 2018) state-of-the-art in 3D-printing technologies and their prospective abilities to produce chromatographic stationary phases.

1.2.2 Effects of Stationary Phase Geometries on Column Performance

Randomly packed beds of spherical particles, generally created by slurry packing, have long been the predominant internal morphology for chromatographic columns. However, slurry packing continues to suffer several drawbacks such as difficulty in attaining repeatable control of the packing process, complexities in modelling and scale up of the resultant beds, and radial heterogeneities, especially near the column walls.

The random micro-structure of the column packing also affects the chromatographic separation efficiency of a column due to every sample molecule taking a slightly different pathway through the structure, leading to residence time inhomogeneity and consequently band-broadening.

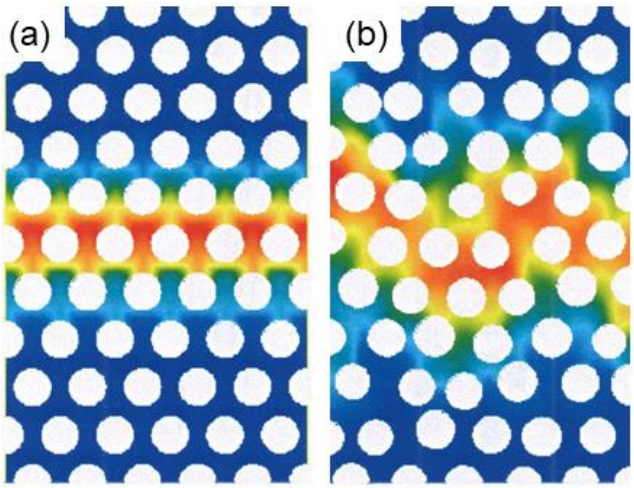

Figure 1.2: Computational fluid dynamic simulation of a sample migrating through an (a) ordered and (b) heterogeneous structure (reproduced from Billen et al.[13])

The detrimental effects of packing heterogeneity can be demonstrated using computational fluid dynamics (shown in Fig. 1.2), where even a small disruption in packing uniformity can lead to significant band-broadening. Regular placement of particles in a column is therefore crucial to reduce plate heights and increase separation efficiencies.

In addition to particle placement, attempts at optimizing particle shapes have been limited by the resin production methods. Like the slurry packing process, precise control of the resin particle shapes (predominantly spherical) cannot be achieved with the majority of production processes. While particles of a similar, though not identical shape can be produced, most production methods produce particles of varying sizes, leading to a loss in column performance.

If a packing of randomly packed monodisperse spheres was achieved, the sizes, shapes and alignment of voids would still contain significant amounts of variability. Even in an ordered arrangement of spheres, it is not possible to recreate the flow patterns assumed by several of the fundamental equations describing flow through porous media. While the particle shape is based on a regular platonic solid, the resultant void spaces that serve as the flow channels do not form an optimal geometry, either for creating a homogenous flow profile or for maximizing internal surface area, even in the case of an ordered packing arrangement, as seen in Fig. 1.3.

In the case of internally porous beads, while the diffusion profile of a single spherical bead is axisymmetric (i.e. identical diffusion path lengths in all directions), the diffusion profile of a set of spheres packed in a dense arrangement is not. To reduce residence time inhomogeneity, it is important not to characterize a porous structure only by defining the component particles of the solid phase but to also define and optimize its resulting flow channels.

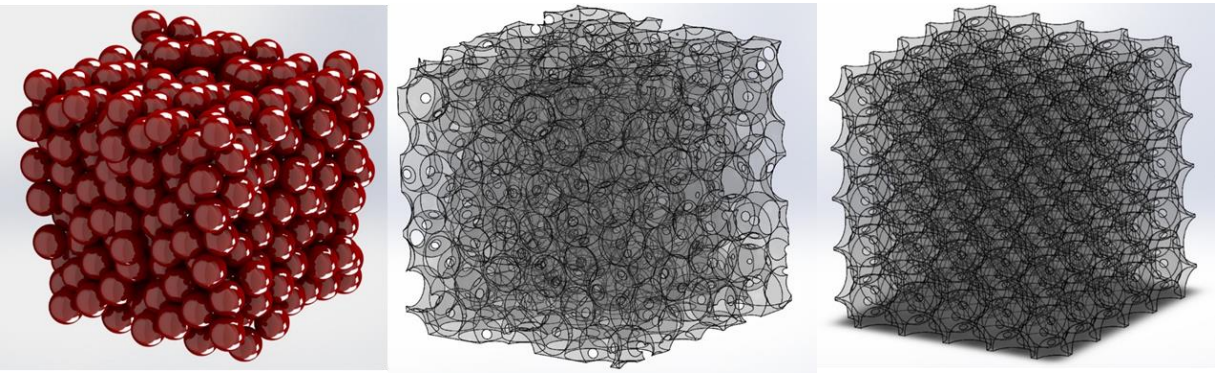

Figure 1.3: A sample void space in random loose packed spheres (left), a unit void space for spheres in a face-centered cubic configuration (center) and a unit cell of a void space for an octahedron in a simple cubic arrangement (right)

Heterogenous pore geometries have meant that fundamental equations mean that heuristic, black-box models are used to approximate properties of a porous structure. Darcy [14], Kozeny[15] and Carman[16] and Ergun[17] have described the pressure drop and permeability of porous structures while the works of Van-Deemter[10], Giddings[9] and Knox[11] have described the performance characteristics of chromatographic columns based on empirical characterization.

The accuracy and predictive powers of the above equations however have not translated into an understanding of the relationship between the physical properties of the porous media and its flow properties. To quote Gritti and Guiochon on the Van-Deemter equation[18]: *"Despite this good fit, it is generally recognized that the best parameters provided by this mathematical exercise are purely empirical and void of physical sense."*. Despite the importance of understanding and quantifying the microstructure of porous structures in chromatography columns, the effects on flow properties have not been well understood. With porous structures consisted of ordered repeating elements, the beginnings of a deterministic model for porous media could be constructed.

The first known mention of a deterministic model of column geometrical on dispersion is by Marcel Golay in 1956, in which he derived that narrow open tubular columns, owing to their axisymmetry, would be optimal for separations[19]. The column and sample volumes for any individual tube would be insufficient, but a bundle of parallel tubes could be the ideal geometry. However, even miniscule differences between the radii of each channel can cause significant

band-broadening or multiplet peaks (due to a Hagen-Poiseuille relation to the channel radius). This issue, known as polydispersity was first studied by Schilsa et al. multiple photonic crystal fibers[20]. Such geometries have since fallen out of favor by the chromatographic community and a need for radial interconnections was deemed to be a practical necessity.

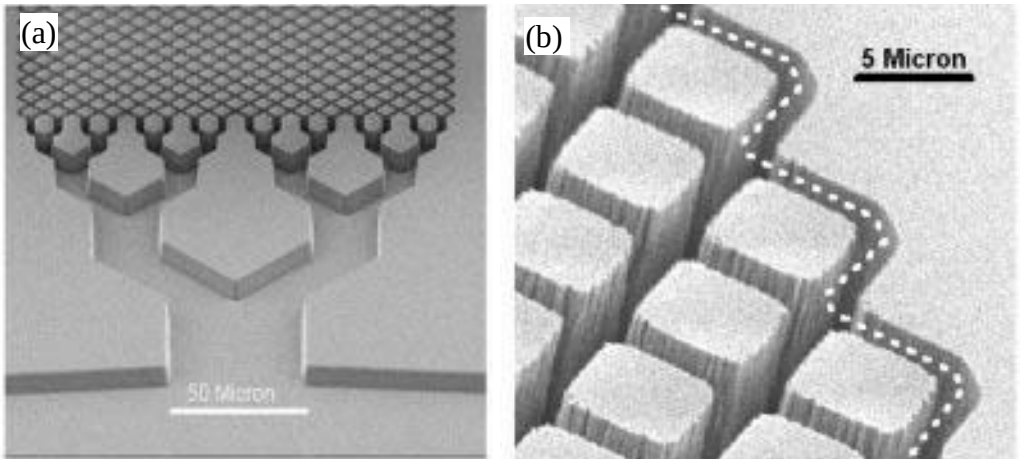

Figure 1.4: Ordered pillar arrays produced using deep reactive ion etching by Regnier and He[21]: (a) inlet flow distributor and (b) etched sidewalls

The first known mention of completely ordered, interwoven stationary phases or stationary phase skeletons appear in publications by He and Regnier [21–23], in which deep reactive ion etching was used on a quartz surface to produce a planar column with diamond shaped stationary phase supports, as shown in Fig. 1.4. Here, silicon ablation methods common in the production of micro-electrochemical systems (MEMS) was used to create channels with a width and depth of 1.5 and 10 µm respectively. In John Knox's final publication[24], he concluded that the largest contribution to dispersion was "*irregularity of the flow pattern in the packed bed*" in the bulk mobile phase and predicted that such an ordered column format was a promising approach.

The arguments for 3D-printing of stationary phases are almost identical to the ones presented for etched quartz chips, but with the additional benefits of larger column volumes that the technology enables. The subsequent sections summarize computational and experimental work conducted in the field of ordered media.

1.2.3 Computational Studies on Column Designs and Ordered Stationary Phases

Following the work of Regnier et al., several studies involving computational fluid dynamics (CFD) have been performed on dispersion effects in ordered structures. The computational methods used to study dispersion can be divided into two separate approaches: Commercial software packages such as Ansys Fluent or Comsol, computing flow fields based on the

Navier-stokes equation, and Lattice-botlzmann method (LBM) for solving advection-diffusion equations.

The first use of CFD to study packing geometries is from Schure et al.[25], who used LBM and supercomputers to simulate flow fields in random close packing (RCP) geometries. Van Deemter curves for reduced velocities of up to $Pe = 400$ were computed. In a subsequent publication [26], Schure et al. compared the reduced plate heights and flow resistances of ordered sphere packing and the RCP arrangements. A study of the three most common crystal structures, simple cubic (SC), body-centered (BCC) and face-centered cubic (FCC) showed BCC and FCC arrangements to produce significantly lower plate heights than the RCP arrangement.

As a more direct continuation of Regnier's work, Desmet et al. have studied the concept of chips comprising two-dimensional pillar arrays in detail using a commercial CFD package (Ansys Fluent). Gzil et al. demonstrated the advantages of an ordered pillar array over an 'ideal' random packed bed column (i.e. the lowest value empirically determined in literature) [27]. Across a range of retention factors and pillar porosities, minimum plate heights were found to be as low as $h = 0.1$. Additionally, flow resistances as low as $\varphi = 480$ were found, compared to $\varphi = 710$ for 'ideal' packed beds. Both here and with Schure's computational studies, the benefits of ordered porous structures are clearly outlined.

Further studies on pillar arrays showed that diamond-shaped pillars produced the lowest h_{min} values compared to cylindrical or hexagonal pillars[28], with radially elongated diamonds produced the least dispersion[29]. Increasing the chip porosity from $\varepsilon = 0.4$ to $\varepsilon = 0.8$ was shown to double minimum plate heights but reduce separation impedences by up to 76 % [30]. All the aforementioned simulations were performed using radial periodic boundary conditions, i.e. without walls or spatial confinement of geometries. LBM simulations by Daneyko et al.[31] have shown that cylindrical pillars are superior to sphere packings even with spatial confinement, albeit not at $Pe > 100$.

For three dimensional packings, Li et al. have recently tested alternative particle shapes in the three ordered packing arrangements using a commercial CFD package (Comsol Multiphysics) and found that axially elongated ellipsoidal particles provided the sharpest bands[32]. However, freedom to design three-dimensional geometries means that porous beds need not be limited to particle packings but can include ordered monolithic structures.

Deridder et al. have explored the B-term properties across a range of retention factors for tetrahedral skeletal monoliths (TSM) in an effort to study silica monoliths[33].

The most direct three-dimensional analogy to Golay's open tubular solution was studied by Gzil et al. [34]. Here, a set of parallel plates (parallel to the flow direction) with differing degrees of radial interconnectivity, given a certain degree of manufacturing errors were compared. The radial interconnects were designed to mitigate the polydispersity effects outlined by Schisla et al.[20]. It was concluded that parallel plate columns (PPC) could provide an improvement of one order of magnitude to state-of-the-art HPLC columns. In a subsequent review by the same group, Billen et al.[35] declared that such a geometry is the ideal stationary phase geometry, if only "*an army of high-precision nano-robots*" were available to build it. Whether the performance of PPC geometries could be surpassed is an open question, but 3D-printing may be the nanorobot army to test such geometries. Overall, CFD studies listed here on both two and three-dimensional geometries indicate the possibilities of superior alternatives to random sphere packings that currently dominate liquid chromatography.

In addition to the heterogeneities caused by random packings, current chromatography columns face the issue of wall effects. As the particles immediately neighbouring the column walls are sub-optimally arranged, higher local extra-particle porosity along the column walls is an inevitable by-product of physically confining a set of particles within a regular shaped (typically cylindrical) container. Several studies have demonstrated the loss in column performances caused by wall effects, particularly in columns with low column-to-particle diameter ratios where the effects are more pronounced. Direct concentration measurements using microvoltammetric electrodes on HPLC columns[36] as well as recent simulations on three-dimensional reconstructions of columns by Reising et al.[37], show wall effects to be a large contributor to axial dispersion. Yew et al. estimates that for certain aspect ratios, half of a columns efficiency is lost due to this effect[38]. In the simulations by Daneyko et al. comparing ordered pillars and random packed spheres [39], a doubling of plate heights compared to bulk packings were seen for an aspect ratio of 20.

Flow distribution across the head of a column is an additional structural aspect that is known to affect its final performance[40]. To reduce band-broadening, the column's mobile phase and samples are invariably fed through a narrow ID (internal diameter) capillary. The challenge is to distribute the sample evenly across the radial profile of a column, with wider preparative columns being particularly prone to maldistribution [41]. Computational studies can reveal

differences and potential improvements in distributor designs. The needs of flow distributors for use in liquid chromatography are especially demanding, as dead volumes and extra-column band broadening from the distributors themselves need to be minimized. Narrower ID columns and higher back-pressures, mean that flow distribution is a less critical issue in HPLC columns than in preparative scale systems.

Fractal distributors with successive self-similar splitting branches (shown Fig. 1.4a) are common in microfluidic devices to spread a fluid from the inlet channel across a device[42,43]. Several computational studies comparing distributor designs for a planar chromatography column or device format have been conducted[44,45]. It was found that a radially interconnecting diamond pattern was less impacted by clogging than the fractal layout, although at the cost of higher band-broadening. Jespers et al. found that a 'hybrid' fractal distributor with periodic radial interconnects provides a good compromise between the damaging effects of clogging and increasing band-broadening[46].

For three-dimensional devices (i.e. with an inlet plane rather than an inlet line), the equivalent design is a Mandelbrot H-tree[47], a planar fractal branching layout. Such distributors have been optimized for reducing flow inhomogeneities and back-pressures [48–52], also been used for chronographic devices [53]. Because of the branching structure of the H-tree, the inlet is invariably on a column with a square cross section, rather than a circular plane that is most common in chromatography and process engineering in general.

A company called AriFractal has created a hybrid design with spiral segments and a modified H-tree for a circular cross section [54]. These designs were specifically intended for large scale simulated moving bed and ion exchange chromatography, i.e. the most challenging cases for flow distribution. Its' performance evaluation reports show good flow distribution across all outlet nodes [55], but no data on dispersion or band broadening is given. Recently, Park et al. have used CFD simulations with Comsol Multiphysics to design and optimize a different distributor design for circular cross-sections involving a series of baffles[56]. As with the previous distributor, the outlet nodes showed homogenous velocity profiles but no data on dispersion was given.

The dead-volumes in both the circular cross-section designs seem prohibitively high to be meaningful in most liquid chromatography columns. A design for a low dispersion flow distributor for circular cross-sections remains elusive, with a technology such as 3D-printing being well suited to produce any three-dimensional layouts recommended by simulations.

1.2.4 Experiments with Ordered Stationary Phases

As with the computational tests, Regnier's seminal work on ordered stationary phase supports were followed by Desmet's and Gardenier's groups. De Malsche et al. have developed, optimized and studied the limits of the production process [57–59], several geometrical characteristics[60,61], producing mesoporous rings to produce core-shell pillars[62,63] and retentive capabilities to perform a wide range of liquid chromatographic separations [64–68].

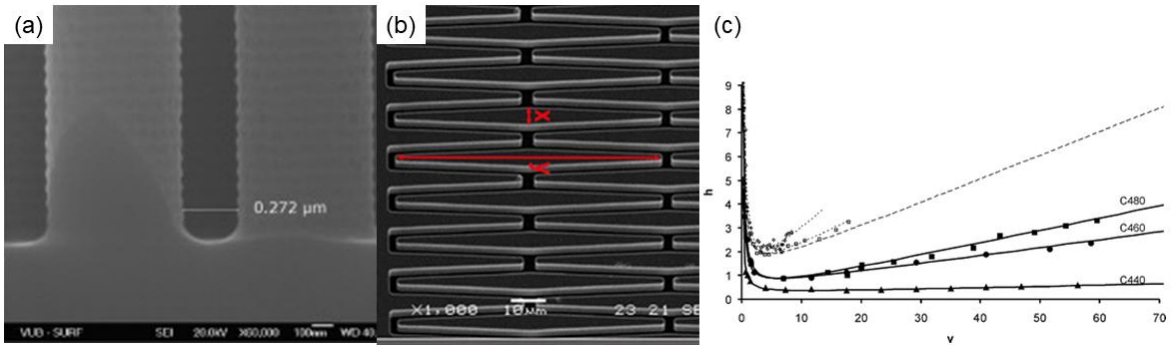

Figure 1.5: (a) 0.6 µm pillars with 0.3 µm designed spacings[57] , (b) radially elongated pillars [60] and (c) Van Deemter curves of separations of a mixture of three coumarin dyes using pillar array columns [62]

The deep UV etching process was found to allow for pillars as narrow as 0.6 µm (shown in Fig. 1.5a), with interpillar distances of 0.3 µm[57]; dimensions that are well suited for HPLC. An entire 'column' length of up to 2 m can be etched into a device with a small footprint because of periodic turns between rows of pillar arrays.

In the study involving pillar arrays, radially elongated pillars were found to yield lower plate heights, as with the relevant computational study [60,63]. Fig. 1.5c shows a Van Deemter profile for a separation using pillar arrays of coumarin dyes compared to empirical data from packed columns and the 'ideal' packed column (dashed grey line). Reduced plate heights of under 1 and absolute plate heights of under 5 µm demonstrate the efficacy of ordered stationary phases.

The etching process also meant that potential solutions to the issue of wall effects. In a computational study on two-dimensional pillar arrays, Vervoort et al. tested the effects of partially protruding pillars on the edges of the chip's walls [69]. However, they found that this led to an increase in band-broadening. Instead, a straight wall with a gap of 0.15 cylinder diameters was shown to be most effective. However, follow up experiments on etched pillar arrays appear not to conform to the simulation's predictions and show that partially embedded cylinders produce lower reduced plate heights[61]. However, with radially elongated pillars, the wall effects were found to be almost completely eliminated[70].

The primary limitation of this method however, is the depth of the chips that can be etched and the resultant low column volumes that can be produced. The etching depth that can be achieved using this process is limited to 30 × d_p (where d_p is the pillar diameter). Creating deeper channels causes significant tapering, where the bottom of the through-pores are 10 – 20% narrower than the top[57]. The uniformity of the geometry is therefore compromised with deeper channels, meaning that creating preparative scale columns is not feasible with such an approach. Nevertheless, the overwhelming advantages of pillar array columns have led to the creation of a spinoff company (PharmaFluidics[71], Ghent, Belgium) for HPLC applications, particularly those involving low sample volumes.

Efforts to create fully three-dimensional columns with an ordered morphology have centered on colloidal silica particle arranged in a face-centered cubic configuration in narrow (i.e. < 150 µm) capillaries by Wirth et al.[72] using a method that is undisclosed thus far. At these dimensions, the phenomenon of slip-flow (i.e. when velocity at the walls of a solid are greater than zero) was utilized to further reduce band-broadening [73–76]. Sub-micron colloidal particles used for separations of bovine serum albumin with plate heights of 0.015 µm (h = 0.03)[72]. However, seemingly ultra-efficient separations come with a large number of issues that are mainly limitations caused by using very small particles. Issues such as band-broadening caused by column fittings, very high back-pressures and limited detection modes mean that such columns are limited in their scope.

In a similar vein, Liao et al. have devised a rapid method for the packing of highly ordered silica particles based on photonic crystals without a significant number of cracks[77]. The particle sizes used here were also < 1 µm in size, with plate heights in the order of 300 nm being reported. As the authors admit, these particle sizes mean that pressure-driven flow is impractical. Instead, they have used electroosmotic flow to move the sample across the chip, as Regnier did in 1998[22]. While this approach is promising for niche applications, it is unlikely that the $6 bn dollar LC sector would shift from pressure to electro-driven flows (and tackle the numerous practical issues) to capture the benefits of ordered stationary phases.

In summary, the current set of manufacturing methods do not seem to be adequate for utilizing the benefits of ordered stationary phase across the necessary range of LC column dimensions. In particular, a glaring gap exists in the ability to manufacture ordered packed beds for preparative columns. As explained in the subsequent sections, 3D-printing seems

uniquely well suited to address this gap and create possibilities for highly efficient separations.

1.2.5 The Case for 3D-Printed Stationary Phases

In this thesis, the use of 3D-printing or additive manufacturing to create packed beds with precise control over the size, shape, orientation and arrangement of particles at a large scale is investigated. Computer aided drawing (CAD) models of custom-designed packed beds, optimized for their flow properties can be precisely replicated in range of materials. While materials that are internally porous can be printed, this thesis studies the fluid mechanical properties of superficially porous (i.e. internally non-porous) structures.

3D-printing not only allows for the large-scale manufacturing of packing in an ordered arrangement, it is also possible to create packed beds with non-spherical particles, and non-cylindrical column formats. A key feature of the columns printed in this study is that the porous bed, column walls, flow distributor and external fittings are all mechanically connected to form a single monolithic entity as shown in Fig. 1.6a, meaning that no further assembly of any column part is required. These printed parts are not monoliths in the traditional sense, which simply translate the problems of random packing into a problem of random placement of pores[78].

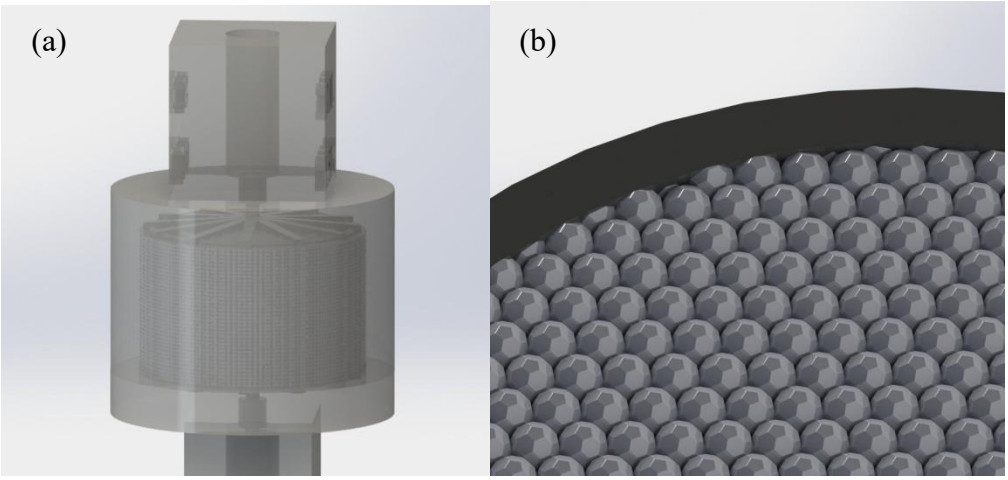

Figure 1.6: (a) CAD model of full column with packing, flow distributors, column walls and fittings and (b) Model of layer with partially protruding beads along the column walls

In addition to optimizing the micro-structure of the porous bed, it is possible to circumvent the problem of wall effects by producing columns with partially protruding beads (Fig. 1.6b), meaning that the local porosity along the column walls is identical to the porosity seen in the rest of the packing. Furthermore, flow distributor designs and templates can be optimized based

on the geometrical requirements of the porous bed, reducing the heterogeneity in a molecule's residence time through the column based its radial positioning.

More fundamentally, 3D-printing allows us to rethink and supersede notions of packed beds or monoliths entirely and design custom made flow channels in three dimensions. For example, Desmet et al. have shown in a theoretical analysis that a porous structure comprised of regular 2D array of pillars produces a significantly smaller A-term contribution than a regular packed bed. 3D printing can serve as a tabula rasa for such novel column geometries outside the paradigm of packed beds or traditional monoliths which can be designed, produced and reliably tested in a short time-frame. The aim of this project is to create and test proof-of-concept studies of 3D-printed porous media and the use of fine control over the porous geometric structure to investigate the related flow behaviours.

1.3 Additive Manufacturing Methods

1.3.1 Physical Requirements

Table 1.1 shows two examples of liquid chromatography columns on two different scales that are typically found in practice. At the preparative scale, a Sepharose Big Beads (General Electric Life Sciences, Uppsala, Sweden) Ion Chromatography column [79] is used as the example for large particles and column volumes. The particles used in this example are on the larger end of particle sizes typically used for preparative chromatography. For analytical separations, we take the example of an Ascentis Express column by Sigma-Aldrich [80], used for example in lipidomics separations[81].

Several manufacturing methods are described below and compared with respect to their abilities to produce geometries with similar dimensions. The printing resolution of the methods are compared with respect to their ability to produce features corresponding to the mean particle diameter. The build volumes of the printing methods must also be able to accommodate columns with the mentioned column diameters and lengths.

Table 1.1: Dimensions and features of a typical preparative scale and analytical scale column. Data sourced from product catalogues of the respective suppliers [82,83]

	Preparative **Sepharose Big Beads XK 26/20 Column**	*Analytical* **Ascentis® Express C18**
Mean Particle Diameter (μm)	200 (100-300)	2.0
Column Length and Diameter (mm)	150, 13.0	50 , 2.1
Recommended Linear Flow Rate ($cm.hr^{-1}$)	500-1000	200-700
Resin Materials	Cross linked agarose and dextran	C18 Silica
Maximum Operating Pressure Drop (MPa)	0.3	10.0

The radial aspect ratios (D_C/d_p) are 65 and 920 for preparative and analytical scales respectively. The corresponding axial aspect ratios (D_L/d_p) are 750 and 25 000. Assuming that each particle is described by 10 × 10 × 10 voxels, the 3D printing technologies compared here must be able to produce structures in the order of 100 × 100 × 1000 and 10 000 × 10 000

× 200 000 voxels in size for conventional preparative and analytical applications respectively. Additionally, the resolution of the printing methods must be capable of producing the necessary particle sizes.

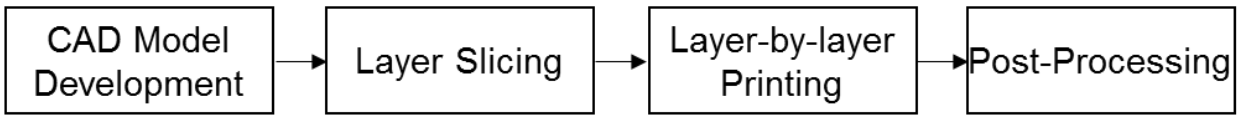

Figure 1.7: Workflow of 3D-printing an object

The typical workflow involving 3D-printing has is shown in Fig. 1.7. The full geometry of the column and ancillary parts must first be drawn in 3D using a Computer Aided Design (CAD) software and exported as a surface tessellation model (.stl) file. The .stl format defines a three-dimensional surface (of the solid object) as a series of adjacent triangles. This file is then imported to a slicing software, such as the freely available Cura or NanoDLP or slicing software specific to a 3D-printer model. This converts the 3D model of the column into discrete slices based on a defined layer thickness. The geometries of each slice are then fed to the 3D-printer, which successively solidifies or prints each layer of the geometry. After printing the parts printed devices or columns require some form of post-processing to be used for its' final application.

It is worth mentioning that 3D-printing or additive manufacturing is not a single technology, but rather a loose collection of manufacturing methods in which successive layers of a material are added to form a three-dimensional object. Numerous methods of 3D-printing have been developed in the past two decades. This section will only describe the printing processes that could plausibly print structures with the desired resolutions and aspect ratios for the two columns mentioned above. Common 3D-printing methods such as Fused Deposition Modelling (FDM) and other methods such as Laminated Object Manufacturing (LOM) are therefore not included this overview.

1.3.2 Selective Laser Melting (SLM)

A common method of producing metal parts using additive manufacturing is a selective laser melting or direct metal laser sintering process. A powdered form of the desired metal is stored on the powder bed. A three-dimensional model is divided into separate layers consisting of binary images. A high-powered laser is used to melt the relevant portions of the layer, as seen in Fig. 1.8). The fabrication platform is then moved downwards by a designated length (typically, a user-defined layer thickness) and a new layer of powder is deposited on

the previously molten layer using a roller. The next binary image is then used to melt the freshly deposited layer of metal powder. A 3D structure is created as a result of successively melting layers of metal alloys powders.

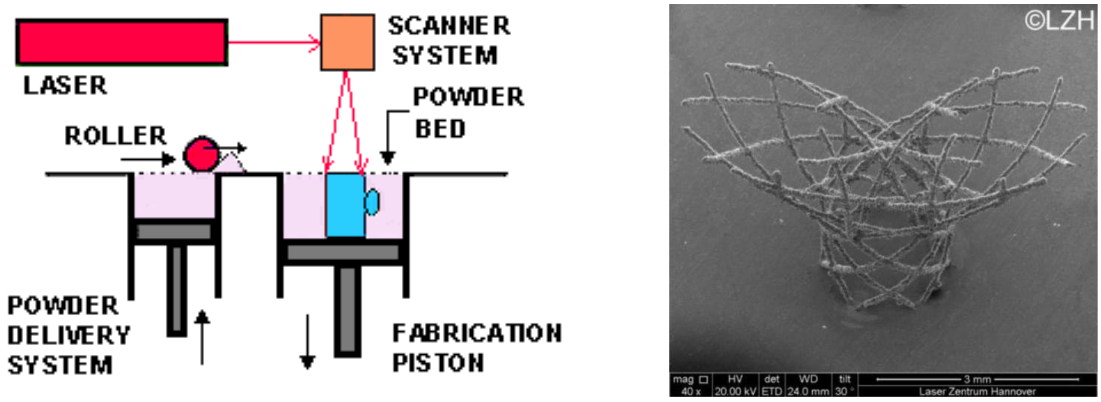

Figure 1.8: Left: Schematic of Selective Laser Melting (SLM) process, Right: vascular implant with < 100 µm beam diameters in a titanium based alloy with a micro-SLM system[84]

The resolution limitations in this process typically relate to the size of the alloy powders, which are typically in the range of 100-200 µm. The precision and extent of heat diffusion from the laser and homogeneity of the deposited powder also serve as limitations to part resolution. The minimum feature sizes that are achievable are therefore larger than 500 µm from regular SLM systems. However, very high aspect ratios can be achieved by simply scanning the laser over large areas, at the expense of manufacturing times. Commercial systems with build envelopes as large as 6 × 1.4 × 1.4 m are available [85].

A critical part of SLM is that overhanging features in the geometry are supported by the unmolten portions of the previous layers in the powder bed. As porous structures inevitably contain overhanging parts, removal of the debris should be taken into consideration. For producing column housings for analytical separations, Gupta et al. found that a minimum channel diameter of 0.9 mm was necessary to remove the residual powder within the channels [86–88] using a commercial SLM system. With such limitations, the residual powder in a porous grid with channels < 0.3 mm therefore cannot be removed.

The basic processes of an SLM system can however, be miniaturized to improve print resolution. Gieseke et al. of Laser Zentrum Hannover have developed a ‘micro-sintering’ method in which powders with grain sizes of < 20 µm and are used to 3D-print small scaffolds [84]. The spot size of the laser was also 20 µm, compared to 100-200 µm used for commercial SLM systems. Figure 1.8 shows a scaffold printed using this method, with beam diameters as small as 60 µm. The finer grains would also allow for easier removal of residual

powder after printing a porous structure. When printing with the dimensions of the preparative column described in Table 1.1, printing times could prove to be a limiting factor. Nevertheless, such a system could conceivably be used for a method such as immobilized metal affinity chromatography.

1.3.3 Inkjet Printing (i3DP)

Inkjet or multijet printing is a common printing method used for prototyping a wide range of products. Figure 1.9a shows the components required for an i3DP setup. A minimum of two print-heads is necessary, with one depositing the build material (a UV-curable monomer powder) and the other print-head depositing a supporting material on the voids created under overhanging features of a geometry. Each slice is discretized into linear segments which defines the path of the print-head. A leveling blade is then used to flatten the deposited material into a desired layer thickness and a UV-lamp is shone across the printed layer. Multi-material printing can be achieved by increasing the number of print-heads and commercial systems can produce up to 256 blends based on three base materials [89].

The resolution in the x direction is determined by the precision of the print-head and the y resolution is limited by the width of linear segments. The x-y resolutions of i3DP machines are typically in the order of 300-750 dots per inch, or 30 - 85 µm, depending on the printer settings[90]. The layer thickness, typically between 15-40 µm is the primary limitation in the z-axis. With the previously assumed 10 × 10 × 10 voxels per particle, the x, y and z resolutions of this method approach the upper limits of the preparative scale column dimensions listed in Table 1.1. Build areas of 500 × 400 mm also mean that the desired aspect ratios can be achieved.

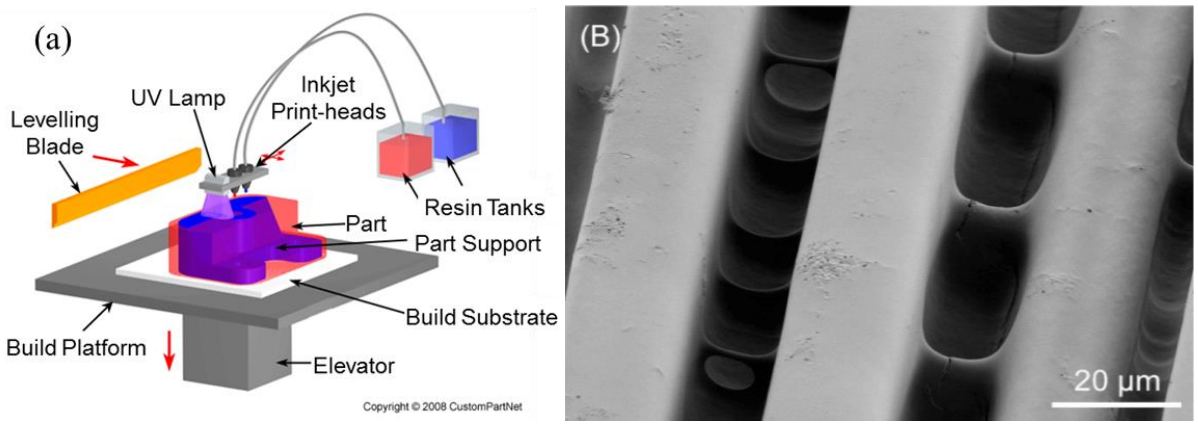

Figure 1.9: Basic schematic of the inkjet printing procedure [91] (b) scanning electron microscopic (SEM) of linear striations produced using an Objet Connex polyjet system used for chromatographic separations of dyes [92]

This technology does theoretically allow for the use of a wide range of build materials. However, in a commercial inkjet system, the material choice is usually limited to a few resins made by the 3D printer manufacturer.

Porous structures built using this method will almost always contain overhanging features and therefore involve the use of support material, which is typically a proprietary wax produced by the 3D printer manufacturer. A post-processing step is therefore necessary to remove the support material.

Because the parts are printed as a sequence of linear segments, the microstructure of the porous beds will consist of linear striations instead of smooth surfaces. MacDonald et al. have used this property of i3DP systems to deliberately create parallel 20 µm wide channels and periodically connecting bridges, as seen in Fig. 1.9.b[92]. The capillary forces caused by parallel striations and the bridges and the hydrophobic surface of the build material enabled a thin layer chromatography type separation of dyes.

1.3.4 Stereolithography (SLA)

Stereolithography (SLA) describes a broad-ranging spectrum of processes involving the use of layer by layer manufacturing of UV or light cured resins. The common features of an SLA printer are a Z-stage where the part is printed and a liquid resin tank, where a photopolymer is stored. UV light is typically used to cure successive layers of the liquid resin. Four formats of SLA printers currently exist on the market: formats where the photopolymer is illuminated from above or below the tray (top-down or bottom-up systems) and where the layers are projected as an image or rastered using a laser. This sub-section will focus on the method that has shown to yield the maximum resolution: digital light processing [93,94].

Digital Light Processing (DLP)

In this bottom-up system a resin tank with a transparent bottom surface, as shown in Fig. 1.10. A projector lamp or laser in combination with a digital mirror device (DMD) is then used to selectively cure and solidify the desired pixels in the bottom layer of the resin tank. The fabrication platform is then shifted upwards (and therefore peeling the part from the bottom of the tank) to cure the next layer of resin. The process is performed on a set of discrete layers to create a 3D structure with the fabrication platform moving upwards after each layer is cured. Because a two-dimensional image is cured simultaneously rather than

single discrete segments or voxels means that the manufacturing times are significantly lower than other methods.

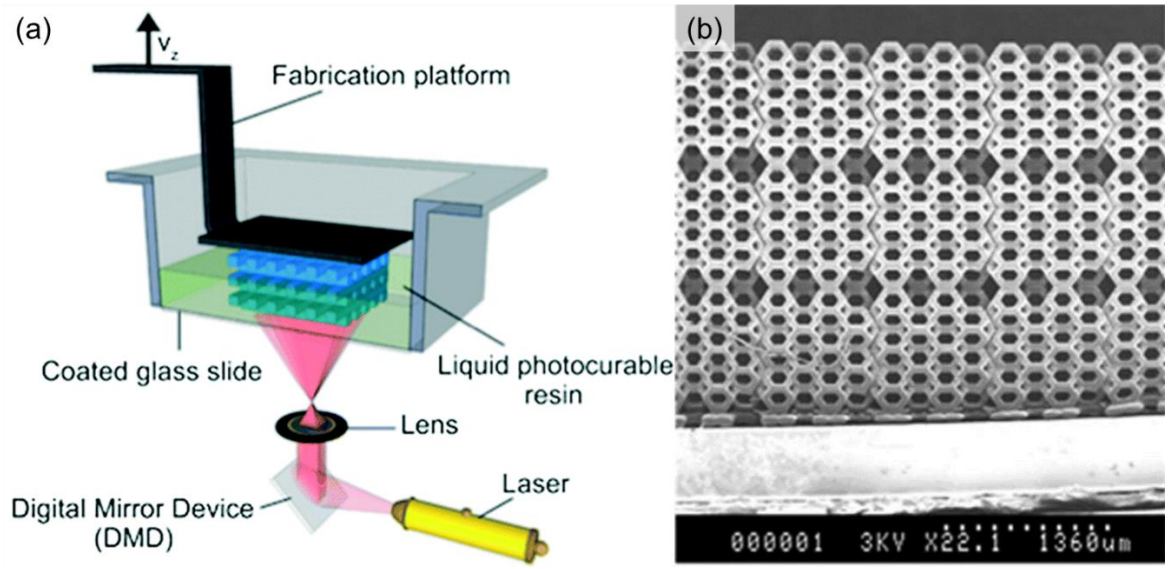

Figure 1.10: (a) Fabrication procedure of digital light processing using a digital mirror device and bottom-up orientation [95] and (b) SEM image of a porous grid produced using a micro-stereolithography system[96]

The pixel sizes of the projected image are in the range of 20-100 µm and represent the theoretical limit in x-y resolution. The minimum layer heights in commercial DLP systems are typically 20 - 50 µm and are the resolution limitation in the z direction. However, the practical resolution limits for a porous grid or a channel for a typical DLP printer is 300-400 µm with the build range of ~ 150 × 150 × 200 mm.

These specifications translate to radial and axial aspect ratios of roughly 1100 and 1000 respectively. The limitation on the aspect ratio in the z-direction is the range that the fabrication platform travels. The number of layers that can be manufactured using this procedure can therefore be increased substantially with a relatively minor modification of the system. The horizontal aspect ratios are limited by the number of pixels that can be processed by the digital mirror device and therefore require larger modifications to achieve higher horizontal aspect ratios. A discrete layer-by-layer manufacturing process would mean that at the micro-structural level, the striations on the printed parts are planar rather than linear. MacDonald et al. have shown that, DLP based microfluidic chips produced laminar flows with the least amount of peturbations[97]. Due to the nature of this process, only UV cross-linked materials can be used to print objects in this method. However, the photopolymer can be investment casted [98,99] or pre-loaded with ceramics [100–102], which can then be de-binded

and sintered. Kotz et al. have used this method to 3D-print fused silica parts using a DLP system and a silica nanoparticle suspension[103].

Unlike previously discussed methods, the build time is solely a function of the part's height and the number of layers that will be printed and independent of the part's volume. The curing times are typically 5-30 seconds per layer with a 25 μm layer height. Recently, a process called continuous liquid interface production (CLIP) has been developed to reduce print times [104–106]. In this process, the fabrication platform moves continuously upwards rather than in discrete steps to cure each layer separately. The peeling step that is necessary in DLP is eliminated by maintaining a thin 'dead zone' where oxygen permeates through the bottom of the tank and inhibits photo-polymerization. This process is shown to increase the print speeds by up to 100-fold to turn 3D-printing from a prototyping tool to a mass-production method. This means that the printing times for the preparative column in Table 1.1 could in principle be produced in 5 - 30 minutes, depending on the resin properties, without compromising on resolution.

Projection Micro-Stereolithography (PμSL)

The resolution limitations in DLP are the pixel size and layer thickness. These two limitations can both be superseded [93,107]: the x-y resolution can improved by de-magnifying the projected image to reduce pixel sizes to < 5 μm and the z-resolution can be improved with the use of more accurate and robust z-stage and actuator for reduced layer heights. Features sizes as low as 1 μm have been reported [96,108,109] using this method. As the number of pixels in the image remains identical (typically in the order of 1000 × 1000 pixels), the parts printed with this method are proportionately smaller. The reduced layer heights also mean that the print times proportionally longer for a given part height.

Fang et al. have devised a system to increase the x-y aspect ratio eight-fold by curing 1000 × 1000 pixel regions in succession, with a x-y stage moving to cure the eight separate regions[96]. Fig. 1.10b shows a porous grid where four adjacent unit-cells of cubes can be seen in the x-direction. This method has also been used for the printing of hydrogels and ceramics[109,110]. The resolutions and aspect ratios reported in literature indicate that this method can be used to print narrow-bore HPLC columns but not preparative scale columns. However, the major limitation of PμSL is the lack of commercially available systems that are commonplace for the other printing techniques mentioned in this sub-chapter.

1.3.5 Two-Photon Polymerization (2PP)

The highest resolution printing technology that currently exists is a photo-lithographic process known as two-photon polymerization [111]. In this process, two femtosecond laser pulses are focused onto a liquid photoresist to cure a single voxel. Galvo-scanners scan the focus point across a layer and successively cure multiple layers to create the final three-dimensional object. The resolutions of two-photon systems are not diffraction limited, and features sizes of 100 nm have been reported [112–115].

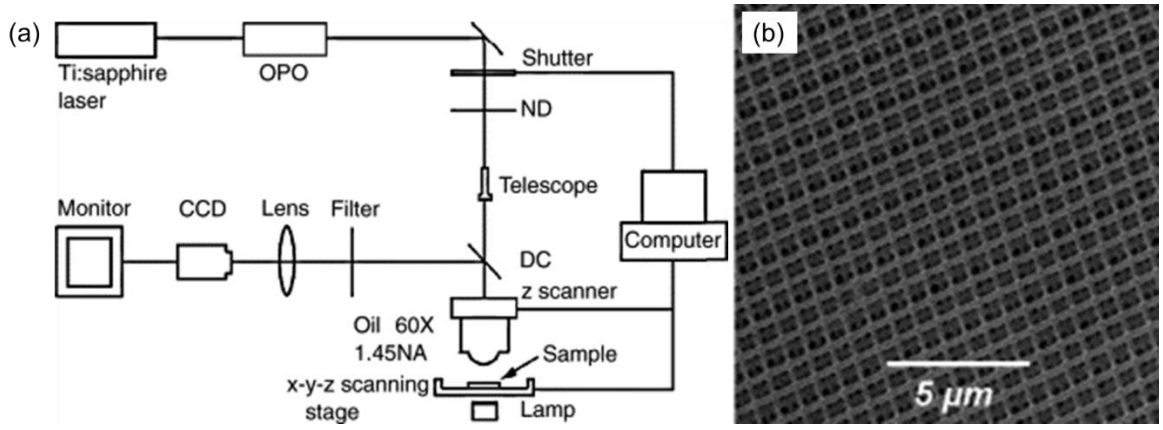

Figure 1.11: (a) Schematic of two-photon polymerization (2PP) and (b) SEM image of a porous lattice using 2PP [116]

As shown in Fig. 1.11a, microscope and CCD setups to monitor the printing process are also common. Like the SLA based printing techniques, uncured liquid photopolymer needs to be removed from the porous grid: this is typically performed by dissolving the resin using solvents such as ethanol or isopropanol. Fig. 1.11b shows a lattice printed with 200 nm rods and 600 nm spacings printed by Wu et al. in 2006 [116]. In a manner analogous to PµSL, the voxel size can be varied by controlling the projection optics to create larger, lower resolution pieces in a process known as wider objective working range or WOW-2PP [117].

The resolutions produced by 2PP are ideal for analytical scale columns, with regular stationary phase dimensions that can be printed with good spatial definitions. Mathause et al. from the Vrije Universiteit Brussel are currently developing analytical scale stationary phase geometries using 2PP [118]. A channel with a width and depth of 200 and 15 µm was pre-etched on a glass slide. The stationary phase is then printed onto the glass slide directly, with the intention of bonding another glass slide on top of the stationary phase once the porous grid is printed and post-processed. Key considerations for this process are optimizing slicing and hatching thicknesses for any given geometry and creating a robust attachment between the glass slide and stationary phase.

The limitations with 2PP are not necessarily build volumes themselves, but the build times that larger structures would require. Each voxel of the piece has to be printed in succession, rather than in parallel as with DLP printing. In the case of Matheuse et al., the print times for a 500 × 200 × 15 µm (length × width × depth) stationary phase are in the order of five hours. While not an impractical production time, the scope for printing longer or wider HPLC columns is limited. Nevertheless, two-photon polymerization remains the most attractive 3D-pirnting method for analytical scale stationary phases.

1.3.6 Additive Manufacturing Methods - An Overview

The current field of 3D-printing contains several technologies that could plausibly meet the physical requirements of chromatography columns listed in Table 1.1. Processes such as µ-SLM and CLIP-SLA seem suited to preparative scale columns whereas PµSL and 2PP's resolutions are more suited to analytical scale columns.

To date, no systematic comparison of printer resolutions exists for porous grids in literature. The most relevant comparison for the purposes of chromatography is on the suitability of three different 3D-printing methods for fluidic devices, performed by MacDonald et al. [97]. In this comparison, a Y-junction with 500 × 500 µm inlet channels and a 750 × 500 µm main channel were printed using three different methods: an FDM (Felix 3.0, FelixPrinters, IJsselstein, The Netherlands), i3DP (Eden 260VS, Stratasys, Eden Prairie, Minnesota, United States) and a DLP system (Miicraft+, Miicraft, Jena, Germany) were used to create an identical channel junction design. As well as microscope images of flow tests using dyes (shown in Fig. 1.12), SEM images and profilometer measurements were taken on test pieces from each printer.

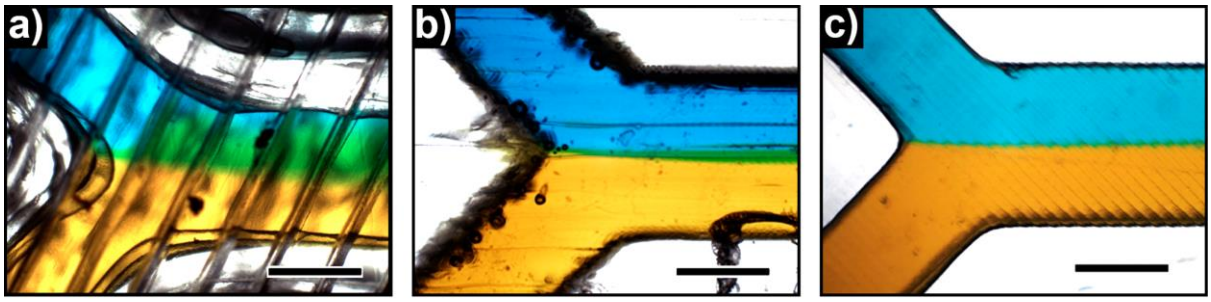

Figure 1.12: Microscope images of two food dyes into a 750 × 500 µm Y-junction channel printed using: (a) FDM, (b) i3DP and (c) DLP printer[97]

In the case of this comparison, mixing of the two streams (blue and orange in Fig. 1.12) indicates rugosities in the channel surface and therefore, inferior printer resolutions. Both the flow tests and SEM images showed that FDM was the most unsuitable method for well-

defined channels with rough surfaces due to extrusion lines produced by the FDM process. Both i3DP and DLP printers created smoother channels, with DLP producing the least amount of mixing between the two streams.

The choice of the printers for this project was also determined by the availability of robust 3D-printers in the vicinity. 2PP systems or custom setups for PμSL or μSLM were therefore not considered. The accessible choices were the following:

- A vat based DLP system (Perfactory Mini, EnvisionTec, Gladbeck, Germany) with an x-y pixel size of 17 μm and a minimum layer height of 15 μm.
- An i3DP system (Projet 3510 HD) with a nominal x-y resolution of 30 μm and minimum layer heights of 29 μm [90] available at the Ara Institute (formerly Christchurch Polytechnic Institute of Technology)
- A multi-material i3DP system (Objet Connex 350, Stratasys, Eden Prairie, Minnesota, United States) available at the mechanical engineering department of the University of Canterbury with a nominal resolution of 42 × 42 × 16 μm (x, y, z)[89].

Tests with the DLP systems showed the light source and slicer software to be unreliable. The two i3DP systems were significantly more robust in producing a large number of test pieces. However, neither systems contained the option to print without supporting wax. In the case of the Objet Connex 350, removal of support material from fine porous beds was a key limiting factor. Despite identical printing methods, the support wax of the Object Connex 350 was significantly more difficult to remove. The vendor's recommended method of using a water jet is effective for a part's external supports but does not remove the support wax from the internal voids of a lattice. Paull et al. report that 300 μm ID straight channels can be cleared at a rate of 1 cm/day with their custom wax setup[119]. In contrast, an effective support removal method was devised for the Projet 3510 HD and is described in the subsequent chapter. This printer was therefore chosen as the preferred printing method for the work reported in this thesis.

It is worth mentioning that neither the comparison of microfluidic devices, nor this overview of printing methods is exhaustive or definitive. Each printing method presents a set of trade-offs in terms of resolution, aspect ratios, material choice and support material removal, in addition to numerous method-specific parameters that can be tuned for maximizing

resolution. In a rapidly evolving field such as additive manufacturing, such comparisons serve as indicators of current abilities rather than the inherent limits of each technology.

Furthermore, the printing method and material chosen herein do not necessarily favour any retention mechanisms. The columns described in this thesis only describe dispersion effects of different bed geometries using unretained tracers. Achieving separations on such printed columns would require an additional step such as surface functionalization and is beyond the scope of this thesis and project.

2. Proof-of-Concept Columns

2.1 Introduction

Chapter one contains a summary of relevant printing technologies for creating columns used in preparative chromatography. To demonstrate the efficacy, versatility and feasibility of 3D printing for this application and to understand the working dimensions, printer resolution and specific procedures involved in the 3D printing of packed beds, prototype columns were built. The aim of the work described in this Chapter was to produce and test initial prototype 3D printed porous structures as a proof-of-concept. This aim can be broken down into several sub-goals:

- The development of a reliable method to 3D-print ordered arrangements and remove support material after printing using an inkjet printing (i3DP) system.
- To establish the dimensions of column features that can be produced at current printer resolutions, i.e. characteristic dimensions of particles, column size, etc.
- To determine the feasibility of adding additional features (such as column walls and integrated fluid distribution systems)
- To create a setup to perform fluid dispersion studies on 3D printed columns through tracer pulse injection tests.

2.2 Full Column Designs

In addition to the porous bed, ancillary features such as column walls, flow distributor and external fittings can be added to the 3D design to form a single monolithic entity as shown in Fig. 2.1, meaning that no further assembly of any column part is required.

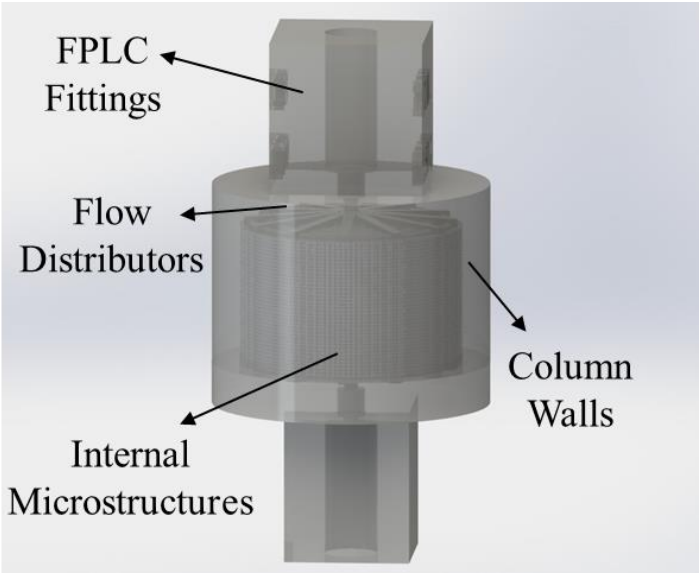

Figure 2.1. Schematic of a full column with ancillary elements

The main focus of this thesis was to study the effects of different column microstructures. The ability to print single piece columns assists with making direct comparison between different geometries. This is because every other part of the column other than its' internal microstructure can be identical in printed models for comparisons. This is in contrast to other experimental characterizations of columns where extra-column band broadening and wall effects can be affected by the studied microstructures themselves[120–122]. This difference is most prominent in comparisons between particle packings and monolithic structures.

To test a packed bed with beads in an ordered arrangement, a column with octahedral beads arranged in a simple cubic arrangement (SC) was produced. A non-spherical particle shape was chosen because of its lower computational load. Because a 3D geometry is described in an .stl file as a set of flat surfaces, the file size of a column containing non-spherical beads can be two to three orders of magnitude smaller than a column containing an identical number of spherical beads. Among the non-spherical particle shapes, the octahedron was chosen because of its natural compatibility with the simple cubic configuration and the simplicity in CAD design that this configuration presents. Additionally, test pieces with octahedral beads showed that an apothem (i.e. internal radius) in the range of 100–120 µm could be reliably printed. However, octahedral particles connected only by their vertices would not be sufficiently mechanically robust to withstand the stress of fluid flow. To produce a robust porous structure where the positioning of the particles remained fixed, the particles were designed to be slightly overlapping as seen in Fig. 2.2a.

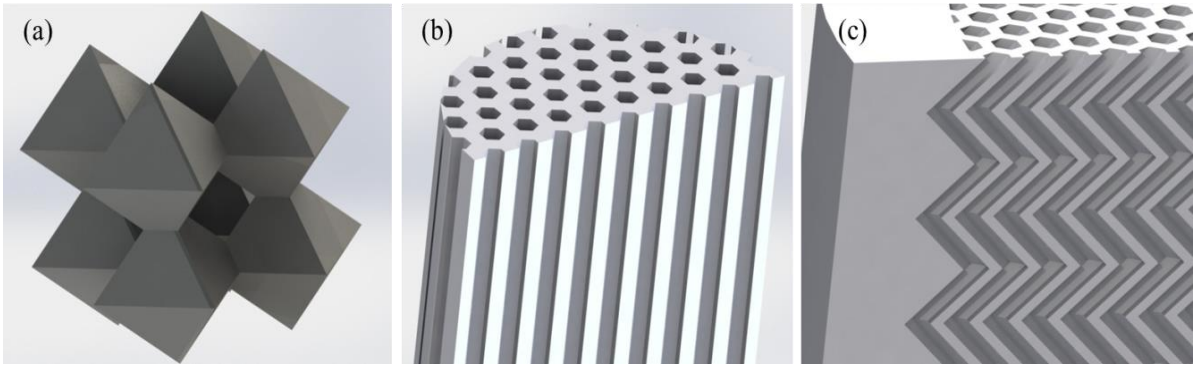

Figure 2.2. Printed packing arrangements: (a) octahedra in a simple-cubic configuration (SC), (b) hexagonal parallel channels (PC) and (c) herringbone channels (HC)

Additionally, two column designs containing channels were printed, a parallel channel column (PC, Fig. 2.2b) containing hexagonal channels arranged in a triangular pitch and a herringbone channel (HC, Fig. 2.2c) column. The HC was identical to the PC column except that it incorporated a tortuosity of $\tau = 1.15$. While their internal surface areas were comparable, the key difference between these two columns and the SC column is that channel-based columns do not allow for radial dispersion within the packing. It is also worth noting that the file sizes of the resultant PC and HC CAD models were significantly smaller than for the SC columns because the structures can be effectively described in only two dimensions rather than the three required in the case of bead packings.

The flat-to-flat distances of both parallel channel models were set to 150 μm. The centers of the channels had to be 500 μm apart for the structure to be mechanically robust and for the channels to be adequately separated. All of the produced columns were all-in-one parts, with integrated fast protein liquid chromatography (FPLC) tube fittings, flow distributors and channel walls.

The printed columns were cylindrical with internal diameters of 16 mm and a wall thickness of 2 mm. For each internal geometry, columns with packing volumes of 1.0, 1.5 and 2.0 ml were created. A standard radial distributor with radial and concentric channels was designed at each end of the packings, with a gap of 100 μm separating the distributor from the channel walls in the case of PC and HC columns. In addition to the full columns, separate cutaway columns were created for each of the tested structures to allow convenient geometrical analysis of the printed features without the need to cut them later.

2.3 Experimental Methods

2.3.1 Column Design and 3D Printing

CAD models of the columns' packing and ancillary features were created on Solidworks 2012 (Dassault Systèmes, Paris, France). Stereolithography (.stl) files of the CAD models were then produced and transferred to the 3D printer. Because the columns were complex structures containing 10^5–10^6 beads, the limiting parameter for the column size (after the bead/channel diameters were established) was the size of the .stl files. The 1.5 ml SC (Simple Cubic) column, which required approximately 240 MB, was the largest file amongst the columns described in this chapter.

A 3DS Projet HD 3500 inkjet 3D printer that operates on the principle of UV curing of photosensitive, powdered, urethane-based oligomer resins, was used to create all the printed columns, using a resin called "Visijet X". Variations between the lateral and vertical printing resolutions were observed, meaning that the orientation of the columns during printing was important to the final resolution of the printed geometries, particularly in the case of PC and HC (Parallel and herringbone channels) columns, where resolution in the x and y (horizontal) directions was more important than in the z (vertical) direction.

Overhanging features of the 3D models must be supported by a proprietary paraffin wax during printing so all of the internal void volumes of the columns were filled with a support material during printing using a separate extruder. To remove this support material, hot water at 70 ^{o}C and 100% cylcohexane, were flushed through the column for 2 - 3 hours alternately, 10-15 minutes each, for 6-8 flushing cycles. The time taken by this procedure depends upon the internal geometry of the column; the higher extra-particle porosities that non-spherical particles afford lend themselves to easier (more rapid) support material removal.

2.3.2 Residence Time Distribution Studies

To test the flow properties of the printed columns, residence time distribution (RTD) studies were performed on all the printed columns, using an ÄKTAexplorer 10™ FPLC system along with an auto-sampler (GE Healthcare, Uppsala, Sweden). After the columns were de-waxed and equilibrated with 10 column volumes of pure water, a 30 µl pulse of 2 M NaCl was injected through the columns and the conductivity of the eluent was measured. All of the tests were conducted at a superficial velocity of u = 298 cm/hr^{-1}. The resultant conductivity peaks, which

were skewed Gaussian curves, were analyzed using the method of moments[123]. In all cases, a minimum of 50 data points were used to form the Gaussian peaks and calculate the moments.

The injection volume, even in the case of the smallest column, was under 6% of the void volumes, therefore its contribution to the first moment can be neglected [124,125]. The mean residence volume, μ_1, the variance, σ^2, and the skewness, γ_1, of the RTD profiles were calculated using the moment method [123]:

$$\mu_1 = \frac{\int_0^\infty \kappa v \, dv}{\int_0^\infty \kappa \, dv} \qquad \textbf{Eq 2.1}$$

$$\sigma^2 = \frac{\int_0^\infty \kappa (v - \mu_1)^2 \, dv}{\int_0^\infty \kappa \, dv} \qquad \textbf{Eq 2.2}$$

$$\gamma_1 = \frac{\int_0^\infty \kappa (v - \mu_1)^3 \, dv}{\sigma^3 \int_0^\infty \kappa \, dv} \qquad \textbf{Eq 2.3}$$

where κ is the conductivity measurement and v is the flow volume. The dimensionless residence volume, θ_r^{exp}, was calculated as follows:

$$\theta_r^{exp} = \frac{\mu_1}{V_{VOID}} \qquad \textbf{Eq 2.4}$$

where V_{VOID} is the designed void volume. A dimensionless residence volume of $\theta_r^{exp} = 1$ would signify that the design and experimental void volumes are identical, implying that good replication of the designed features was achieved during printing.

The design, printing and testing methods outlined in this section serve as the template for the subsequent experimental studies in the project, in which individual parameters of the packing structure were investigated in greater detail.

2.4 Results and Discussion

2.4.1 Resolution Tests

The relevant dimensions of internal microstructures of the packing were determined through a series of geometrical tests. A series of small cutaway sample packings (e.g. Fig. 2.3a) were produced. The printed test parts were then analyzed with a compound light microscope to determine the minimum printable feature size for a given printer technology.

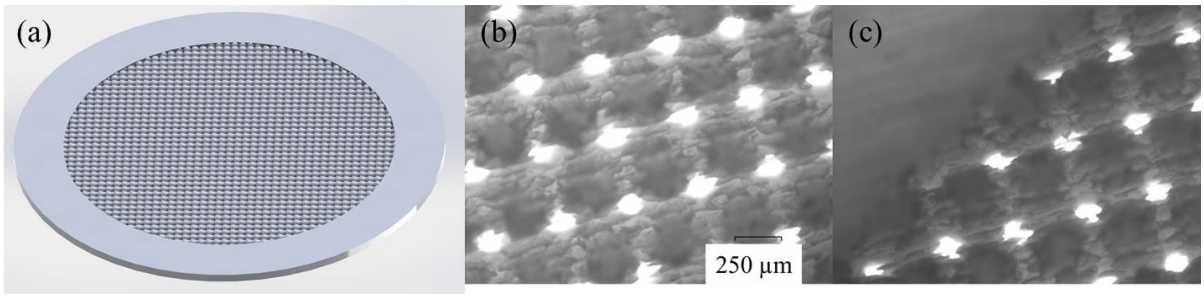

Figure 2.3. (a) CAD Model and compound microscope images of test parts with spherical particles with 400 µm diameters in the (b) bulk region and (c) wall region

Based on sample parts with spherical elements, a minimum sphere radius of 200 µm (Fig. 2.3b,c) was necessary for two reasons: for the printer to reproduce elements with a spherical shape and for the pore sizes to be large enough to remove support materials from designed void channels. Both these considerations are highly dependent on the element shape. Non-spherical elements could produce porous structures with smaller characteristic dimensions.

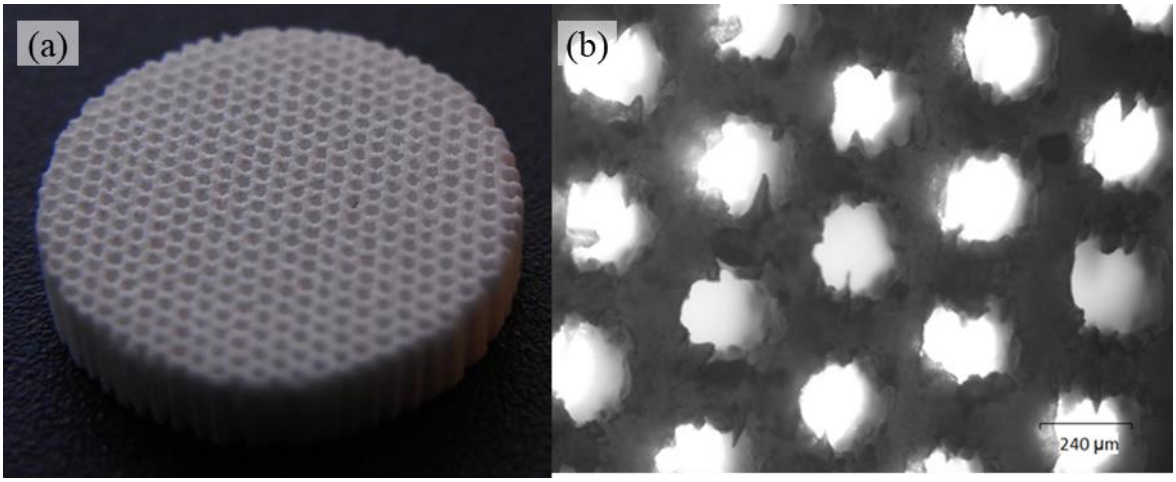

Figure 2.4. Test part with hexagonal pores with a 120 µm apothem (a) CAD model and (b) microscope image

For monolithic structures with hexagonal pores, the minimum apothem (i.e. inner radius of the hexagonal pore) was in the range of 120 µm, as shown in Fig. 2.4. This smaller dimension could be attributed to two potential reasons: Unlike geometries with particle-like elements, all

layers of the part shown in Fig. 2.4a can be identical, leading to fewer (or identical) irregularities caused by the powder jet of the printer. Secondly, as the geometry does not contain any tortuous channels or any dead-zone regions, removal of support material was easier. This is in contrast to spherical particles, where support material from regions can be seen immediately next to two spheres as observed in Fig. 2.4b.

2.4.2 Full Column and Cutaway Model Printing

Figure 2.5 shows CAD designs and pictures of cutaway models of the three tested geometries: SC, PC and HC. The images show that not only the column macrostructures but also the microstructures of the CAD models were reproduced with reasonable fidelity by the printer. In addition to the porous bed geometry, the grooves for flow distributors and collectors can also be clearly seen.

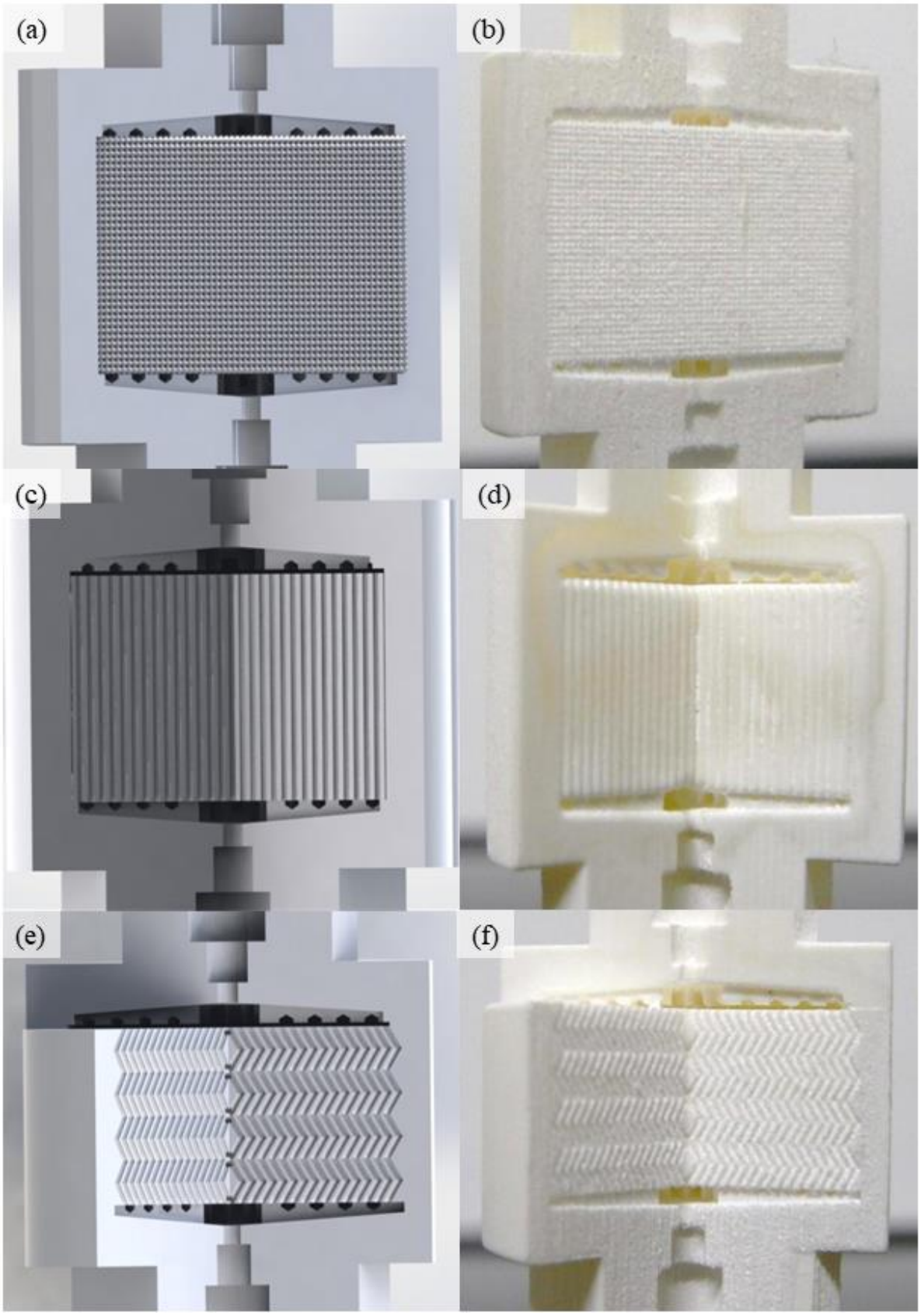

Figure 2.5. 3D-printed porous media columns. Left: CAD models, centre: 3D printed cutaways and right: microscope images of cutaway pieces. (a), (b) and (c) octahedra in a simple cubic arrangement, (d), (e) and (f) parallel channels and (g) (h) and (i) herringbone channels

Geometrical analysis of the cutaway models, shown in Fig. 2.6a, revealed good replication between the CAD (shown in Fig. 2.2) and printed models, with a mean error of 2.4% in the measured flat-to-flat and center-to-center distances of the octahedra. Image analysis of Fig. 2.6b reveals that the mean pore diameters of 296.4 μm with standard deviation of 3.8 μm.

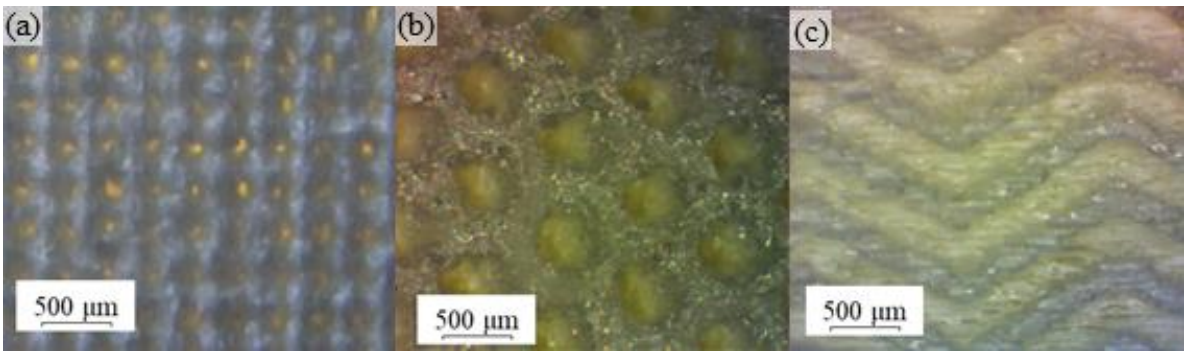

Figure 2.6: Microscope images of (a) simple cubic octahedra, (b) top view of PC geometry and (c) front view of HB column

While the positional accuracies of all models and columns were acceptable (i.e. positional errors of under 3%), the final definitions of the printed shapes varied for each geometry. It is well known that the spatial accuracy in i3DP is strongly dependent on the part geometry, especially for small features at the limits of the printer's resolution[126,127]. This is especially important for overhanging geometries, such as the octahedral packed beds and less so with the hexagonal channels. However, purely 2D images of individual test pieces cannot fully describe the final shapes of the printed pieces. The subject of geometrical analysis on multiple printed parts is studied in greater detail in Chapter 3.

What can be demonstrated using the cutaway and full columns is the ability to 3D-print single-piece columns that are robust for flow-tests and where the printed elements are placed accurately. Flow tests of the printed pieces showed the columns to be robust up to flow-rates of 20 ml/min ($u = 594$ cm.hr^{-1}). To achieve water-tight fittings up to these flow-rates, a smaller channel was designed below the fitting channel (shown in the top sections of Fig. 2.5 b, d and f). The smaller channel can therefore crimp ferrules (i.e. the external cones) of the 10-32 fittings and thus withstand back-pressures of up to 20 bar.

2.4.3 Residence Time Distribution (RTD) Results

RTD results can indicate whether the printer could faithfully reproduce the designed particle shape (octahedra) with the dimensions that were created for this study as spherical and octahedral beads packed in a simple cubic arrangement result in significantly different

porosities. Figure 2.7 shows a sample of the normalized RTD results of the tested columns with more than 200 data points defining each curve

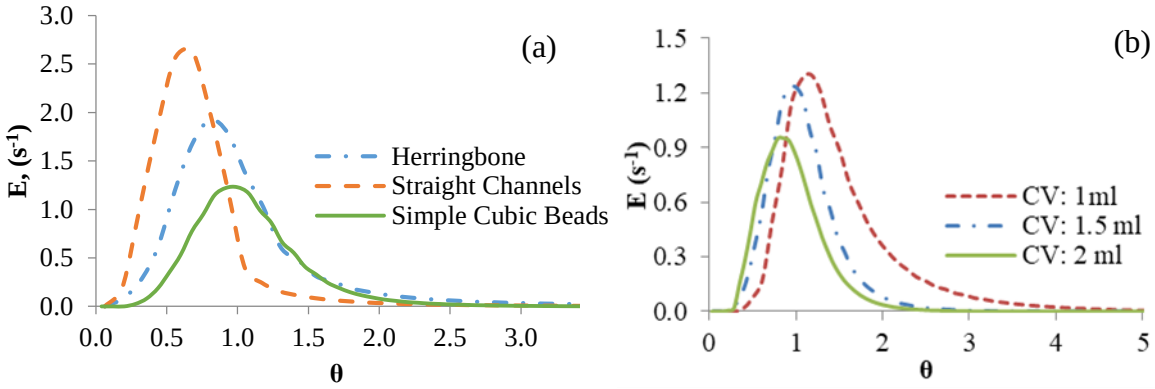

Figure 2.7. Residence time distribution profiles of (a) the three tested packing geometries in 1.5 ml cylindrical columns, (b) simple cubic bead columns at three different column volumes. The above RTD tests were conducted at superficial velocity u = 298 cm.hr^{-1}.

For the octahedral bead 'packed' columns, RTD measurements were in agreement with the designed porosity values. In all of the three tested column volumes the experimentally determined porosities were close to the designed value of $\epsilon_{exp} = 0.575$ ($\epsilon_{exp} = 0.678$, 0.569 and 0.551 for 1, 1.5 and 2 ml columns respectively). For a simple cubic packing with spheres, the design (theoretical) porosity was $\epsilon_{des} = 0.476$.

The low mean residence volumes of the herringbone and straight channel columns ($\theta_r^{exp} = 0.82$ and 0.68 respectively, using Eq 2.4) indicates that a substantial portion of the internal void volumes in the column was not accessed by the tracer pulse as it transited the column. Because these two column geometries did not allow for any radial distribution between the channels themselves within the beds, this probably indicates poor inlet distribution, as discussed below.

2.5 Effects of Flow Distribution

2.5.1 Prototypes Containing SC and PC Microstructures

To test the effects of radial distribution on the columns, two additional columns were designed and printed. The two columns contained a square fractal distributor conceived by Benoit B. Mandelbrot, with the flow properties optimized by Tondeur and Luo[48]. The design of the distributor is explained in Chapter 2.5.2. The resultant columns therefore had a square cross-section. The aim of producing these two columns was to compare the effects of flow distribution and collection in a column design that allows for radial dispersion within the 'packing' (simple cubic packed beads) and designs with no radial dispersion (parallel

channels). Both the columns had a packing volume of 2 ml and had cross-sectional areas equivalent to the cylindrical columns. The RTD comparisons of the columns are shown in Fig. 2.8.

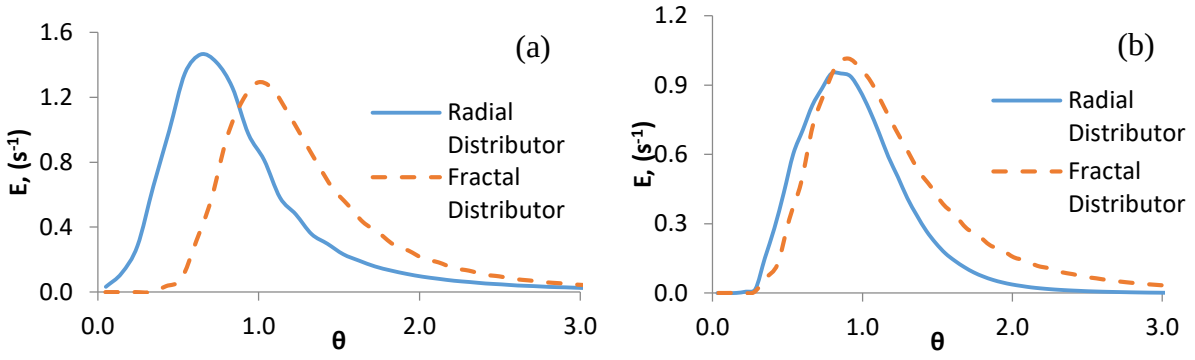

Figure 2.8: Comparison of 2 ml columns with radial and fractal flow distributors of a) straight channel columns b) simple cubic bead columns at u = 295 cm.hr^{-1}.

The differences between the effectiveness of the two distributors are highlighted in the parallel channel columns Fig. 2.8a where the mean residence volumes were θ_r^{exp} = 0.68 and 1.02 for the radial and fractal distributor, respectively. The parallel channels could not provide radial distribution within the column itself, so the effect of the entrance flow distribution on the RTD was significant. In the case of packed bead columns (Fig. 2.8b), only a minor difference was seen between the RTD's using each distributor because the bead packing already allowed for radial dispersion within the column. However, it is worth noting the greater peak asymmetry and tailing in the square cross-section column (peak asymmetry of γ_1 = 1.56 compared with γ_1 = 1.28 in the radial distributor in a cylindrical column). The tailing might result from the column shape, where dead-volumes might form in the edges of the cuboid.

2.5.2 Comparison of Flow Distributor Performance using Concentric Channel Models

As observed with the parallel channel (PC) and simple cubic (SC) geometries, the quality of radial distribution across the cross-section of the column and outlet collection can significantly affect the column performance. It is well established that the local interstitial velocities across a section of the column vary greatly depending on its radial position and result in varying local plate heights across the radial cross-section of a column[40,49,54], especially in preparative scale columns [41]. Additionally, back-mixing and band-broadening caused by poor flow distribution and collection is a significant cause of band-broadening[6,42,44]. Furthermore, these effects were not only observed in channel-based monoliths, where inlet distribution is directly linked to

column performance but also in packed bed columns where the radial dispersion caused by the porous bed can potentially reduce the effects of poor distribution.

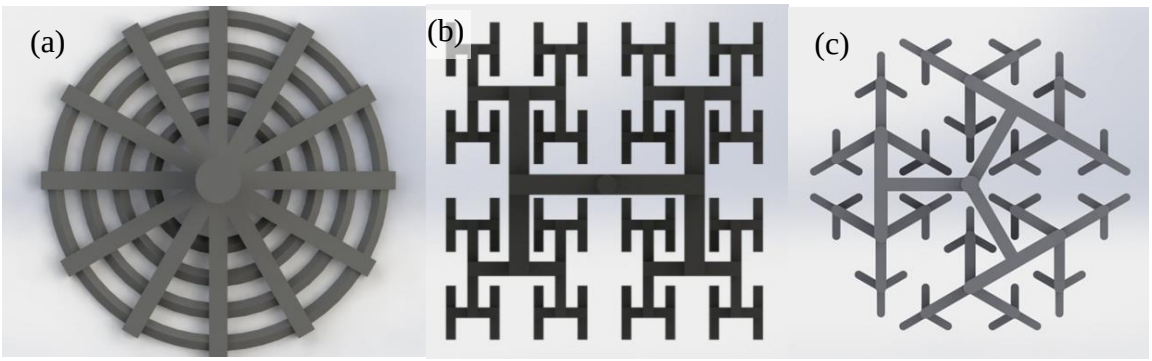

Figure 2.9. Inlet distributor templates: radial distributor (left), square fractal distributor (centre), hexagonal distributor (right)

To study the variation in effectiveness of flow distributor design, three different distributor templates were designed and printed. A standard radial distributor shown in Fig. 2.9a was used in cylindrical columns with the diameters of the radial and concentric channels being 300 µm and 250 µm, respectively. A square fractal distributor (Fig. 2.9b) derived from the Mandelbrot H-tree [47] was printed for a square cross-section column. The H-tree is a self-similar branching structure that can be used as a distributor across a square pitch of 4^n nodes where n is an integer. Unlike the template shown in Fig. 2.9b, which contains only 64 nodes for clarity of presentation, the printed models contained 1024 nodes, each comprising a square with a 250 µm side. Additionally, a hexagonal distributor (shown in Fig 2.9c), loosely based on the H-tree model was also designed and printed. In each case, the column cross-sectional area was A = 2.01 cm^2, corresponding to a cylindrical column with an internal diameter of 1.6 cm, as designed in the proof-of-concept studies. In the case of the square and hexagonal distributors, the proportions of the cross-sectional areas of bifurcating branches followed Murray's law [128].

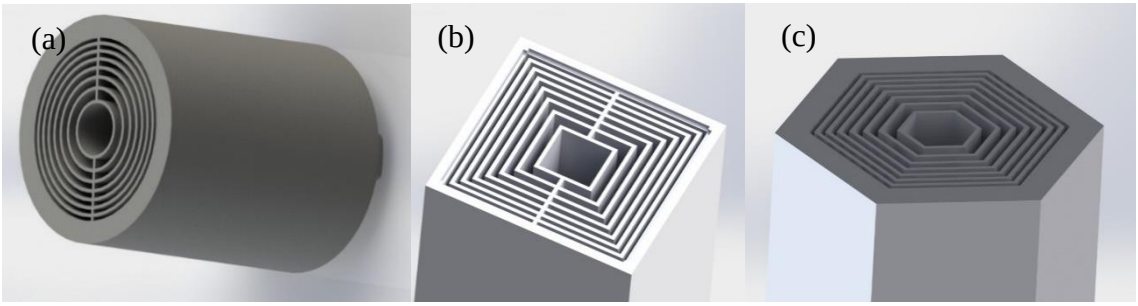

Figure 2.10. Concentric partitioning of columns for (a) radial, (b) square fractal and (c) hexagonal distributors

To determine the effect of each distributor alone on the velocity profile across the column cross-sectional area, no porous packing was included. Instead, the column was partitioned into

eight separate concentric channels as shown in Fig. 2.10 with a 300 µm thickness wall separating the channels. The geometries were designed such that the total cross-sectional area of each channel would be identical within a structure. With the appropriate distributor located at the inlet of the column, a separate outlet fitting was designed to individually collect the outflow from each channel in the column, with each of the outlet fittings connected to a measuring cylinder. A vertical gap of 100 µm was left between the outlet nodes of the inlet distributor and the partitioning walls. After the internal support material was removed, a peristaltic pump was used to flow pure water at 10 $ml.min^{-1}$ through the column for 10 minutes. Based on the volume of water collected in each receiving measuring cylinder and the cross-sectional area of each section, a velocity profile was calculated for each of the distributor designs. Figure 2.11 shows the average normalized velocity for each concentric section $u/\bar{u}$ in relation to the radial positioning of the section r. The measurements were made in triplicates and the error bars represent two standard deviations of $u/\bar{u}$.

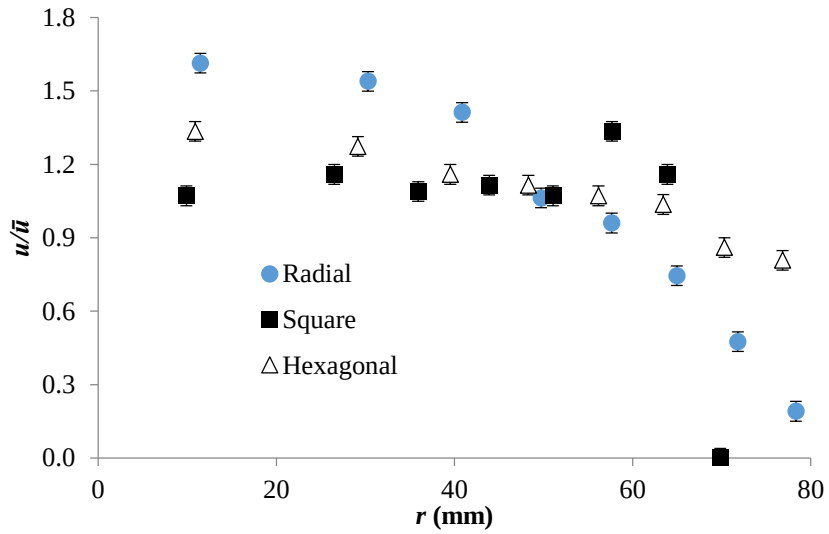

Figure 2.11. Radial velocity profiles of the three tested distributors

Poor distribution across the cross-section was observed in the case of the radial distributor, with a near perfect parabolic velocity profile (R^2 = 0.992) and very little fluid flowing through the outer channels of the column. In contrast, in the fractal distributor used for the square cross-section column, fluid velocity was generally uniform across the column cross-section but with significant variation between the channels. The noise seen in the data could be caused by the rugosities within the channel having a greater effect on the intricate network of fine channels. A minor printing inaccuracy in a parent branch could result in major variations in flow rates across its daughter branches because the distributor was bifurcating in nature, whereas errors

in printing the radial distributor containing larger channels could have been be self-correcting because they were radially interconnected. The anomaly seen in the outermost section of the square cross-section column can be attributed to insufficient wax removal completely blocking fluid flow through the outermost concentric region. The hexagonal distributor provided a velocity profile with a slight linear gradient that was directly correlated to the higher concentration of outlet nodes in the center of the column.

An important feature of this comparison is that the backpressures caused by the concentric sections were negligible compared with the backpressures observed in packed bed chromatography columns. While a porous bed can correct for the effects of poor flow distribution, the method used here is more sensitive to small variations in local flow rates. Moreover, the effects of flow distribution were isolated from porous bed effects using this method.

A limitation of the studied geometries is that the distributor designs were inevitably linked to the column shape. The effect of the latter is unknown and further studies would be necessary to design and optimize various distributor templates and dimensions for any given column shape. Additionally, in every printed column that contained a flow collector in this work, the collector design was identical to that of the distributor, whereas their functions differ, even if only subtlety. To further reduce extra-column effects, the features of the flow collectors could be optimized, independent of the distributor designs, but additive manufacture makes this entirely feasible. It is also worth noting that the three distributor templates tested here were periodically axisymmetric. To test non-axisymmetric templates that are produced through iterative algorithms, the columns could also be radially partitioned to determine and optimize flow distribution.

2.6 Conclusions

Single-piece columns containing ordered internal geometries, column walls, distributors and fittings were produced using an inkjet 3D printer. This is the first time, to my knowledge, that such porous media columns and associated column features have been designed and created using 3D printing. Octahedral beads and hexagonal pores with apothems of 115 and 150 μm respectively, were designed and printed. Columns with internal diameters of 16 mm and volumes of up to 2 ml were designed for the prototypes. A method involving cyclohexane and warm water was devised to reliably remove support material from the columns' internal voids.

No internal or external structural defects were observed at the tested velocities (maximum superficial velocity, u = 594 $cm.hr^{-1}$), displaying the structural robustness of the printed columns at flow rates necessary for preparative scale separations. Geometrical analysis of cutaway parts showed that the elements of the columns' microstructures were reliably recreated by the 3D printer. RTD tests of the columns showed that the design and experimental void volumes matched in all but two cases. In these two cases, it was observed that the inlet flow maldistribution was affecting the column performance.

These proof of concept models established a set of working parameters with regard to the column and packing dimensions as well as printing and testing methodology for the columns which were used to carry out the rest of the studies herein on the flow properties of 3D printed columns. The results of this study were published in the Journal of Chromatography A[129].

3. Ordered Packings with Control over Geometrical Parameters

3.1 Introduction

An overwhelming majority of liquid chromatographic separations, across scales and applications are performed on packed bed columns[2]. The exact geometries and particle placements within the columns are inherently random and practically impossible to reproduce [130–132]. These disadvantages associated with packed beds are all inherent to the geometry and packing method itself. Furthermore, the bulk-properties of the porous beds are inevitably linked to one another and dispersion effects of an individual geometrical property is often difficult to isolate.

The previous chapter established the concept of facile, single-piece columns 3D-printed with ordered porous beds. This chapter aims to demonstrate the efficacy of 3D-printed ordered particle packings and the ability to tailor and study individual geometrical properties in isolation. In Section 3.2, the effect of extra-particle porosity on dispersion was studied by varying the distance between particles. In Sections 3.3 and 3.4, the effects of ordered particle arrangments and non-spherical particle shapes were investigated.

It is worth noting that the word ‘particle’ as used here does not mean a discrete particle as used in a random packings. To create robust 3D-printed beds, the particles were designed to overlap and create a monolithic network of particle-like elements. All mentions of 3D-printed ‘particle’ packings in this thesis will refer to beds consisting of such elements.

3.2 The Effects of Bead Overlap on Dispersion

In fundamental studies of flow through porous media, a few all-encompassing parameters are usually used to describe the micro-structure of the porous structure. Among the more important parameters is extra-particle porosity which serves as a proxy for internal surface area, permeability, tortuosity and in some cases, packing heterogeneity[133,134]. In the case of monodisperse random close-packed spheres, extra-particle porosity is inextricably linked to the alignment of the pores, internal surface area and tortuosity of the packed bed but not to packing homogeneity for geometrical reasons[135]. However, well-known empirical

correlations used to relate the above parameters in packed beds may not apply for the non-spherical particles or the ordered structures that are possible to create with 3D printing. Unlike in random packing, using 3D printing to create ordered structures allows one to actually decouple porosity and surface area from particle shape, tortuosity, permeability and arrangement. This chapter investigates the effects of extra-particle porosity in isolation from these other parameters, using the concept of particle overlap.

For the packed bed columns used in the proof of concept studies in Chapter 2, it was necessary to align the particles in such a way that their vertices were overlaying to produce a physically stable structure in which the positions of the beads were fixed. An overlap factor, α can be defined as:

$$\alpha = \frac{S}{D_{ext}} \qquad \textbf{Eq 3.1}$$

where S is the distance between the centers of two adjacent particles and D_{ext} is the external diameter of the particles. While an overlap of α = 1.40 was determined through trial and error to be sufficient to produce a mechanically robust model, α can also be used as a parameter that is deliberately designed to control extra-particle porosity to gain insight into the behaviour of flow through porous media. Because the overlap factor determines the extra-particle porosity (seen in Fig. 3.1), it is now possible to vary the porosity of the column without varying the alignment of pores or what is traditionally referred to as packing quality. In this study, the effects of α on the column performance by printing four columns containing octahedral beads arranged in a simple-cubic configuration, with α = 1.40, 1.45, 1.50 and 1.55 were investigated.

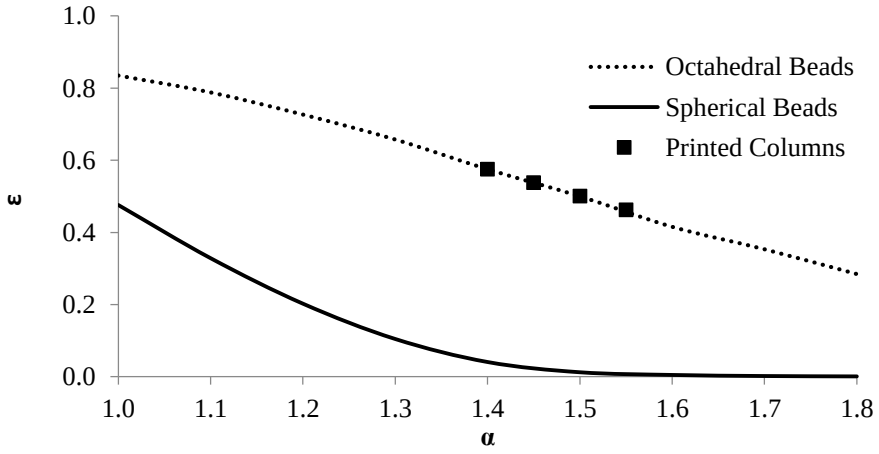

Figure 3.1: The effects of bead overlap on extra-particle porosity, ϵ in a simple cubic packing configuration

Figure 3.1 shows the four tested overlaps and porosities as well as the relationship of α on ε using spherical and octahedral particles, based on CAD design measurements. For spherical particles of an equivalent size, a minimum value of α = 1.1 is necessary to attach the particles in a porous bed. With α = 1.36, the pores between the spheres are no longer connected to one another and the column cannot be used for flow tests. A major advantage of using octahedral particles instead of spherical particles in this study is the wider ranges of ε and α values that can be designed and reliably printed.

The other dimensions and features of the columns were identical to the packed bed columns produced for the proof of concept studies except that the columns studied here had a column volume (i.e. the sum of void and packing volumes) of 2 ml. In addition to the four full columns, cutaway sample pieces containing packing with the four overlap factors were printed for geometrical analysis. The full columns were tested using the RTD method of moments described in Chapter 2, with 30 µl injections of 1 M NaCl in a pure water buffer at a superficial velocity of u = 298 cm.hr^{-1}, with the conductivity of the eluent measured downstream of the column outlet. In this case, the normalized peak skewness γ_1 was calculated in addition to the mean residence volume, as described in Eq. 2.1-2.4.

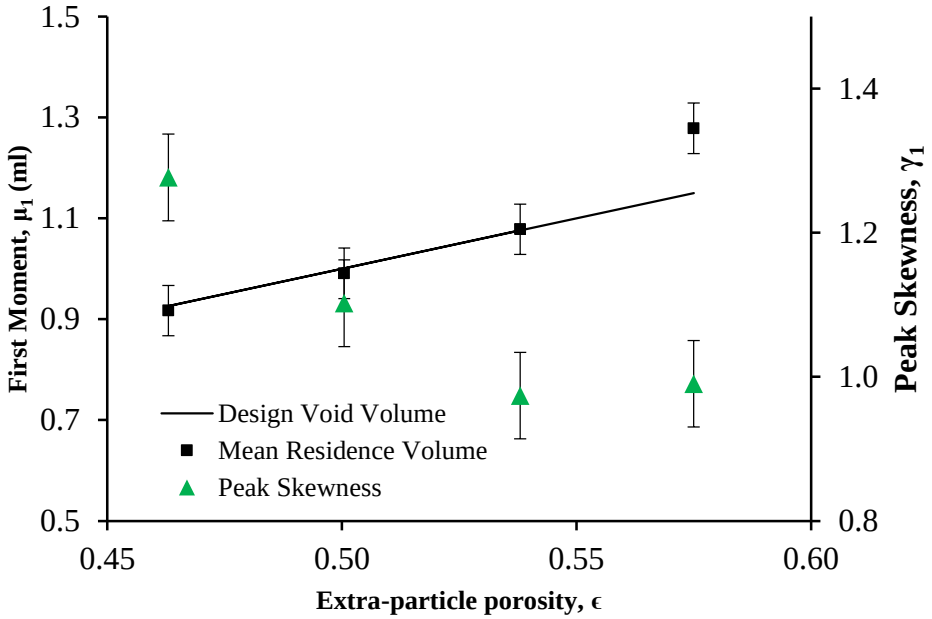

Figure 3.2: Mean residence volume μ_1 and peak skewness γ_1 of the four tested columns

The mean residence volumes, shown in Fig. 3.2 indicated that there was good fidelity between the CAD and the printed models because the experimental and design void volumes matched closely in all but one column. The columns with the lowest α value displayed a

higher void volume, potentially because of a printing inaccuracy. The peak skewness, an indicator of the chromatographic resolution, was inversely proportional to the column porosity in the four tested columns. The highest porosity model ($\alpha = 1.40$, $\epsilon = 0.575$) produced slightly more skewed peaks than the $\alpha = 1.45$ model, while nevertheless performing better than the other two columns. This could potentially be the result of small printing defects (as hinted by the difference between experimental and design void volumes).

A smaller skewness here, at the higher extra-particle porosities, thus represents smaller axial flow dispersions and therefore higher resolution. For packed bed columns, it is generally thought that more closely packed (i.e. lower porosity) columns tend to produce a higher chromatographic resolution [136]. This unexpected finding could be due to small rugosities (surface roughness) in the printed surfaces having a greater effect in smaller pores found in the columns with the higher overlap factors than in larger pores. In more porous geometries with larger voids (i.e. low α values), the proportion of the void volumes affected by surface roughness is likely to be lower. With smaller pores (high α values), a higher proportion of the flow volume is affected by the same degree of surface roughness.

Geometrical analysis of the sample pieces was also consistent with CAD models of the packing with a mean error of 2.4% in measurements of bead sizes, placement and pore sizes, showing good spatial accuracy of the 3D printer. However, piece orientation affected the apparent resolution of the printer, as shown in Fig. 3.3c. The cutaway model shown here was printed at a print orientation of 45^{o} to the x-axis. Experience has shown that with the Projet 3500 HD printer, the bottom portions of the printed part up to approximately 1 mm in height are not printed with good resolution (data not shown). In the case of printing full columns, this does not necessarily translate into poor replication of the CAD models because the lower portions of a column are invariably the column walls. However, in Fig. 3.3c shows that any intricate geometry should be built with a small vertical buffer on the print bed to eliminate this effect.

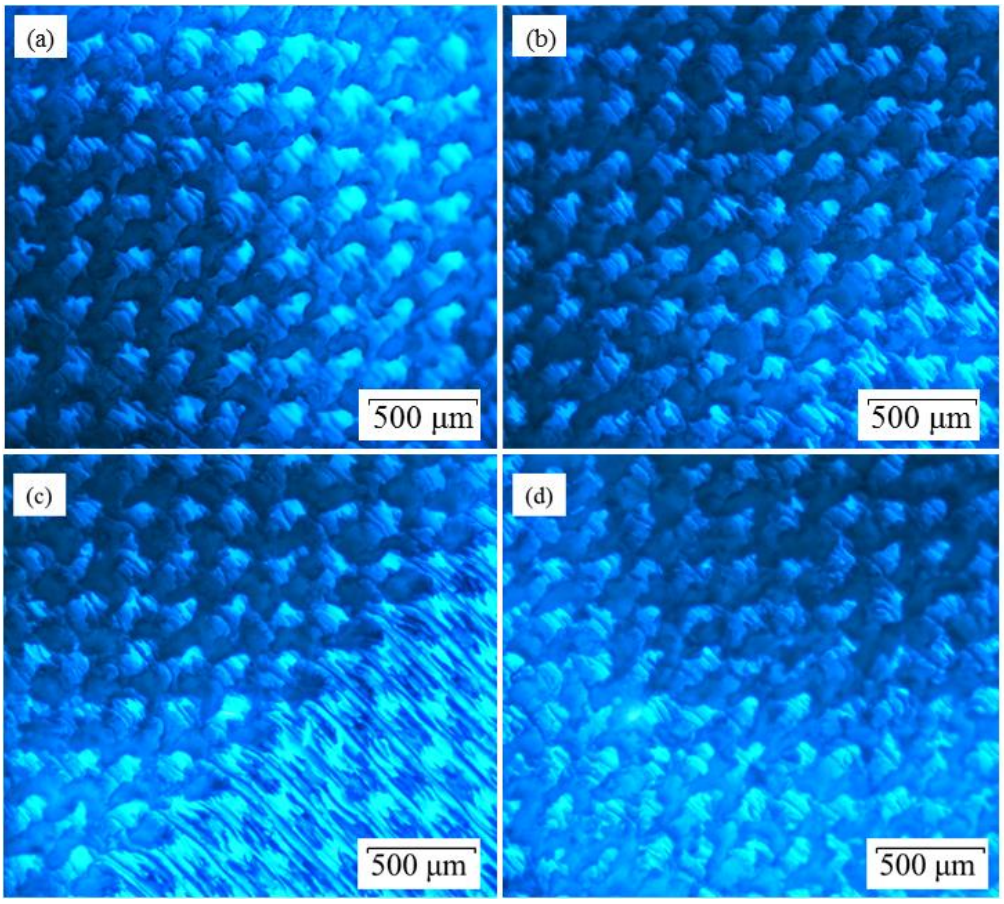

Figure 3.3: Microscopic images of cutaway sample pieces (a) α = 1.40, (b) α = 1.45, (c) α = 1.50 and (d) α = 1.55 with a magnification of 5x

In any event, contrary to the literature, the findings of this chapter show that porosity alone cannot be used as a standalone parameter that predicts column performance but that the homogeneity of flow channels within the column is the more important factor in determining column performance. The above work was published in International Labmate [137].

3.3 Effects of Element Arrangement

3.3.1 Introduction

The effects of particle arrangement on dispersion and band broadening in packed beds have long been studied using computational fluid dynamics. Computational results by Schure et al. have demonstrated the advantages of homogeneous beds in three dimensions, concluding that face-centered cubic (FCC) configurations of monodisperse spheres have much lower plate heights than do random close packings across a large range of reduced velocities [25,26]. Other computational studies have given similar results [73,74]. Wirth et al. experimentally

demonstrated the advantages of a FCC arrangement of silica particles [72,138] but experimental studies such as this are rare because of the difficulty of producing ordered beds in practice.

The potential advantages offered by ordered configurations of particles were further investigated by De Smet et al. and Li et al., who proposed the use of ordered arrangements of particles having shapes other than traditional spheres [28,29,139]. Their simulations predicted that axially elongated elements could improve chromatographic performance, but manufacturing limitations have made it impossible, until now, to test these shapes experimentally. The above studies do however, reveal the potential of ordered lattices of non-spherical particles, if they could be manufactured reliably.

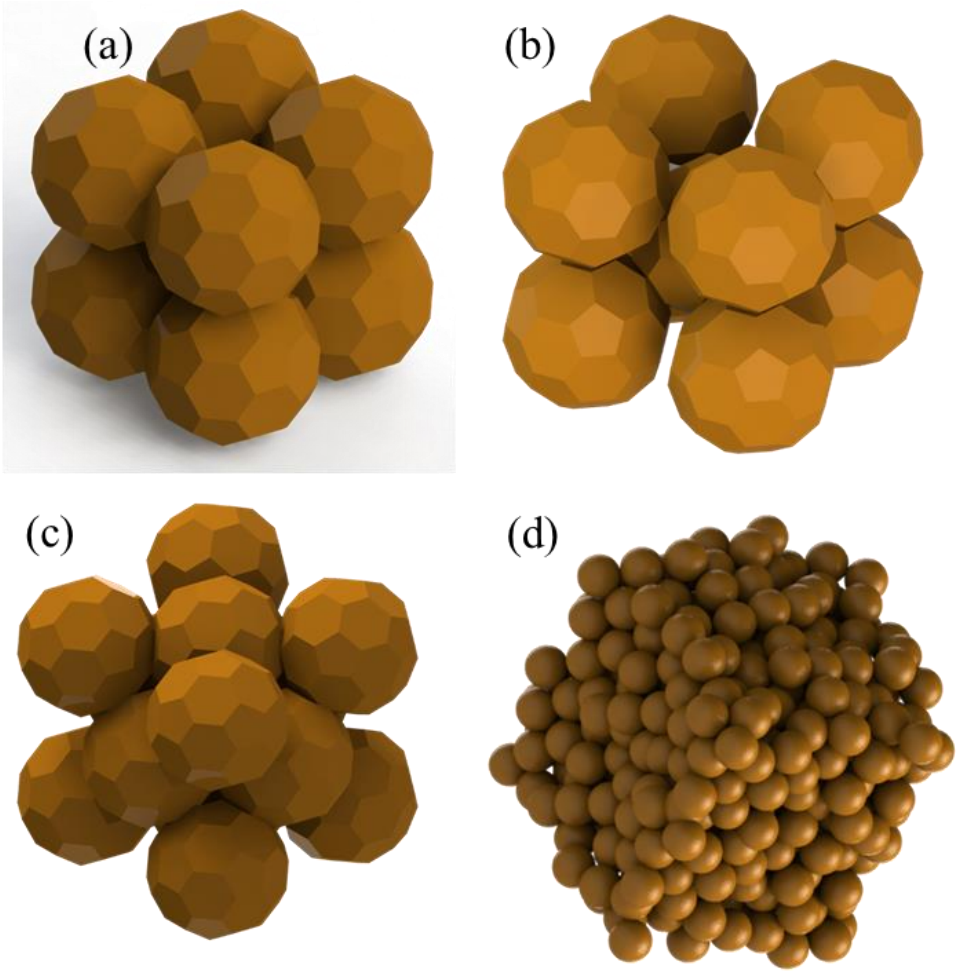

Figure 3.4: The three element arrangements tested with spherical particles: (a) simple cubic, (b) body-centered cubic (c) face-centered cubic and (d) random close packing

The effect of particle arrangement on band broadening was compared herein by designing truncated icosahedra, arranged in the three basic crystal lattice structures: simple cubic (SC), body-centered cubic (BCC) and face-centered cubic (FCC). Additionally, a random close packing based column was also designed. The Jodrey-Tory algorithm used to produce the

packing was provided by Dr. Siarrhei Khirevich[135]. The centerpoints of the packings were then used to place truncated icosahedra models in Solidworks 2013. All the sphere packing arrangements were designed with overlap factors of $\alpha = 1.10$. The unit cells used to generate the porous morphologies are shown in Figure 3.4.

The different arrangements were obtained using a constant equivalent diameter, D_E, of 579.8 μm, where the equivalent particle diameter, D_E, is defined as the diameter of an equivalent sphere having same volume as the truncated particle, V_P:

$$D_E = \left[\frac{6V_P}{\pi}\right]^{\frac{1}{3}} \qquad \textbf{Eq 3.2}$$

The resulting extra-particle porosities and specific surface areas for the different configurations are summarized in Table 3.1. Because of bead overlap, the porosities and surface areas do not correspond to the theoretical values for non-overlapping spherical particles. However, the relative orders of the three configurations are still identical in terms of porosity and specific surface area.

Table 3.1: Design parameters of spheres arranged in the three tested crystal lattice structures.

Element Arrangement	ε	S^{-1} (mm^{-1})
Simple cubic	0.370	8.66
Body centered cubic	0.283	9.42
Face centered cubic	0.193	9.77

3.3.2 Model Reproducibility

As with the bead overlap study, test models were printed to test the fidelity and reproducibility of the 3D printer. The models contained 8 × 8 × 2 mm samples of the five particle shapes considered (a typical sample containing 13 × 13 × 3 particles) in the same arrangements used in the full columns. To test variations caused by different orientations of the printed models on the printer bed, two models were printed in a single print job, with one model aligned with the x-y plane and the other along the x-z plane. To test print-to-print repeatability, these two models were then printed using separate print jobs.

Images of the printed beds were captured on a Leica TPS SP5 confocal microscope (Leica Microsystems, Wetzlar, Germany) using a HCX PL APO CS 10.0 × 0.40 dry UV objective. The auto-fluorescence of the printed resin itself was used to generate the images, using a blue excitation (488 nm) and a gain of 1050-1200 V, depending on the average z-depth of the specimen. Z-stacks of the sample packings were taken in increments of 10 μm to provide three-dimensional models of the printed parts. The overall stack depths were 250 μm to capture images of the upper portion (up to the equator) of the particles. Z-stack images were taken from both the top and the bottom of each test model.

The resolution and spatial accuracy of the printed spheres were measured from the circularity of their confocal cross-sections and the spatial relative error between CAD model and 3D printed artefact. The circularity, *C*, the analogue of the sphericity value used in 2D, is defined as the ratio between the circumference of a circle having same area as the shape, A_S, and the perimeter of that same shape, P_S:

$$C = \frac{2(\pi A_S)^{\frac{1}{2}}}{P_S} \qquad \textbf{Eq 3.3}$$

A circularity of $C = 1$ would indicate perfectly circular element cross-sections. The spatial relative error, *e*, was determined by comparing the theoretical distance between particle centers in the CAD model, $\bar{l}$, and the actual distance in the 3D printed artefact, l_c:

$$e = \frac{\left| l_c - \bar{l} \right|}{\bar{l}} \qquad \textbf{Eq 3.4}$$

A value of $e = 0$ would indicate ideal element placement and replication of the CAD models. Confocal images were converted into binary images using the open-source ImageJ 1.50h image analysis software (available from www.imagej.net) and the cross-sectional areas of the shapes, A_S, were determined. Also, an algorithm was created on Mathematica 8.0 (Wolfram, Champaign, IL) to calculate the perimeter of the sliced 3D printed shapes, P_S. The algorithm approximated the outer boundaries of the shapes using an appropriate polygon composed by linear segments that were 5 μm in length, from which the perimeter could be easily derived. The spatial relative error was determined by calculating the distance between the centroids of adjacent polygons in the confocal images.

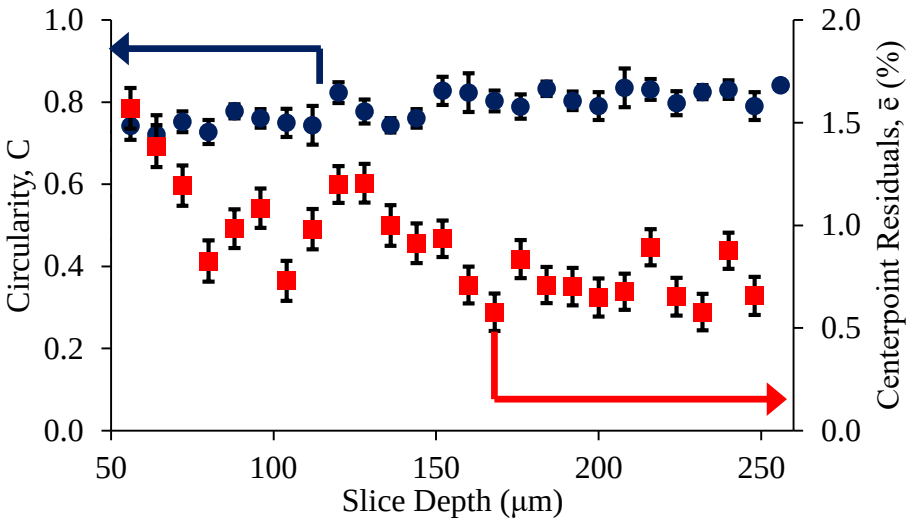

Figure 3.5: Circularity (C, in blue) and center-point errors (ē in red) of cross sectional images of sphere packing arrangements

The circularity and spatial relative errors were calculated for 64 spherical elements across the four sample pieces, as reported in Fig. 3.5. Overall, the circularity was relatively close to 1 for all the slices, while the spatial relative errors were well below 2%. These values indicate that the printed parts could be considered close replicas of the original CAD models, with features at the sub-millimetre scale reproduced with good accuracy and precision.

3.3.3 Single Piece Columns

Van Deemter curves for the printed columns were produced for a range of reduced velocities or Peclet numbers. The moment method was used to calculate the mean residence volume, μ_1, variance, σ^2, as in Eq. 2.1-2.3. In addition, the reduced plate heights, h, were calculated:

$$h = \frac{\sigma^2}{\mu_1^2}\frac{L}{D_E} \qquad \textbf{Eq 3.5}$$

where D_E is the equivalent diameter and L is the column length. The h values were plotted against the Peclet number, Pe:

$$\mathrm{Pe} = \frac{u\,D_E}{D} \qquad \textbf{Eq 3.6}$$

where u and D represent the superficial velocity and molecular diffusion of the NaCl tracer in water (1.99×10^{-9} m^2 s^{-1}), respectively. Conductivity values lower than 0.002 mS.cm^{-1} were

neglected from the calculation of the integrals, because this value was below the experimental error of the conductivity meter.

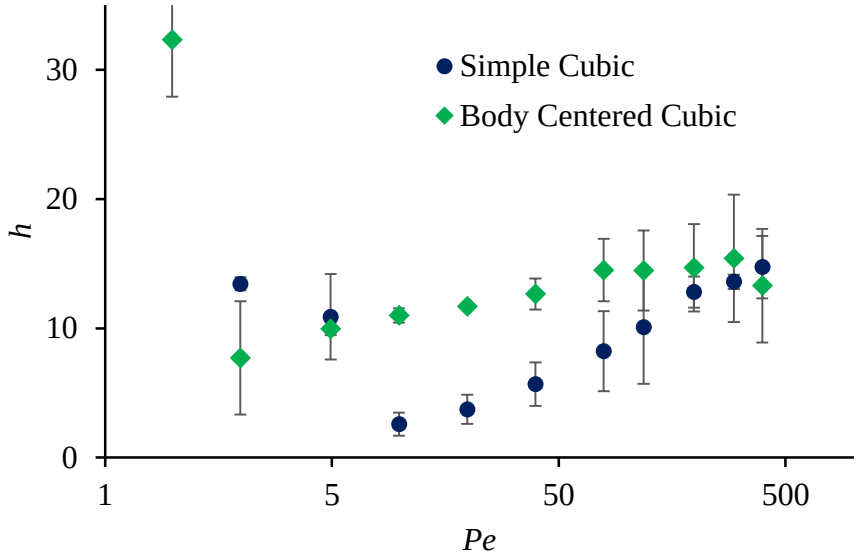

Figure 3.6: Van Deemter curves of initial single piece column models with spherical elements

Figure 3.6 shows the initial Van-Deemter curves with the SC and BCC columns. Tracer pulses from both columns showed significant tailing, resulting in high plate heights. Contrary to what is seen with CFD studies, the SC column produced lower plate heights than the BCC geometry. However, the first moment of the peaks also appeared to shift as flow rates were increased. The peak areas remained consistent across both geometries at all flow rates, meaning that this was not an artefact of the detector. Figure 3.7 shows the first moments, μ_1 across the tested flow rates:

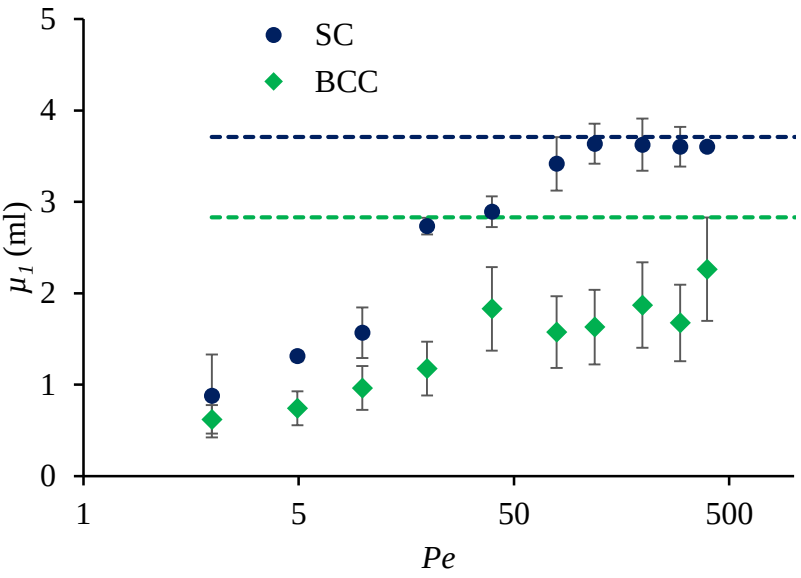

Figure 3.7: First moments, μ_1 of the two single piece columns as a function of reduced velocity. The dashed lines denote the ideal first moment values corresponding to the design void volumes

An ideal setup would see all the first moments close to their design void volumes (shown as dashed lines). The lower observed first moments indicate that the tracer was not accessing significant portions of the porous bed, especially at lower flow rates. A possible explanation is the poor flow distribution of the radial distributor used in this column design. This effect is especially acute at lower flow rates (and lower back-pressures). μ_1 values of the SC column shows this effect up to Pe = 100, after which the back-pressure produced by the bed may have been sufficient for good flow distribution.

Another potential reason is the presence of residual support material in the porous bed. In geometries such as BCC arrangement, clearing the smaller and more tortuous pores of a viscous support material is especially challenging. This could potentially explain the maximum μ_1 of the BCC column being 26% lower than the design void volume. The high surface tension and viscosity (when molten) of the paraffin wax used as a support material during printing help it support overhanging portions of the geometry during the print process. When creating a porous geometry with high surface areas and small pore sizes (in the range of 100 µm) however, the support materials properties also hinder the removal of support material from the internal microstructures of the printed columns. The resulting void geometries therefore may not replicate the CAD designs and result in excess band-broadening.

An issue with using the single-piece columns described in Chapter 2 was the inability to distinguish band broadening caused by the internal printed flow distributors from that caused by the porous bed structure. The largest contributor to extra-column volumes are the flow distributors and collectors (representing a total of 130 µL calculated from the CAD designs). The accessible volume within a flow distributor, and in turn its effectiveness, depends heavily on the back-pressures created by the porous beds.

To account for the effects of the flow distributor, a control piece containing just the FPLC fittings and a flow distributor and collector (without a porous bed) was 3D-printed. Due to the absence of back-pressure caused by the porous bed, the radial distributor did not distribute fluid across the cross-sectional area of the control piece. Instead, the tracer passed directly from the central entry channel of the flow distributor to the (central) outlet channel of the flow collector without passing through the distributor branches. The first moments were indistinguishable from first moments shown in the setup by zero-volume unions (and matched the volumes of the PEEK tubing and detector cell's). The purpose of the control piece (to account for extra-column band-broadening) was therefore nullified.

3.3.4 Column Frit Arrangement

An alternative approach was devised to measure and minimize extra-column band broadening. A screw-in assembly consisting of three pieces was created: One piece contained the packing in the form of an open cylinder and two caps were designed to be screwed into the two ends of the cylinder, as seen in Fig. 3.8. For each cap, a stainless-steel frit with pores of 18 µm and a thickness of 3.5 mm was placed between the inlet point and the plane of contact with the packing cylinder. The threads on the cylinder and caps were designed with the Helix feature on Solidworks 2013 and used an offset of 50 µm. To ensure a watertight assembly between the three pieces at flow-rates greater than 5 ml/min, silicone sealant was used at the edges of the connecting threads.

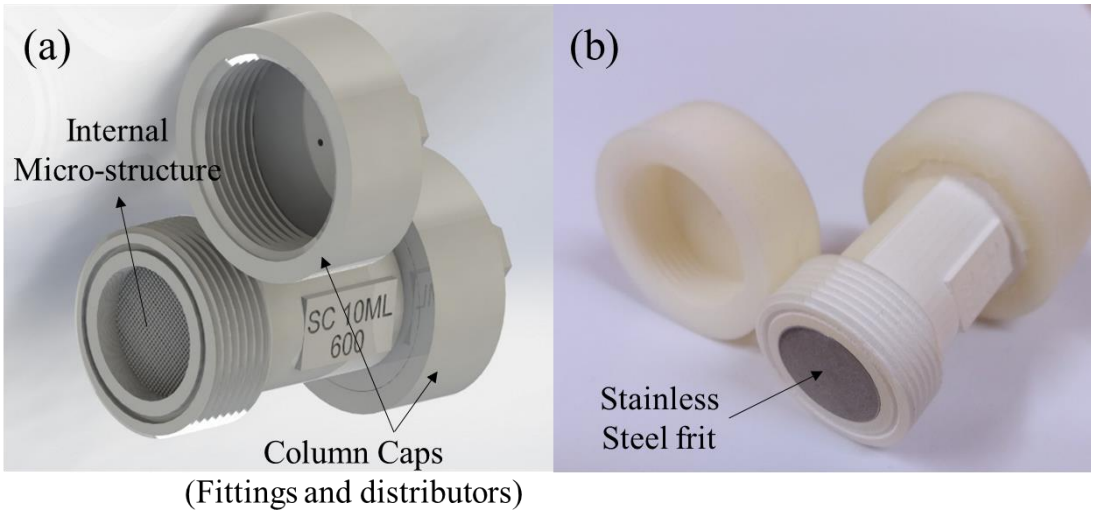

Figure 3.8: (a) CAD rendering of 3D column assembly for a column containing spheres in a simple cubic arrangement, (b) 3D-printed column assembly, the stainless steel frit is visible at one end of the column.

The goal of this arrangement was to more accurately compare the three geometries by isolating the band-broadening effects in the packing region from the total system band-broadening. The frit arrangement helped in the following ways:

- Minimizing dispersion in flow distributor: The back-pressure caused by the set of frits (roughly 2 orders of magnitude greater than the printed bed itself) could ensure greater flow homogeneity in distribution and collection. Additionally, differences in flow distribution caused by small differences in back-pressures between the geometries themselves will be nullified.
- Measuring extra-column dispersion: A control piece consisting of a short cylinder with two spaces slots for the two frits was 3D-printed. The first moment was consistent with the void volume within the frits and connecting tubes across the range of tested flow-rates.
- Support material removal: In the single-piece setup, the molten paraffin wax would have to be flushed out the column through the 1 mm hole in the inlet or outlet. The preferential pathways created by the radial flow distributor also meant that preferential portions of the column were de-waxed. The wider cross-sectional area of the screw-in cylinder meant a 40-fold increase in cross-sectional area for the support material to flow through. The de-waxing process was therefore reduced from 3 hours to 15 minutes.

The Van-Deemter tests with 1M NaCl of the porous bed geometries in the frit assembly were performed using the method described previously. The first and second moments of the control assembly were subtracted from the overall system moments.

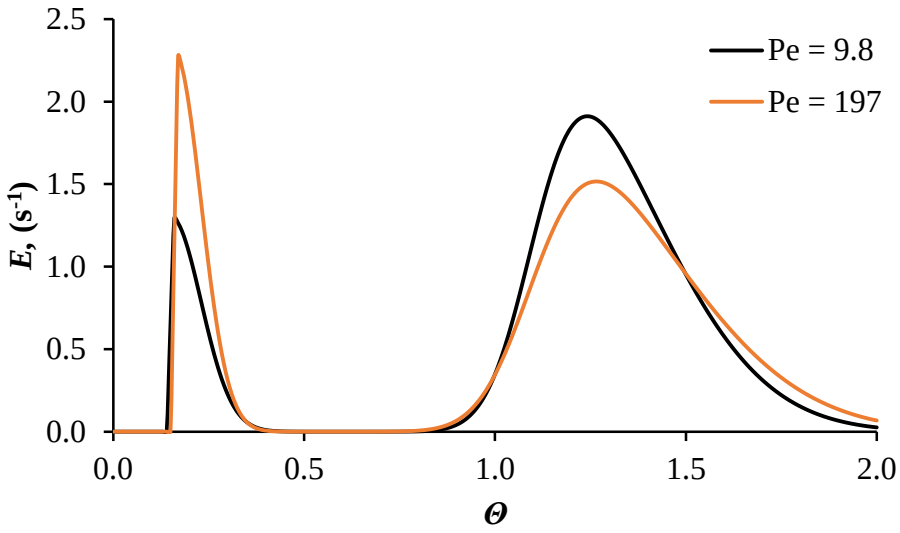

Figure 3.9: Dimensionless residence time distributions of random packing (RCP) column at *Pe* = 9.8 and *Pe* = 197

Despite the low extra-column dispersion of the frit assembly, the printed random close packing (RCP) column's plate heights were in excess of $h = 15$. The tracer pulse profiles for this column (two examples shown in Figure 3.9), showed severe channeling. A breakthrough curve at $\Theta = 0.2$ was observed for all reduced velocities. This clearly indicates a defect in the packing, either caused by a random distribution of pore sizes or by mechanical separation of two 'particles' in the printed piece, despite the overlap of $\alpha = 1.10$. For the RCP column, a 7 × 7 × 7 unit-cube of particles was patterned across the column (with an aspect ratio of 33) to maintain practical computation times during the design step. The column therefore consisted of a periodically patterned set of RCP unit-cubes. Any minor defect would be periodically repeated across the radial and axial directions of the column. Larger unit-cubes can be tested to overcome this issue. However, the current CAD setup does not allow for the three-dimensional placement of elements given their center-points, meaning that the 'particles' had to be placed manually in the unit-cell. The RCP column was therefore removed for this comparison of bed geometries.

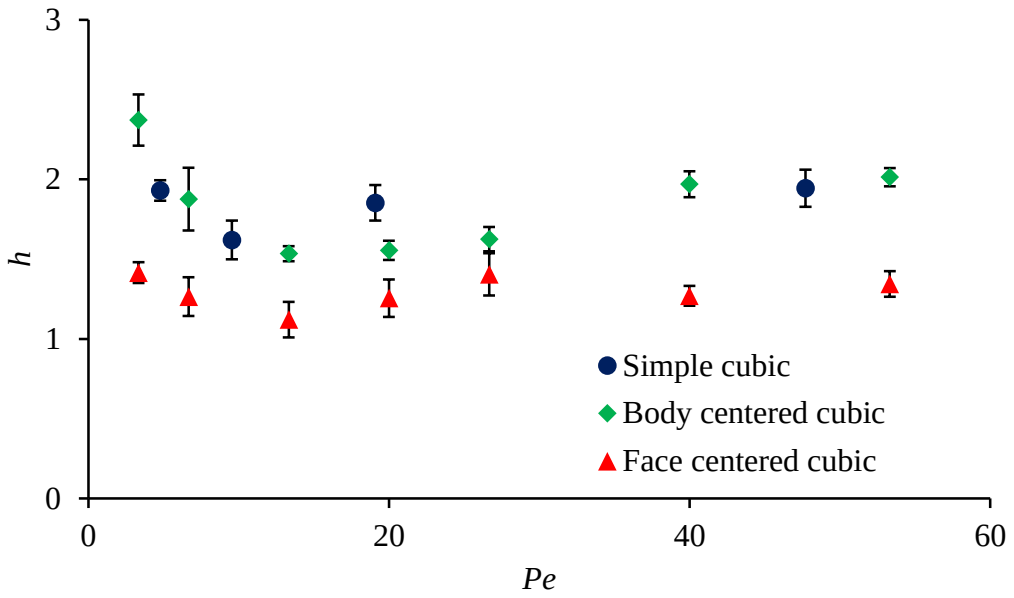

Figure 3.10: Reduced plate height, h plotted against reduced velocity, *Pe* for the three tested element arrangement with spherical particles

The FCC arrangement always displayed a significantly lower reduced plate height than SC at all *Pe* values investigated. The minimum reduced plate heights were 1.12, 1.53 and 1.62 for FCC, BCC and SC arrangements, respectively. The relative performances of the columns are consistent with predictions made in CFD studies [26,32,140], with the BCC arrangement providing a slight plate height improvement compared with the SC configuration. The FCC arrangement however, was reported to exhibit significantly lower plate heights than the other arrangements in the more recent computational studies, which report h_{min} values lower than 0.1 even in no-slip conditions. This is attributed to a flow uniformity that is markedly higher in FCC packings compared with both SC and BCC arrangements. The pore sizes in an FCC packing are also significantly smaller than in the other two configurations.

While a significant decrease in h_{min} for the FCC configuration was also observed in the present experimental results, this improvement was not as marked as seen in the recent CFD studies. A possible reason for this is the presence of surface micron-scaled roughness in the 3D printed models, which would be disproportionately larger on the relatively small flow paths present in the FCC arrangement than in BCC and SC. The high flow uniformity mentioned by Li et.al could therefore be partly impeded. The effects of the surface roughness are expected to diminish as the resolution of 3D printing technologies improves.

Another observation can be made on the value of the reduced velocity corresponding to the minimum plate height, Pe_{min}. In our experimental evaluation, all Pe_{min} consistently ranged

between 10 and 15, while their computational counterparts display values for the FCC arrangement significantly higher than for the BCC and SC configurations. However, the FCC column produced the least dispersion at all tested reduced velocities.

3.4 Element Shape

In addition to comparing element arrangements, as in Section 3.3, 3D-printing can also be used to create porous beds with a wide range of element shapes. It is commonly acknowledged that highly spherical particles produced more homogenous packings and that non-spherical particles are detrimental to column performance[130]. While this is true with random packing, the effects of ordered, non-spherical particles is not well studied. Computational studies have hinted at the possibilities of non-spherical element shapes being more advantageous in minimizing dispersion [29,139] but no experimental studies of ordered non-spherical particles have been conducted. This chapter describes the comparison of dispersion observed in a range of polygon shapes that were arbitrarily chosen. The frit assembly setup, as well as column dimensions described in Section 3.3 were used to 3D-print a set of columns with different element shapes.

In order to conduct a rational comparison between the different shapes, several geometrical properties such as the size and orientation of the elements must be identical across the geometries. A simple cubic arrangement was the only morphology that was considered when studying the effect of particle shape. This decision was mainly made for geometrical reasons, as this arrangement easily lends itself as a uniform template in which the various polyhedra could be systematically and reliably truncated, thus enabling us to systematically compare the effect of element shapes on chromatographic performance.

The equivalent sphere diameter D_E, as defined in Eq 3.2, of 579.8 µm was used for all printed models. The truncated particles and their resulting SC arrangements were geometrically characterized using the Wadell sphericity, ψ, defined as the ratio between the surface area of a sphere with an equivalent volume and the wetted surface area of the unit particle in its truncated form, A_p:

$$\Psi = \frac{\pi^{\frac{1}{3}}(6V_P)^{\frac{2}{3}}}{A_P} \qquad \textbf{Eq 3.7}$$

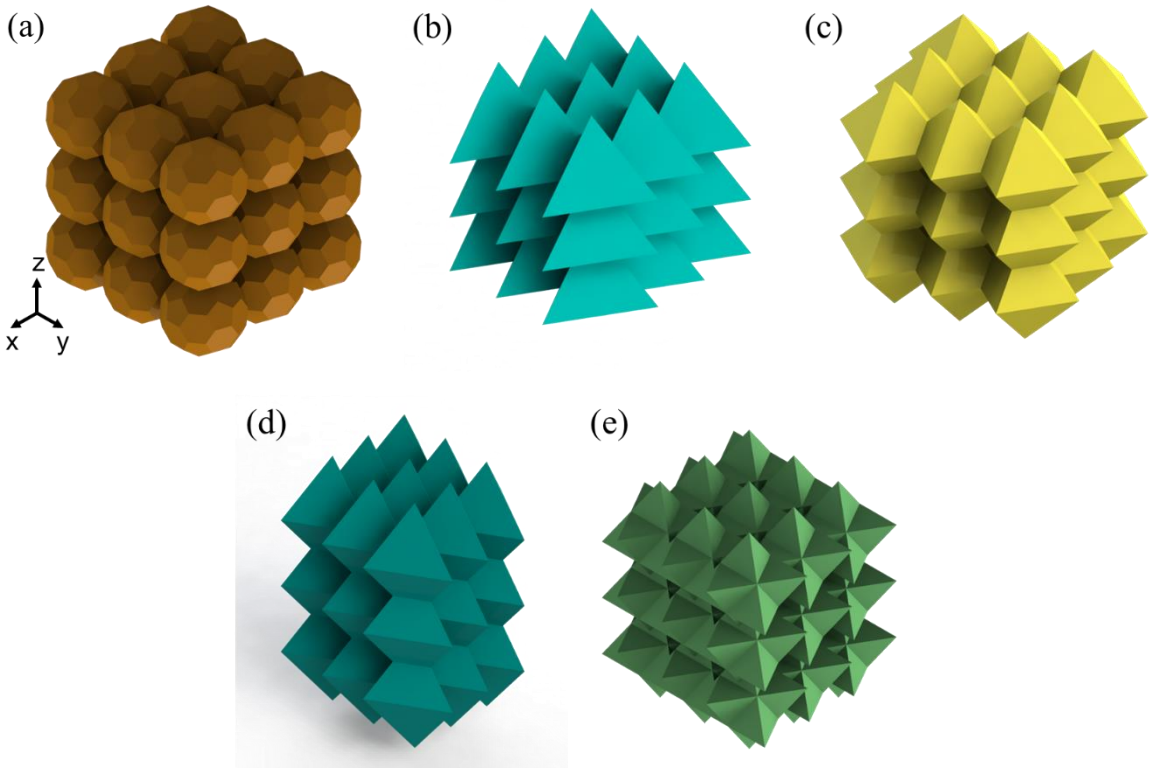

Figure 3.11: CAD renderings of 'packing' units used in this study: (a) truncated icosahedra (spheres), (b) tetrahedra, (c) octahedra, (d) triangular bipyramids and (e) stella octangulae.

Figure 3.11 shows the tested element shapes that were printed for this study. Two basic platonic solids: tetrahedra and octahedra (Fig. 3.11 b and c) along with two composite geometries: dual tetrahedra and stella octangulae (Fig. 3.11 d and e) were chosen as the four arbitrary, non-spherical element shapes to be compared against spherical elements in an SC arrangement (Fig. 3.11 a) tested in the previous section.

Table 3.2: Experimental dimensionless residence times at a superficial velocity of u = 235.8 cm.hr^{-1} (Pe = 191, Q = 10 ml.min^{-1}) and minimum plate heights h_{min} of the tested element shapes.

Element Shape	θ_{exp}	h_{min}
Spheres	0.987 ± 0.004	1.62 ± 0.20
Tetrahedra	1.012 ± 0.001	1.56 ± 0.07
Octahedra	1.008 ± 0.003	1.72 ± 0.14
Triangular bipyramids	0.991 ± 0.005	1.68 ± 0.09
Stella octangulae	0.989 ± 0.004	1.81 ± 0.09

The θ_{exp} values (i.e. the proportion of design and experimental void volumes), shown in Table 3.2 shows good agreement for all tested columns, indicating that the void spaces were defined in accordance with the CAD models. The minor discrepancies between design and actual column volumes could arise from imperfections in the 3D printed artefact or from small traces of residual support material that were not removed during post-processing of the columns.

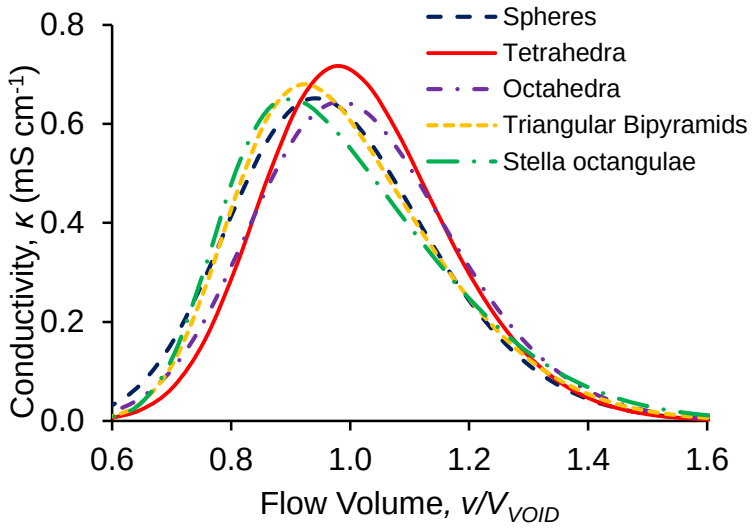

Figure 3.12: Residence time distribution curves (conductivity against flow volume) for tested particle shapes at Pe = 19 (superficial velocity of u = 5.9 cm.hr^{-1}).

Figure 3.12 shows a set of typical RTD profiles of the tested element shapes. The basic platonic solids (tetrahedra, octahedra and spheres) exhibited the lowest peak skewness (γ < 1). Composite geometries such as triangular bipyramids and stella octangula displayed markedly higher peak skewness (γ >1.5), indicating a greater degree of tailing of the curves, possibly caused by recirculation or stagnation zones within the columns. At a reduced velocity of Pe = 19, it is clear that tetrahedral elements, which were topologically the

simplest amongst the tested elements, also displayed the most favorable dispersion characteristics.

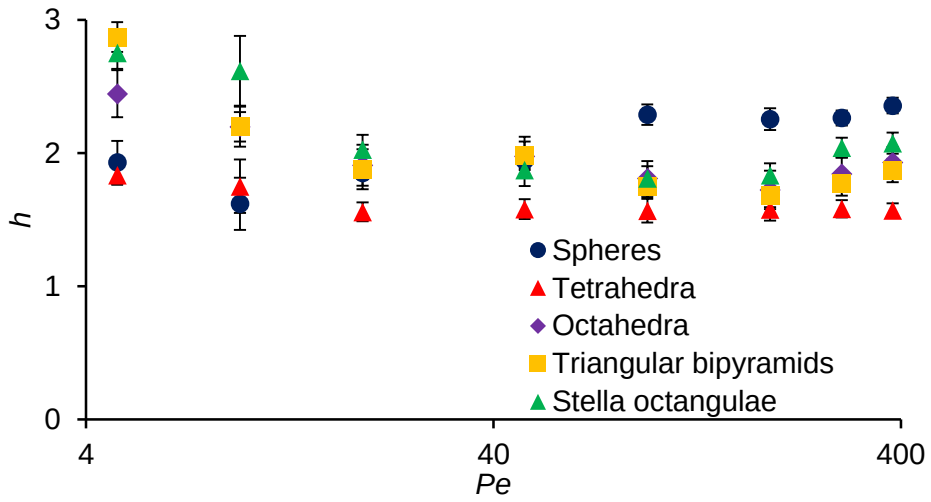

Figure 3.13: Reduced plate height, *h* as a function of reduced velocity, *Pe* for the five tested particle shapes.

The reduced plate heights for the particle shapes investigated were determined using Equations 3.5 and 3.6, with the results shown in Fig. 3.13 in the form of a van Deemter plot in the range of Pe = 4 to 400. All of the tested columns displayed h_{min} values between 1.5 and 1.8, and, with the exception of spherical particles, the reduced plate heights did not vary significantly after reaching their minima. These values compare favourably with those of conventionally (slurry) packed columns, which generally exhibit minimum reduced plate heights of h_{min} = 2.

Regardless of particle shape, the performances of the tested columns were superior to traditional columns containing fully porous random-packed particles. This result is consistent with computational studies that predicted the superiority of structured packing over random packing [26]. Inevitably, the experimental plate heights were marginally higher than the corresponding computational fluid dynamics (CFD) values because of wall effects and surface roughness. For example, a simple cubic packing of spheres has a predicted value of h_{min} = 1.0 by in Schure et.al, compared with h_{min} = 1.65, observed in our experiments.

Spherical elements did not produce the lowest plate heights but, rather, tetrahedral particles seemed to consistently outperform spheres across the entire range of Pe values tested, while other particle shapes often performed better than spheres. Therefore, while spherical particles are the most prevalent element shape used in packed bed chromatography[135,141] and may result in the most homogenous randomly packed beads, the results here indicate that other

shapes may be superior when the orientation and alignment of the elements can be perfectly controlled, as for example through 3D printing. Further investigation is required to confirm this observation and to identify geometrical features that would produce a configuration with the lowest possible plate height.

Several 2D and 3D computational studies on particle shape recommended the use of axially elongated particles[29,30,139]. Li et al. [139] showed that in a simple cubic arrangement, such particle shapes significantly outperform regular spherical particles. The proposed reason for this difference was the reduction of dead-zone volumes. The element shapes studied in our comparison were not explicitly chosen to verify this particular hypothesis but spheres, octahedra and triangular bipyramids are symmetrical elements with respectively increasing axial elongation. It can therefore be expected that triangular bipyramids and spheres would have the lowest and highest reduced plate heights, respectively. The experimental data however, showed no such relation between axial elongation and minimum plate height, possibly because the stagnation zones surrounding the overlapping spheres used in our work would have been considerably smaller than those surrounding non-overlapping spheres.

A consistent feature of the *h*–*Pe* curves of columns produced using 3D printing was the absence of a C-term contribution at the higher reduced velocities. Because the elements were non-porous, stationary phase mass transfer contributions would be negligible [142,143] but significant C-term gradients are normally observed in studies of ordered geometries, particularly the simple cubic configuration, even for non-porous beads. All elements exhibited reduced plate heights of $1.5 < h < 2.5$ even at the maximum tested reduced velocity of $Pe = 400$. For -shell or fully porous versions of the tested geometries, the mass transfer effects would likely be significant and a substantial increase in plate height would be expected when *Pe* exceeds that at the minimum plate height [144]. For non-porous elements however, the lack of a C-term gradient theoretically enables increased productivity and shorter analysis time.

The performance of the different element shapes was also not strongly related to the two *a-priori* geometrical parameters, namely the Wadell sphericity and specific surface area. As was the case with De Smet's 2D computational studies [29,30], the tested porosity of $\varepsilon = 0.36$ may be too low to fully reveal the differences between the tested element shapes. Because $\varepsilon = 0.36$ is a typical porosity value for conventional packed bed columns, this implies that the

two listed parameters do not play as large a role in determining column performance as the porosity and configuration of the geometry.

Larger differences between element shapes may be observed when arranged to produce more tortuous flow paths. While a simple cubic arrangement was the most convenient for producing connected networks of elements across a wide range of geometries, it inevitably limited the scope of the comparison to low tortuosity geometries. Further tests with other combinations of element shapes and arrangements would be necessary to find an optimal element packing geometry. The results of Sections 3.3 and 3.4 were published in Chemical Engineering Science[145].

3.5 Conclusions

In this chapter, several aspects of a packed bed geometry were studied in isolation in ways that were not possible without 3D-printing. The frit assembly arrangement tested here was found to significantly lower overall dispersion and minimize extra-column band-broadening compared to the single piece columns described in Chapter 2. Minimum plate heights of well under 2 (i.e. lower than typical random packed columns) could be achieved using this setup.

For the first time, the dispersion effects of various sphere packing arrangements were directly compared experimentally. The experiments confirmed what had been previously studied computationally: i.e. that the minimum plate heights of the FCC arrangement were the lowest, followed by the BCC and then the SC arrangement.

A comparison of element shapes in an ordered arrangement showed that tetrahedral elements produced the least dispersion. This was contrary to what is seen in regular packed bed columns, where spherical elements are preferred. However, no correlation between plate heights and geometrical characteristics could be established with the compared element shapes. Another conventionally held rule of thumb that densely packed beds produce the sharpest bands do not seem to apply to 3D printed ordered beds.

The work presented in this chapter has only covered a small fraction of the possible combinations of porosities, particle alignments and shapes that can be tested to better understand packed bed geometries. For ordered bed geometries, other combinations of element shapes and arrangements can be tested to discover novel, more effective geometries. For random packed geometries, variations within random packing can be studied once

challenges in design software have been overcome. The emergence of 3D-printing as an enabling technology means that dispersion effects of such properties can be systematically tested.

4. Investigation of Line Defects in Ordered Packings

4.1 Introduction

Due to the semi-random nature of the slurry packing process [146,147] and of the tendency of packing heterogeneities to self-aggregate and morph during fluid flow[148,149], the study of column packings with structural defects is an important part of understanding the flow properties of chromatography columns and of porous media in general. Structural defects in porous media can be characterized as either one-dimensional line defects with a narrow cylindrical void, planar defects and cluster defects where the void is typically spherical in shape[150,151]. CFD studies where the effects of line and cluster defects were investigated by Schure et.al.[152] show that eliminating structural defects in the column packing is significantly more important to column plate heights than decreasing extra-particle porosity. Whereas the CFD studies were conducted with periodic boundary conditions which neglected column wall effects, experimental studies on porous media with deliberately introduced and carefully quantified defects have not been possible to conduct.

A key feature of 3D printed chromatography media is the ability to design and print non-ideal porous structures involving either general packing heterogeneity across a column or introducing a localized defect into the packing structure. This study aimed to investigate the effects of well-defined line defects in columns containing ordered packings in a range of particle shapes as well as defect shapes. The effects of the structural defects were isolated by a comparison of a defect-free control column. Both residence time distribution studies and CFD simulations were performed on the defect geometries. To our knowledge, is the first study that investigates identical micro-structures using both CFD and experimental methods in the field of chromatography.

4.2 Materials and Methods

A series of columns with packing volumes of 5 ml were built to test the effects of line defects. The columns, cylindrical in shape contained spherical beads with a diameter of 600 μm and an overlap factor of $\alpha = 1.10$, arranged in a simple cubic configuration. The internal diameter and wall thicknesses of the columns were 12 and 2 mm, respectively, with an extra-particle porosity

of ϵ = 0.370 being maintained for all columns. A portion of the packing was removed from each layer of the structure so that the line defect was parallel to the axis of the cylindrical column. The magnitude of the line defects was quantified using a porosity difference, PD which is defined as follows:

$$PD = \frac{\varepsilon_{DM} - \varepsilon_{ND}}{\varepsilon_{ND}} \quad \textbf{Eq 4.1}$$

where ϵ_{DM} is the porosity of the defected model and ϵ_{ND} is the porosity of the non-defected version of the packing. For columns with spherical beads, four different defect shapes, shown in Fig. 4.1 were designed and printed.

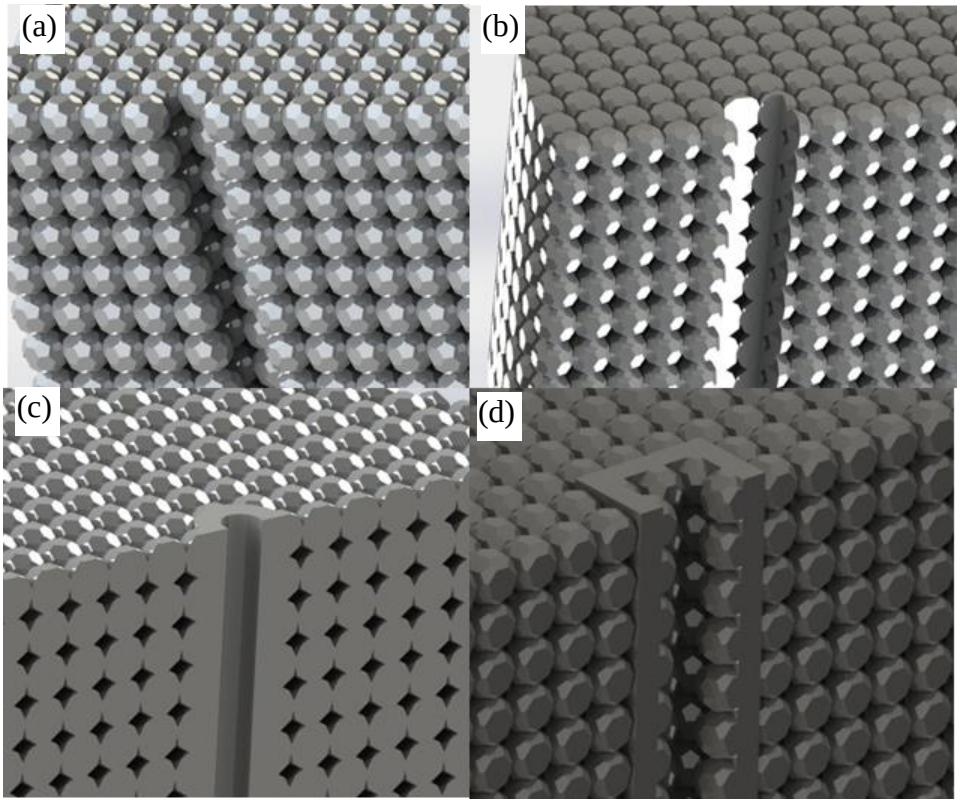

Figure 4.1: Line defects: (a) Discrete bead removal (DBR) and (b) Square cross section defect (SCS), (c) Tube defect (TD), (d) Embedded tube defect (ET)

Discrete beads were removed (DBR) from each layer of the simple cubic packing (Fig. 4.1a). Columns with 1-5 removed beads. In the case of more than one bead being removed from each layer of the packing, the beads neighboring the original singe-bead line defect were removed, meaning that the closest approximation to a circular cross section was maintained for the line defects across all the PD values. Additionally, a line defect with a square cross section was designed whereby portions of beads were removed to create a square void through the packing

(Fig. 4.1b). Both defect shapes allow for lateral exchange ("seepage") between the defect channel and the porous bed.

The channel and packing were partitioned by a 200 μm internal wall in the case of the tube defect column (TD) that was cylindrical in shape. Another walled defect, the embedded tube defect contains partial beads protruding from the square cross sectioned walls, as shown in Fig. 1d. The extent of radial dispersion within the packing itself and between the defect and the packing can be quantified using these four line defect models. For all the defect shapes, columns with porosity differences of PD = 0.195, 0.392, 0.587, 0.783 and 0.977% were created, corresponding to 1-5 missing beads in the DBR models.

To study the effects of particle shape on the column flow properties, columns filled with elements described in Chapter 3.3 were designed. An extra-particle porosity of $\epsilon = 0.370$ was maintained by adjusting the overlap factor between the beads. For each particle shape, a single bead was removed from each layer of the packing corresponding to an approximate porosity difference of PD = 0.195%. Additionally, a tube defect model with the same PD value was created for every particle shape. The particles were characterized by their Wadell sphericities ψ:

$$\Psi = \frac{\pi^{\frac{1}{3}}(6V_P)^{\frac{2}{3}}}{A_P} \qquad \textbf{Eq 4.2}$$

where V_p and A_p represent the volume and the surface area of a particle, respectively. It is worth mentioning that because the particles overlapped, the volume and area of the particles in their truncated form were used to measure their sphericities, often resulting in sphericities of $\psi > 1$ which would be geometrically impossible with a packing consisting of discrete beads.

The RTD studies to test the defected columns were identical to the previous studies except for being conducted at a superficial velocity of u = 26.5 cm.hr^{-1}, which corresponded to v_{min} for a simple cubic arrangement. The mean residence times, and consequently the tracer velocities were measured using the moment method outlined in the proof of concept tests. CFD studies of a unit section of each of the packing arrangements were conducted along with a unit section of each of the defect shapes at an interstitial velocity corresponding to the superficial velocity of u = 26.5 cm.hr^{-1}. The pressure drops per unit length for each of the geometries was measured. The simulations were performed on on COMSOL Multiphysics 4.2a using a time-independent

solver, laminar flow conditions and with the fluid density and viscosity corresponding to those of pure water at 18 ^{o}C[153].

A default tetrahedral meshing scheme with an average element size of 4.6 μm was used for the flow region. Grid independence for all the models was establishing by halving the element sizes and measuring the maximum velocity on the outlet surface. For all geometries, halving the element size only resulted in a change in maximum velocity of < 0.5%. The domain of study was limited to just a unit cell of the packing and of the defect as a simulation of a full column would require an impractical computation time. Based on an investigation of hard sphere packings performed in COMSOL 4.2 a by Stute et al. on a BiCGStab supercomputing platform[154], we can estimate that a simulation of a full column printed for this study would require approximately 1.5×10^{6} h using the grid resolution and iterative solvers used in the CFD models. The methodology used in this investigation does not allow for a direct comparison with the experimental results as no RTD curves were produced. Instead, the pressure drops across the unit cells were measured to calculate the relative tracer velocities through the defect channels and porous beds.

4.3 Results and Discussion

The RTD profile of a column with a line defect is characterized by a dual peak (shown in Fig. 4.2) with the initial breakthrough curve caused by the defected channel. The E-curves of the defected columns were decomposed into two separate curves with two distinct mean residence times, variances and peak asymmetries for the line defect and the porous bed.

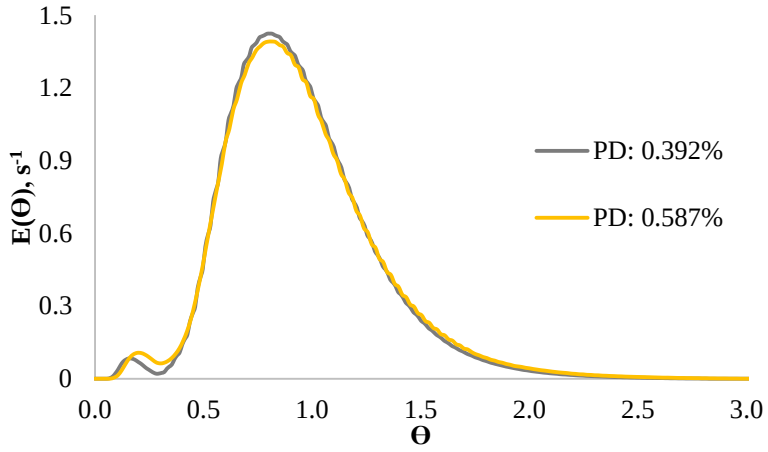

Figure 4.2: Normalized E-Curves of residence time distribution tests performed on DBR defect columns with spherical beads

Dual-peak profiles for all the tracer tests were observed, with the higher PD values resulting in larger breakthrough curves. For the minimum and maximum values of PD = 0.195% and 0.977%, the breakthrough peak accounted for 3.5% and 10.9% of the total peak area respectively. This trend of larger areas for breakthrough curves for higher PD values was consistent for all tested columns, with correspondingly smaller and more asymmetrical main peaks. Theoretical predictions on the relative velocities were made using a two-compartment model based on the Carman-Kozeny and Hagen-Poiseuille equations describing the porous bed and the line defect channels respectively. The relative channel velocity, v_c/v_b can be described as follows:

$$\frac{v_c}{v_b} = \frac{180}{32} \frac{D_c^2}{\Psi^2 D_p^2} \frac{(1-\varepsilon)^2}{\varepsilon^3} \qquad \textbf{Eq 4.3}$$

with ϵ, Ψ, D_c and D_p representing the extra-particle bed porosity, particle sphericity, defect channel and particle diameters respectively. In the case of non-spherical particles, the diameter of an equivalent volume sphere was used for D_p. In all calculations, the bed velocity v_b refers to the superficial velocity across the porous bed. This model assumes a straight, cylindrical tube through a porous bed comprised of randomly placed hard packed spheres. It does not account for any potential seepage between the porous bed and the line defects. Of all the printed models, the tube defect model in a packing of truncated icosahedra (shown in Fig. 4.1c) was the nearest representation of the two-compartment model with the only key difference being that the printed model contained an ordered arrangement of spheres as opposed to the random packing assumed by the Carman-Kozeny equation.

Deviations from this model indicated the direction as well as the extent of seepage between the two compartments as well as differences in pressure drop between a simple cubic arrangement (used in all printed columns) and a random close packing. The model does account for non-spherical particles but not their configuration. The tested models with non-spherical particle shapes can provide insights into the variations caused by a packing arrangement that is not easily manufactured without 3D printing.

The differences between plate heights H of the defected columns and their corresponding defect-free control columns were then calculated to produce the relative loss in column

performance ΔH. The relative channel velocities and performance losses for the columns containing trunctaced icosahedral beads are shown in Fig. 4.3.

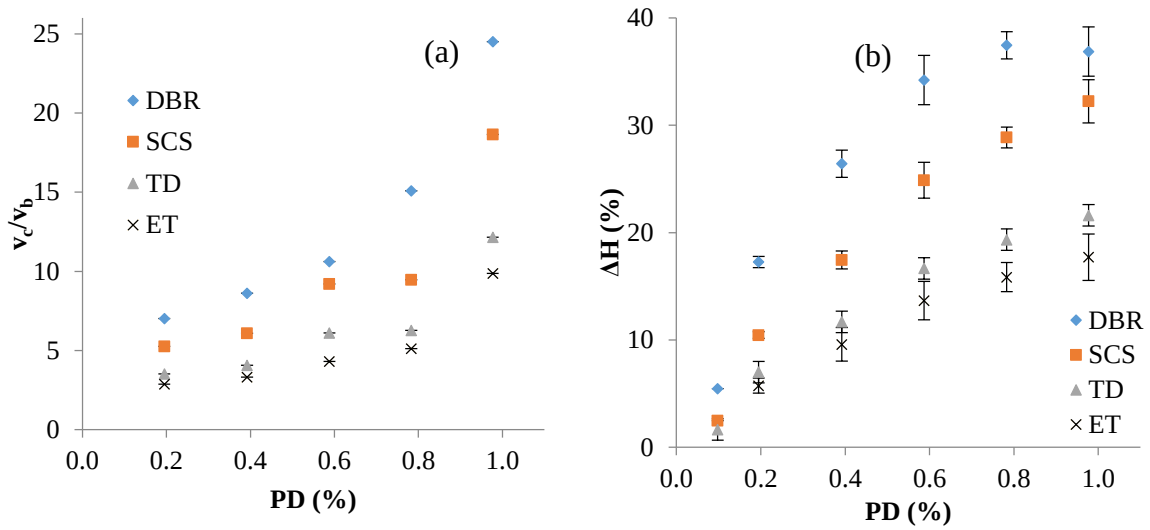

Figure 4.3: (a) Relative channel velocity v_c/v_b(b) column performance loss vs defect size for columns containing spherical beads with discrete bead removal (DBR), square cross section (SCS), tube defect (TD) and embedded tube (ET) line defects

Across the various defect types, the calculated relative channel superficial velocities are significantly lower than the velocities predicted by the two-compartment model. In the case of the tube defect model, the closest replication of the theoretical model, it was approximately one order of magnitude lower across the tested defect sizes. The assumptions made by the two-compartment model largely involve the Carman-Kozeny component. The lower relative channel velocities can be accounted for by the lower fluid tortuosities produced by the simple cubic configuration. Additionally, it is worth noting that the particle sphericity used for the calculations was $\psi = 1.39$ due to the overlap in the truncated icosahedra, rather than a value of $\psi = 0.98$ if the packing was comprised of discrete particles.

Both the tube defect and embedded tube models contained the internal walls between the porous beds and line defects, therefore the differences between the two models were solely due to the non-cylindrical walls and the additional pressure drop caused by the protruding beads. The higher relative channel velocities of the DBR and SCS models (the two models that allow for seepage between the two compartments) shows the extent of seepage from the porous bed and the line defect with the differences between the two models being caused by the different channel porosities (the area available for the fluid to transfer from the porous bed into the channel). The seepage between the defect and the porous bed accounted for 40-60% of the

increase in plate height, as the difference between porous (DBR and SCS) and closed (TD and ET) defect shapes showed.

In the case of column performance loss, an asymptotic relation was observed between defect size and ΔH with the asymptotes for each defect shape correlating with the relative channel velocities. In the tested PD range (i.e. maximum of PD = 1%), a maximum asymptotic increase of 40% was observed in the plate heights of the printed columns. At a first glance, a performance loss of 40% may not seem significant compared to breakthrough effects caused by other reasons such as solvent incompatibility[155] or viscous fingering[156,157]. A 40% decrease in the number of plates only results in an 18% decrease in peak capacity. In preparative chromatography, the yield for a certain percentage recovery is a function of Log[N], where N is the plate number[158].

However, the tracer profiles shown in Fig. 4.2 can render a column unusable in practice. In analytical separations, the appearance of small false peaks could mean that the column cannot be used for the analysis of a sample. The breakthrough curves shown in this chapter all involve pulse injections with an unretained tracer. This means that the breakthrough curves typically arrive well before the main peak. However, a mixture of analytes with different retention factors passing through a column with a line defect would effectively produce two overlapping chromatograms: one regular chromatogram and a breakthrough chromatogram. Breakthrough peaks with high retention factors could appear after the first compound on the regular chromatogram. In such cases, the effects of a line defects are far worse than the 40% increase in plate height might indicate.

In purification processes, the yield is reduced as the compound of interest is lost in the breakthrough peak. Furthermore, breakthrough curves of impurities with higher retention factors could also merge into the compound of interest. Here too, the consequences of a line defect are worse than their plate height numbers may indicate.

To determine the effects of particle shapes on the column flow properties, the relative velocities of the four particle shapes (shown in Fig. 4.4) were calculated. Additionally, CFD simulations of 8 different particle sphericities were performed and the relative velocities calculated assuming a two-compartment model. As the particles become less spherical, higher pressure drops are caused by the more tortuous fluid flow paths within the porous bed, and consequently produce lower relative channel velocities.

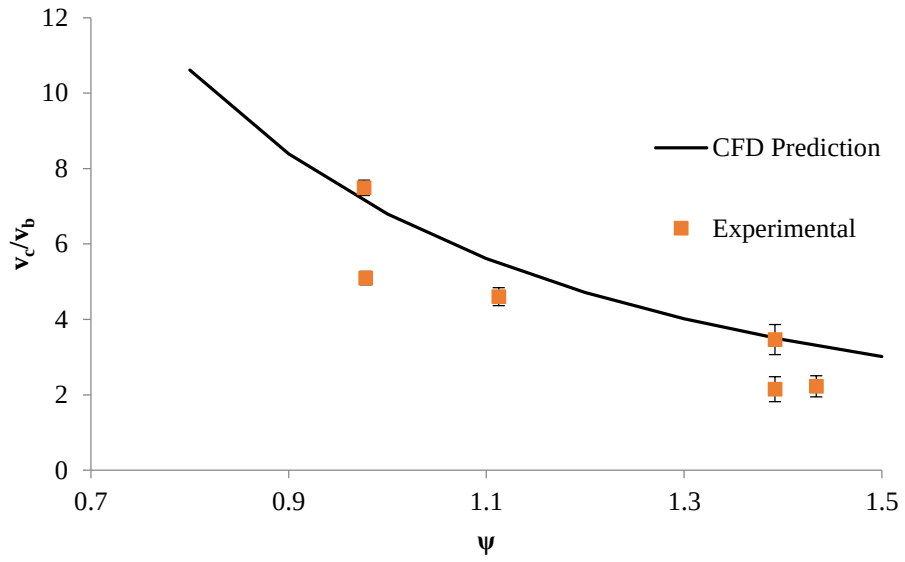

Figure 4.4: Relative channel and bed velocities with the tested particle shapes

General agreement was seen between the CFD and the experimental velocities despite internal variations in velocities between particles with nearly identical particle sphericities. For example, both tetrahedral and stella octangula, two evidently different shapes are calculated as having sphericities of $\psi = 0.98$ in their truncated forms but have large differences in their design specific surface areas that may account for the differences in relative channel velocities.

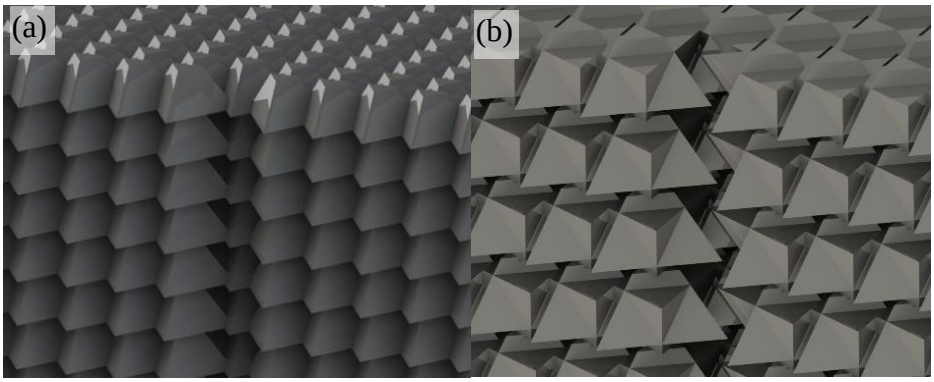

Figure 4.5: DBR defects in columns containing (a) tetrahedra and (b) stella octuangula

In addition to the particle shape, the relative channel velocity v_c/v_b, is also a function of the shape of the resultant channel. As seen in Fig. 4.5, the channels created by a DBR defect vary in tortuosity and in accessibility to the porous bed (channel porosity). For example, CFD simulations of the two defects shown above indicated channel tortuosities of $\tau = 1.06$ and $\tau = 1.24$ in channels created in the tetrahedral and stella octangula columns, respectively. In the case of particles shown in Fig. 4.5, the defects themselves are not clearly visible, due to the high particle overlaps necessary to create strong, monolithic structures.

With the dual-peak RTD profiles that the defected columns produce, it is possible to investigate the properties of the two curves in isolation, revealing the flow properties of the porous bed and the line defect channel separately. While the two mean residence volumes determine the channel and bed velocities, both the variance and peak asymmetry of the two profiles can indicate the extent of radial dispersion as well as residence time inhomogeneity that two geometries produce.

In the case of discrete bead defects seen in Fig. 4.5, peak asymmetry of the initial breakthrough curve Υ_1 can be caused by caused by wall 'roughness' i.e. deviation from Hagen-Poiseuillie flow in non-cylindrical channels. This deviation from a cylindrical channel shape can be quantified in a metric analogous to Wadell sphericity. An additional contribution is the seepage of tracer flow from the packing into or out of the defect channel. Radial dispersion within the porous bed as well as interfacial area (which was quantified in terms of the design channel porosity ϵ_C) between the two compartments would contribute to Υ_1. Table 4.1 shows the three design metrics as well as the experimental peak asymmetry of the breakthrough curve Υ_1 for each tested particle shape in the discrete bead defect columns.

Table 4.1: Peak asymmetry Υ_1 as a function of particle and channel shape in DBR columns

Particle Shape	**Sphericity, ψ**	**Channel Porosity, ϵ_C**	**Υ_1, ±0.03**
Tetrahedron	0.98	0.33	1.41
Stella Octangula	0.98	0.43	1.69
Dual Tetrahedron	1.11	0.33	1.21
Truncated Icosahedron	1.39	0.28	1.27
Octahedron	1.43	0.61	1.96

When both of the above factors are negated, as in the case of TD columns with cylindrical walls, the peak asymmetries were consistently lower with an average breakthrough asymmetry of $\Upsilon_1 = 0.62 \pm 0.04$ across the TD columns with all the tested particle shapes. The causes for this baseline asymmetry can include extra-column backmixing in the distributors and roughness on the surface of the cylindrical channel.

Positive values of peak skewness suggest that there was seepage into and not out of the defect flow channel. More importantly, the data suggests that the design particle sphericity ψ is a poor

predictor of breakthrough asymmetry Υ_1 (R^2 = 0.060). Channel porosity, a more rudimentary parameter that is only indirectly related to the particle shape predicted breakthrough asymmetry (R^2 = 0.905) more accurately. The linear relation between the two parameters indicates that the extent of radial dispersion is similar across the tested packings and is almost entirely unrelated to the particle shape. It is also worth noting that the range of sphericities tested in this CFD study is significantly higher than those tried in experimental studies.

Peak asymmetry of the packing Υ_2 is predominantly an indicator of the defect-free performance of the packing geometry, quality of inlet distribution and backmixing caused by the extra-column void spaces. As the fluid distributors and collectors for all the printed columns were identical in design, variations in extra-column backmixing can be neglected. In addition to the sphericity ψ and specific surface area S_P, the Υ_2 values for each particle shape is listed in Table 4.2.

Table 4.2: Packed bed asymmetry Υ_2 in relation to design sphericity ψ and design specific surface area of the internal packing S_P

Particle Shape	**ψ**	**S_P, mm^{-1}**	**Υ_2, ±0.02**
Tetrahedron	0.98	24.7	0.52
Stella Octangula	0.98	15.0	0.77
Dual Tetrahedron	1.11	17.9	0.41
Truncated Icosahedron	1.39	13.0	1.18
Octahedron	1.43	18.6	0.62

Significant differences in asymmetry were observed with changing particle shapes. Columns with non-spherical beads consistently produce more symmetrical curves than the two spherical models (with DBR and SCS defects) with the least spherical particle shape, the tetrahedra producing the most symmetrical curves which might be accounted to the greater specific surface area of non-spherical particles.

Except for the case of dual tetrahedral particles, an elementary metric like specific surface area is a more reliable indicator of the column performance than particle sphericity. However, not

all of the packing's internal surface is readily accessible to the fluid meaning that making the particles more non-spherical particles does not necessarily translate into more symmetrical curves and better column performance. These findings are directly contrary to a numerical study[159] and experimental studies[160,161], where bed permeability expressed in the form of bed velocity in this case, was clearly influenced by particle sphericity.

The non-dependence on particle sphericity seen in Table 4.1 and Table 4.2 as well as the discrepancy between these experimental results and the results found in literature could also be caused by the uniform packing arrangement used in all printed columns. In a random close packing of beads, the particle sphericity inevitably influences the arrangement of particles during the packing process and more importantly, the size, shape and alignment of the resultant pores as well as the available surface area. This means that in a traditional packed bed, ψ is not merely a geometrical parameter that describes a unit component of the solid phase but an indicator of the size, shape and inter-connectedness of the pores within a packed bed. When a standardized particle size and arrangement is used, isolating sphericity from other aspects of the porous bed's microstructure, ψ ceases to be a good predictor of the flow properties of a packed bed. Limitations of the metric have been discussed before in experimental analysis of bed permeability data and an additional shape factor is recommended to describe the particle shape with the exact definitions of the shape factor varying for each study.

To better understand the differences between the flow properties of different particles shapes and configurations, it is worth considering the derivations of the fundamental equation used to predict the relative velocities. In the case of Carman-Kozeny equation, it is assumed that the porous structure is a set of parallel capillaries that are cylindrical in shape. A multiplication factor of $\lambda = 2.5$ is then experimentally determined to predict pressure drop across a random packed bed of spheres. λ accounts for the tortuosity of the flowpaths as well as varying diameters of the 'capillaries'. To determine the empirical constant λ for the various particle shapes in their tested configurations, tube defect columns were prepared for several particle shapes. Using a smooth cylindrical tube, the channel roughness effects caused by different particle shapes are removed and only the Carman-Kozeny portion of the two-compartment model is optimized for the particle shapes and packing arrangements. λ, experimentally determined using the channel and superficial bed velocities is calculated as follows:

$$\lambda = \frac{32}{72}\frac{v_c}{v_b}\frac{\Psi^2 D_p^{\,2}}{D_c}\frac{(1-\varepsilon)^2}{\varepsilon^3} \qquad \textbf{Eq 4.4}$$

Table 4.3: Multiplication factor λ for tested particle shapes

Particle Shape	λ	
	Experimental (±0.06)	CFD
Truncated Icosahedron	1.20	1.41
Tetrahedron	0.87	0.92
Dual Tetrahedron	1.02	1.29
Stella Octangula	1.28	1.28
Octahedron	0.82	0.78

Table 4.3 shows the computationally and experimentally determined values for all particle shapes. For all shapes, the λ values are significantly lower than for random packed columns, with computational and experimental results in good agreement. A possible reason is the parallel alignment of through-pores and low tortuosity in the simple cubic geometry. The close agreement points towards accurate replication of the CAD models in the printed columns. The discrepancy from random packed columns is especially large in non-spherical shapes such as terahedra and octahedral elements. It is worth noting that, particularly with non-spherical particles, the packing arrangements found in porous media are significantly different from the printed columns that contain a simple cubic configuration, involving the vertices of the polygons connected with their neighboring particles. In the case of traditional packed beds, each particle shape would result in a unique particle arrangement with the random placement of beads reducing the differences in pore shape, size and alignment caused by varying particle shape.

4.4 Conclusions

A range of models containing several defect and bed geometries were designed and printed to investigate the effects of line defects on band broadening. The data produced in RTD experiments have shown that flow contributions to the defected channel are significantly lower than predictions made by the two-compartment model with the determining factors being the channel shape and channel porosity (to allow for fluid transfer from the porous bed into the line defect). Particle shape was shown to have a significant effect on flow through the porous bed and its resultant defects in both experimental and CFD studies. However, relative

channel velocity and peak asymmetries of both curves produced in the dual peak RTD profiles were not correlated to the Wadell particle sphericity, with rudimentary metrics such as specific surface area and channel porosity proving to be better predictors and by extension, more accurate representation of the geometry of the printed monolithic structures.

Comparisons of closed (TD and ET) and porous (DBR and SCS) line defects showed that roughly half of the increase in plate height was a result of radial seepage from the porous bed to the line defect channel. In terms of permeability, both the experimental and CFD results show that the simple cubic geometry used for all models is a closer representation of the parallel capillary model as shown by the consistently lower λ values.

The studies described in this chapter demonstrate the capabilities of 3D-printing as a tool to examine principles behind flow through porous media. The control over the geometries (in this case, the defect and particle shapes) provides the opportunity to reproducibly test otherwise uncontrolled phenomenon such as line defects within chromatography columns.

5. Triply Periodic Minimal Surfaces as Stationary Phase Microstructures

5.1. Introduction

Previous chapters have described the capabilities of 3D-printing as a method to build a wide range of ordered lattices of overlapping particles. Chapter 3 describes the superior performance of several non-spherical particles in ordered packings [162]. Although the tested geometries were all repeating unit-cells of 'particle' packings, the void spaces left between the solid elements typically contain large variations in the local pore sizes and surface areas within a unit-cell of a of particle-like element. For example, even the most ordered sphere packing structure, the face-centered cubic arrangement, contains void zones that vary by up to 70% in their local hydraulic diameters. The mobile phase channels of such ordered packings are not homogenous and ordered mobile phases.

A better approach may be to build monolithic networks in which both stationary and mobile phase geometries are rationally designed. A promising class of such structures is offered by minimal surfaces, which are defined as locally minimal energy area surfaces with a mean curvature of zero. They were described by Meusnier in 1776 and the most commonplace examples are those of soap films [163]. Minimal surfaces that contain a crystalline structure are of special interest because they repeat themselves in three dimensions. Such surfaces divide a volume into two uniform, interconnected but non-intersecting labyrinths and are known as triply periodic minimal surfaces (TPMSs). They were first identified by mathematicians H.A. Schwartz and E. R. Neovius, describing surfaces that would later be known as the Schwartz Primitive, Diamond and Hexagonal [164–166]. Many minimal surfaces have since been discovered and studied, with the most significant development being the description by Schoen of the gyroid and I-WP TPMS forms [167].

TPMS structures occur naturally between phases in cell membranes[168,169], block copolymers and photonic crystals [170–172], such as those observed in butterfly wing scales [173–175]. Computational studies have shown that minimal surfaces exhibit favourable mechanical properties[176], permeability [177] and are extremal in cases where high and low relative thermal or electrical conductivities are desired in two separate but intimately mixed phases [178,179]. The novel concept described in this chapter is that chromatographic applications, the volume on

one side of the TPMS could comprise the stationary phase and the other the mobile phase, facilitating the rational design of both phases. Their well-defined mathematical definitions facilitate myriad variations of the basic forms of each TPMS, for example to alter the relative volumes divided by the surface (thus, in our case, the relative dimensions and volume fractions of the stationary and mobile phases, or column porosity) or to vary the flow profiles across the x, y or the z direction.

Additive manufacturing enables accurate physical production of TPMS-based structures over wide range of length scales, meaning that virtually any defined minimal surface can now be designed, produced and tested. There have been several studies involving 3D-printed TPMS models testing their mechanical properties [180–182]. Their high permeabilities and structural stiffness offer advantages as porous scaffold macrostructures of 3D-printed implants [183,184]. The heat exchange properties between two labyrinths, separated by a TPMS wall have been used to create membrane-like heat exchangers [185,186].

The above studies indicate that TPMS-based structures offer highly versatile, tunable surface morphologies and geometrical characteristics that can affect stationary-phase volume fraction (adsorption capacity), velocity profiles (dispersion) and permeability (back-pressure). In this study, a combination of computational fluid dynamics (CFD) and experimental studies using 3D-printed porous beds were used to compare the chromatographic performance of several TPMS-based structures, showing that porous bed performance can now tuned. The computational tests were performed by Fabian Dolamore using the Lattice Boltzmann Method (LBM), with the setup described in another study [187,188].

5.2 Methods

5.2.1 Porous Bed Design

To create robust 3D structures, TPMS-based geometries were created in which one side of the TPMS served as the mobile phase and the other as the stationary phase. The 3D-printed parts therefore comprised single monolithic networks with repeating unit-cells.

Numerous varieties of TPMS can be created, depending on the cubic crystal structure. This study focuses on the four best-known TPMS geometries: the Schwartz Primitive (Fig. 5.1a), based on a simple cubic crystal structure, the Schoen IWP (Fig. 5.1b), based on a body-centred cubic crystal structure, the Schoen Gyroid (Fig. 5.1c), with a body-centered cubic

structure and the Schwartz Diamond (Fig. 5.1d), arising from a diamond cubic crystal structure, a sub-set of face-centered cubic arrangements. Other than the Schoen IWP, these surfaces are generally known as the P-G-D family of minimal surfaces, and are the topologically simplest examples of TPMS that possess cubic lattice symmetry. The members of the P-G-D family balanced minimal surfaces: i.e. the two separate labyrinths (stationary and mobile phases in our case) are congruent and have identical geometrical properties, whereas the IWP is unbalanced.

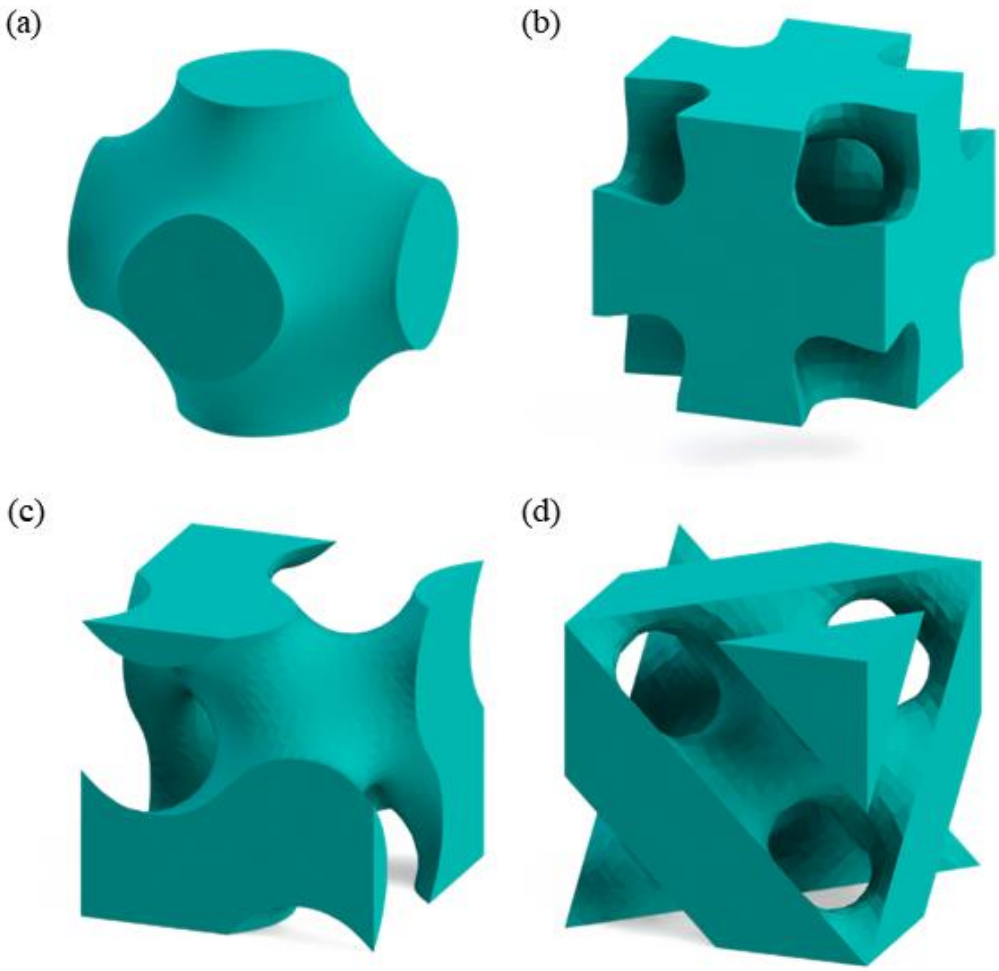

Figure 5.1: CAD images of unit-cells of the tested triply periodic minimal surface structures (a) Schwartz primitive (SP), (b) Schoen iwp (IWP), (c) Schoen gyroid (SG) and (d) Schwartz diamond (SD)

(a) $cos(x) + cos(y) + cos(z) < t$,

(b) $2\,[cos(x)\,cos(y) + cos(z)\,cos(x) + cos(y)\,cos(z)] - [cos(2x) + cos(2y) + cos(2z)] < t$,

(c) $sin(x)\,cos(y) + sin(y)\,cos(z) + sin(z)\,cos(x) < t$,

(d) $sin(x)\,sin(y)\,sin(z) + sin(x)\,cos(y)\,cos(z) + cos(x)\,sin(y)\,cos(z) + cos(x)\,cos(y)\,sin(z) < t$

Eq 5.1

The above trigonometric approximations of the TPMS structures were used for this study. These approximations were developed by von Schering and Nesper[189,190] and are known to be accurate representations of the final geometriesto define the Schwartz Primitive, Schoen IWP, Schoen Gyroid and Schwartz Diamond, respectively, where values of t lower than 0 comprised the stationary phase and values greater than zero comprised the mobile phase. the geometries were designed to be balanced across the stationary and mobile phases ($t = 0$) and consequently, superficial column porosity $\varepsilon = 0.50$.

Table 5.1: Geometric characteristics of tested TPMS structures at $t = 0$. The specific surface area S is non-dimensionalized with respect to the length of the unit-cell.

	Specific Surface Area, S	**Tortuosity, τ**
Schwartz Primitive	2.35	1.03
Schoen IWP	3.58	1.12
Schoen Gyroid	3.09	1.26
Schwartz Diamond	3.85	1.29

The tortuosity of the model is calculated using Lattice-Boltzmann simulations by dividing the sum of axial velocities and absolute total velocities in the simulated domain. This was the method used to calculate tortuosity in an earlier computational study by Dolamore *et al.*[187] As shown in Table 5.1, the Gyroid and Diamond geometries showed significantly higher tortuosities than the Primitive or IWP models.

For the IWP model, it is worth noting that the tortuosity only pertains to the geometry where $t < 0$. For the structure where $t > 0$, the tortuosity is $\tau = 1.03$. For the other three structures, the tortuosity is identical for structures defined by positive and negative values of t. As a comparison, this is compared to the best sphere packing from a previous study [162] on particle packings.

5.2.2 3D-Printing and Post-Processing

Computer aided design (CAD) models of the four TPMS geometries were created using Wolfram Mathematica 7.0 (Wolfram Research, Champaign, Illinois) and SolidWorks 2012 (Dassault Systemes, Vélizy-Villacoublay, France) using the parametric equations described in Eq. 5.1 To create a surface tessellation language (.stl) file that could be 3D-printed, discretized versions of the structures described by the parametric equations were created,

with each unit cell surface split into approximately 400 adjoining triangles. The method for designing the TPMS columns shown here are described in Appendix 2.

The unit cells for each printed geometry were 1 mm across, corresponding to channel dimensions of the order 500 μm. The surface areas of the geometries are therefore *S* values presented in Table 5.1 multiplied by 1 mm^{-1}. Preliminary test prints showed that the structures could be 3D-printed with smaller unit-cell sizes but 1-mm dimensions were used to ensure printing fidelity and reproducibility of the CAD models. The column diameter and volume of each printed model were 18 mm and 10 ml, respectively. Wall effects were minimized by printing each column as a single piece, with the monolithic network embedded into the walls. As in the previous chapters, CAD models were printed on a UV-curing inkjet 3D-printer (3DS Projet HD 3500, 3D Systems, Rock Hill, SC) using the commercially available Visijet X ABS-like polymer.

5.2.3 Flow Characterization

Dispersion through the columns was calculated using the moment analysis method previously described [162], with 1 M NaCl tracer pulses injected and the conductivity of the eluent recorded. The basic schematic used in the ÄKTA 10 and 100 systems is shown in Fig. 5.2. To reduce extra-column band broadening, the column selection valve was bypassed and the column was connected directly to the injection valve. The 1 mm unit-cell lengths meant that it was not possible to measure B-term effects in the Van Deemter curves within practical time-scales. Reaching a reduced velocity of $\nu = 0.5$ would translate to an approximate elution time of 400 minutes. To fully capture tailing effects, this number would have to be tripled or quadrupled. Performing triplicate studies at flow rates on all tested geometries were therefore deemed impractical.

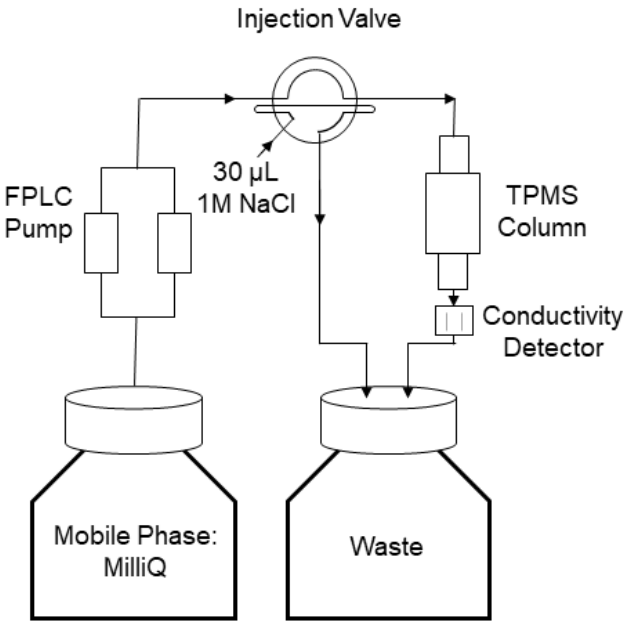

Figure 5.2: Schematic of pulse injection tests of TPMS columns with conductivity detection

The permeability, *k*, of the geometries was calculated from the pressure drop recorded over the range of tested velocities:

$$k = -\frac{u\mu\varepsilon L_D}{\Delta P}$$ **Eq 5.2**

where $\bar{u}$, μ, ε, L_D and ΔP represent the superficial velocity, dynamic viscosity, superficial column porosity, column length and pressure drop, respectively. The dimensionless term, flow resistance Φ, is calculated as follows:

$$\Phi = \frac{\varepsilon D_h^{\,2}}{k}$$ **Eq. 5.3**

In all cases, the results were non-dimensionalized with respect to the hydraulic diameter of the unit-cell

$$D_H = \int_0^Z \frac{4A_Z}{P_Z} dz$$ **Eq 5.4**

;where A_Z and P_Z are the cross-sectional areas and wetted perimeter lengths along each slice of the unit-cell in the z direction for the mobile phase.

5.3 Results and Discussion

5.3.1 Geometrical Analysis of Printed Samples

Confocal overlay images of the sample parts, shown in Fig. 5.3 show good replication of the CAD models. The structures are evidently recognizable as matching their intended TPMS structures. The experimental dispersion and pressure drop characteristics of the 3D-printed models can therefore be said to describe meaningful differences between flow properties of the tested geometries. Inevitably, a certain degree of discretization and surface roughness will be present in any 3D-printed structure. As the resolution of 3D-printers improve with time, these imperfections in the structures will be offer decreasing significance compared to the intended structures.

A recurring feature in the 3D-printed parts are parallel, vertical striations. In this case, the striations are 28 μm apart, corresponding to the nominal printer resolution. These are an inherent feature of extruder or foil-based 3D-printing methods where 3D structures are constructed as a series of 2D layers and each layer is constructed as a series of extruder lines. Other methods such as liquid based digital light processing or 2-photon polymerization will not necessarily exhibit a similar surface pattern, due to the different methods of constructing a 3D object[97]. Experience with inkjet systems has shown that to produce parts with the best print resolution, linear segments in the geometry must be aligned with these striations where possible. The Schwartz Diamond geometry was thus rotated by 45^{o} about the z-axis to align it with the extruder lines of the 3D-printer, in both the sample parts and full columns. As this rotation is about the axis of the column cylinder, it has no effects on its flow properties, but improves print quality.

The images shown in Fig. 5.3 resemble structures whose *t* values are 0.05 to 0.1 (i.e. lower porosity than described by CAD models), rather than 0 as described in the CAD designs. This is largely a result of the intensity overlay function of the confocal microscope, where only the maximum intensity projections are taken from each cross-sectional image and effectively, displays the sum of all over-printing errors.

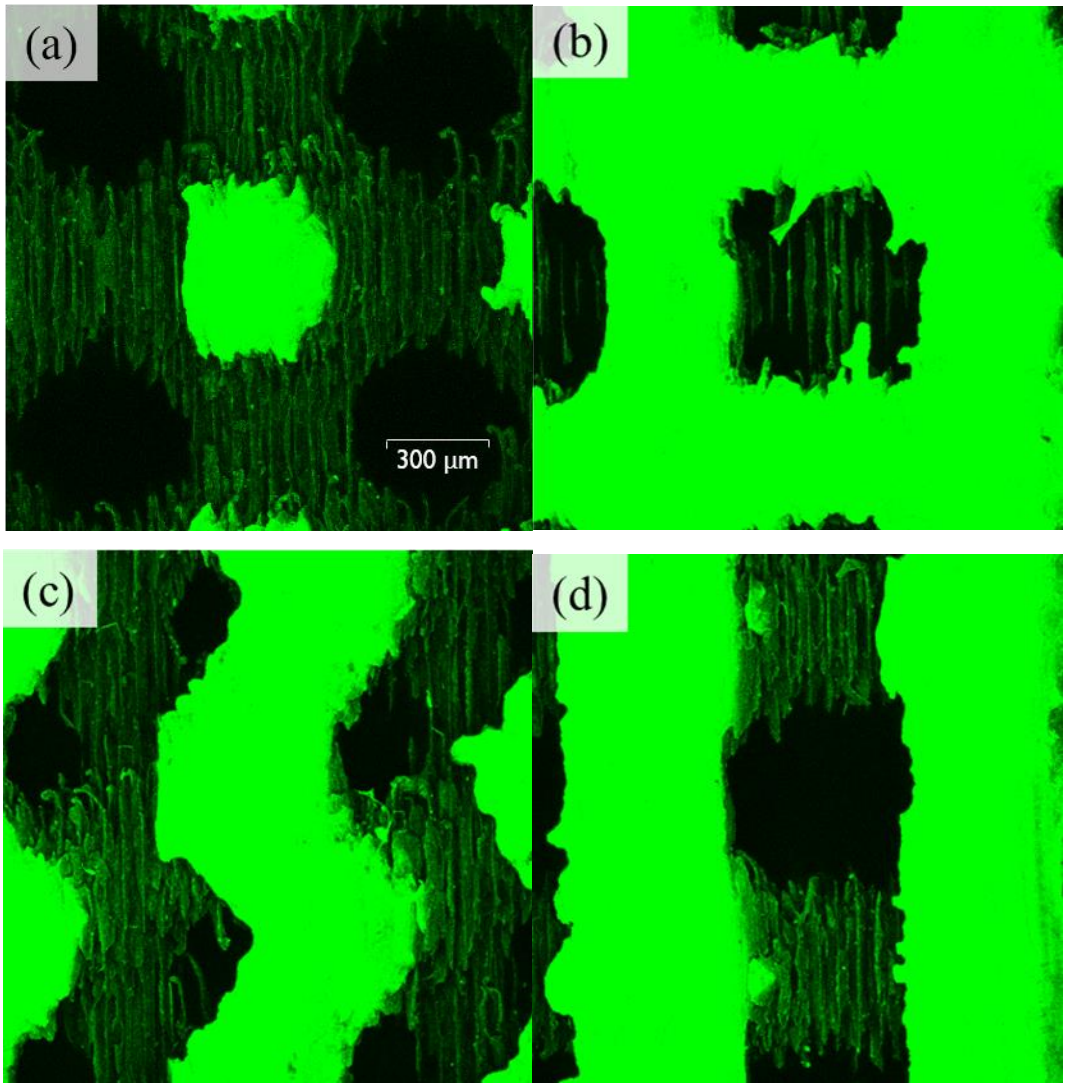

Figure 5.3: Maximum intensity overlay images of tested geometries (a) S Primitive (c) Gyroid (d) S Diamond and (e) Schoen IWP captured using a Leica TPS SP5 system and a HCX PL APO CS 10.0 × 0.40 dry UV objective. The S Diamond sample is rotated by 45º about the z-axis. The scale bar shown in (a) applies to all confocal images.

Just as the 3D structures of the TPMS can be reliably approximated by parametric equations, so too can any individual 2D cross-section of the structure. By setting the *z* value in Eq.5.1 to correspond to the slice depth of the individual confocal images, it is possible to compare any single image to a 2D parametric plot. The build errors were calculated on Wolfram Mathematica 8.0 by comparing binary versions of the microscope images and their corresponding parametric plots to determine non-overlapping regions. The build error e_b is defined as follows:

$$e_b = A_N / A_V \qquad \textbf{Eq 5.5}$$

where A_N is the non-overlapping area between a cross-sectional confocal image and its corresponding 2D parametric plot and A_V is the design surface area of the void zone in a cross-section. The build errors for the tested TPMS geometries as a function of slice depth, *z*

are presented in Fig. 5.4. As shown in Chapter 3.1, identical build errors cause greater band broadening in smaller pores. Therefore, the cross-sectional areas of the voids, rather than the solid cross-sectional areas were used to determine build error.

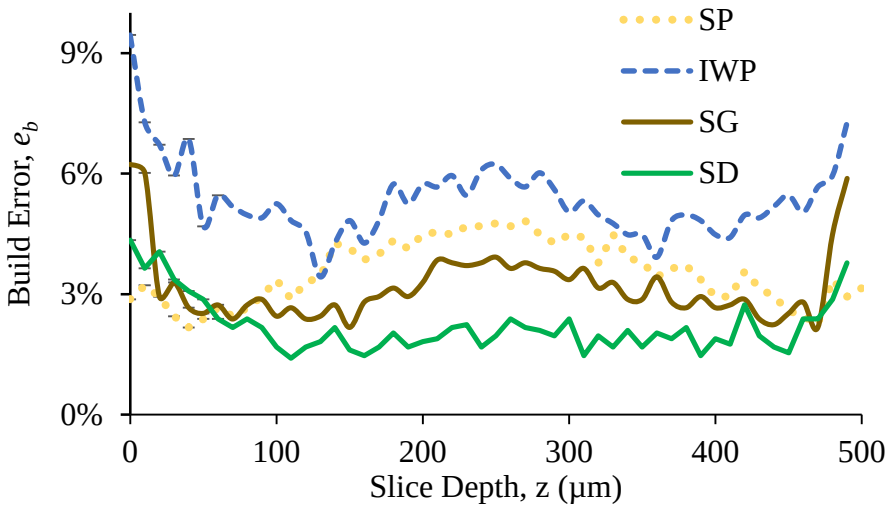

Figure 5.4: Build error e_b of printed samples of TPMS geometries with 8 confocal image stacks per geometry

For all geometries, the build errors up to a slice depth of z = 30 µm were the highest, after which a dramatic drop in e_b was consistently observed. A potential reason for this is that the peripheries of the column are most affected by post-processing. The distortion of the final structure due to de-waxing and sonication steps would be most prevalent in the outer portions of the porous grid. In the context of a full, enclosed column, only a small region in the immediately vicinity of the flow distributors is likely to be affected. Because this region represents less than 0.1 % of the total column volume, it can be safely assumed that the bulk of the column resembles data shown for z > 30 µm i.e. very close replication of the CAD model.

Amongst the TPMS structures, it can be seen that the Schwarz Primitive and IWP structures display the highest levels of build errors in certain regions. Due to the nature of these two geometries, which contain regions with small design cross-sectional surface areas, the relative build errors are higher. This implies that the two geometries are effectively less suitable for 3D-printing due to the regions with low 2D porosities. As in Chapter 3.1, such geometries can be expected to display greater amounts of band-broadening.

The Gyroid and S Diamond structures consistently exhibit smaller build errors due to having no such regions with low 2D porosities. Amongst the two geometries, the S Diamond structure contains the smallest build errors that is almost completely independent of slice

depth. A potential reason for this is the rotation of the geometry to align linear segments with the striations caused by the 3D-printer's extruder.

A key component in determining the merits of a structure produced using additive manufacturing is the suitability of a particular geometry to the manufacturing process, i.e. the printability of a geometry. The build error results shown here can be reasonably applied to fused deposition and a range of other foil or filament based printing mechanisms where striations similar to ones shown in Fig. 5.3 can be expected.

Another potential source of build errors, depending on the scales involved, is the discretization of the TPMS geometries. An important choice in the CAD modelling of these geometries is the resolution at which the stl CAD file would be produced. In this study, it was possible to build TPMS structures with good replicability with relatively small file sizes of 18-25 kB per unit-cell. At the tested scales, the limiting factor in achieving perfect definition of TPMS surfaces is the printer resolution, not the discretization of the smooth, curved surfaces into separate triangular elements during CAD modelling.

5.3.2 Reduced Plate Heights of TPMS Structures

The reduced plate heights for the TPMS geometries determined using the moment method are shown in Fig. 5.5, compared with the results obtained from CFD tests.

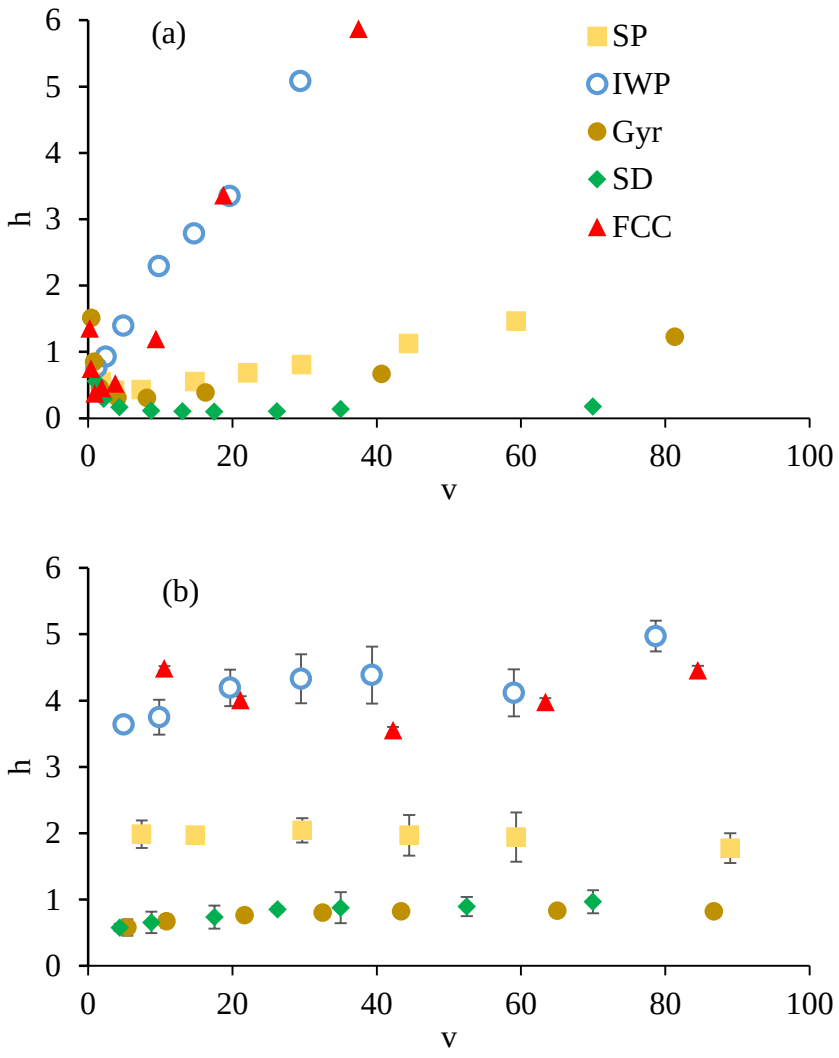

Figure 5.5: Reduced plate heights *h* of Schwartz Primitive (SP), IWP, Gyroid (Gyr), Schwartz Diamond (SD) and a face-centered cubic sphere arrangement (FCC) as a function of reduced velocity, *v*. (a) CFD values derived from Lattice-Boltzmann simulations on TPMS unit cells with periodic boundaries. (b) experimental values of 3D-printed columns.

In all CFD results, classical Van Deemter *h*-*v* profiles were observed, whereas for experimental results, the distinctive C-term contribution was lacking, possibly caused by a combination of the effects of spatial confinement, imperfect flow distribution and surface roughness in the 3D-printed columns. However, when comparing the relative performance of the geometries, CFD and experimental results are broadly in agreement. The Schwartz Diamond and Primitive structures were found to exhibit the lowest and highest reduced plate heights, respectively. Furthermore, the relative performance of the geometries also corresponded to their cubic crystal arrangements, consistent with previous computational studies on packed spheres [26,74,139], with the order of performance from lowest to highest plate heights being face-centered (Schwartz Diamond), body-centered (Schwartz IWP and Schoen

Gyroid) and simple cubic (Schwartz Primitive) TPMS geometries, in both CFD and experimental tests.

A notable inconsistency between the comparative performances of the geometries was for the IWP structure, in which experimental reduced plate heights were significantly higher than computational values. A potential explanation for this discrepancy is that imperfect flow distribution had a disproportionately large effect on structures possessing a lower tortuosity. The relatively low tortuosity of $\tau = 1.12$ for the IWP packing indicates there may have been insufficient radial mixing to negate the effects of a non-uniform flow distribution. In the computational model, this effect would not be relevant because the radial domain size is one unit-cell, with periodic boundary conditions, and there was a uniform inlet velocity profile, in contrast to the physical column, which may have had a non-ideal flow distribution profile. Consistent with this explanation, the experimental h_{min} values of the two low-tortuosity models, the Schwartz Primitive and the IWP (1.76 and 3.64 respectively), were significantly higher than both CFD results and the experimental results of the other TPMS geometries.

It is interesting to compare the TPMS geometries with the best performing sphere packing geometry, FCC. The experimental plate heights of FCC sphere geometry were superior only to those of the poorest performing TPMS structure, with an experimental h_{min} of 3.56. While this maybe an artefact of non-dimensional metric used in this sub-chapter, using the equivalent diameter used in Chapter 3.2 would still mean that the Gyroid and SD geometry outperform an FCC sphere packing.

In the experimental performance, it is also interesting to note the relatively low importance of specific surface area in determining the relative performance of the various geometries. Despite having virtually identical surface areas, the Gyroid and IWP structures displayed vastly different plate heights and although it has a significantly higher surface area, the performance of the FCC sphere geometry was inferior to most minimal surface structures. This strongly suggests that for macro-pores/non-permeable structures, surface area alone is not a sufficient indicator of dispersion when the size of the unit cell is controlled. Clearly, other parameters are more significant in governing the dispersion characteristics intrinsic to column microstructures.

Tortuosity is one such factor that has recently been shown to be correlated with column performance [187]. Another potential factor is the degree of homogeneity within a geometry. An increase in bed homogeneity to improve performance has been a recurring suggestion over the years in the literature on random sphere packing. In one sense, the use of a periodic unit cell structure provides homogeneity throughout a column but if the local variations within the unit cells are accounted for, a different picture emerges.

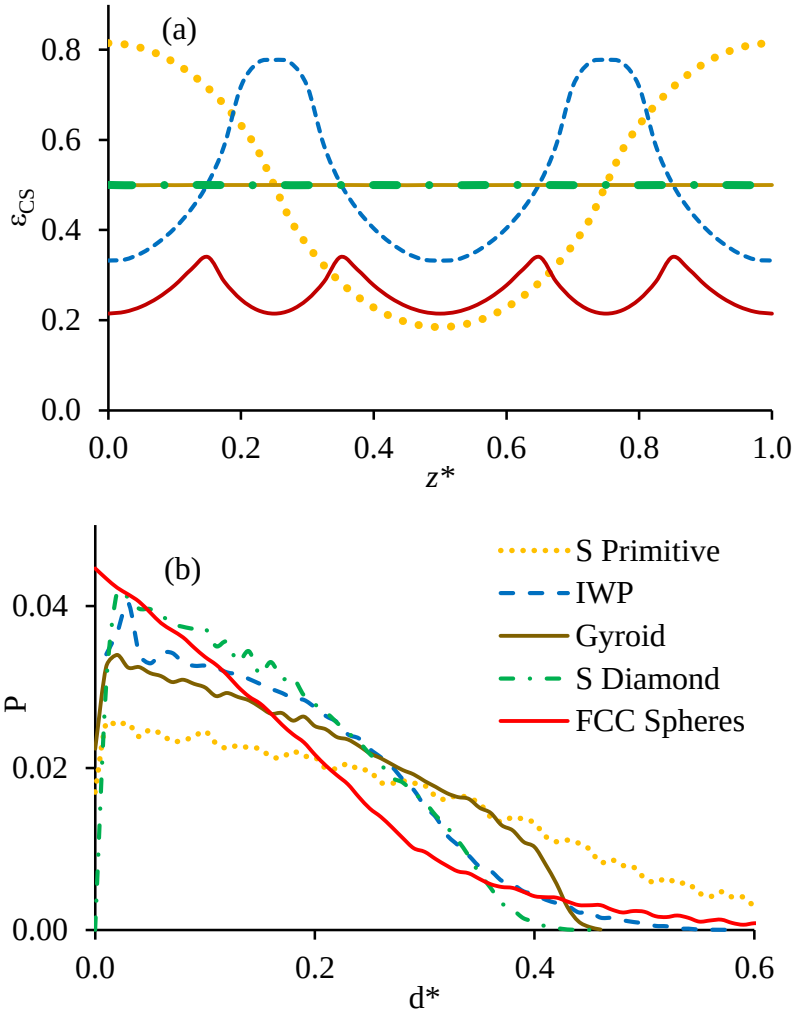

Figure 5.6: Porosity of 2D cross-sections of tested unit cells, ε_{CS} as a function of z-depth of cross-section z* = z/L. The yellow, blue, brown, green and red lines represent the schwartz primitive, iwp and schoen gyroid and schwartz diamond respectively. (b) nearest surface probability density function of a cubic lattice of 10000 points within the void spaces in a unitcell. The nearest surface data is filtered with a 3 point moving average function.

To quantify local homogeneity, the 2D or cross-sectional porosity, $\varepsilon_{CS,}$ of a unit cell, which reflects the variation in interstitial superficial velocity through the axial length, *L*, of the unit cell was used. A nearest surface function (nsf) was also calculated: a metric used by Schure *et al.* in comparing homogeneities of sphere packings[26]. Here, a probability distribution function is calculated for a point in the void space and its distance to the nearest solid surface.

The ε_{CS} profiles for the unit cells tested in this work are shown in Fig. 5.6. Notably, the two best performing geometries, the Schoen Gyroid and Schwartz Diamond, have uniform ε_{CS} profiles with the cross-sectional porosity being independent of z^*. The other two TPMS geometries show significant amplitudes, ($\Delta\varepsilon_{CS} = \varepsilon_{CS\ Max} - \varepsilon_{CS\ Min}$), in cross-sectional porosities with $\Delta\varepsilon_{CS} = 0.45$ and 0.63 for IWP and Schwartz Primitive, respectively, while face-centered cubic spheres have a relatively low $\Delta\varepsilon_{CS}$ value of 0.13. The periodic variation in cross-sectional area for FCC spheres shown in Fig. 5.6 is inevitable for any ordered sphere packing but the FCC arrangement provides the most homogenous ε_{CS} profile amongst FCC, BCC and SC arrangements and also exhibits the lowest plate heights. Thus, $\Delta\varepsilon_{CS}$ apparently reflects the comparative column performances with respect to reduced bed height seen in Fig. 5.5, with a lower value of $\Delta\varepsilon_{CS}$ corresponding to a lower value of h.

5.3.2 Flow Resistance and Separation Impedance

The permeabilities of the tested geometries are compared using a non-dimensional flow resistance metric, Φ defined in Eq. 5.3. Typical Φ values for packed bed columns range from 300 - 1500 for packed bed columns [191] while monolithic columns usually produce significantly lower flow resistances [192,193]. However, values for Φ vary significantly in the literature, with the range of reported values spanning several orders of magnitude for stationary phases. Significant discrepancies are also found between computational and experimental values, for example with FCC spheres [26,75]

For TPMS geometries, an experimental study of 3D-printed prototypes [186] reported values of dimensionless permeability that were consistently 40-50 times greater than the corresponding computational results [179]. Despite wide variation in quantitative values, there is qualitative agreement on the comparative pressure drop characteristics of several geometries. In this study, for the first time, the flow resistances of TPMS and sphere packings were compared using identical geometries in simulations and 3D-printed columns. The CFD and experimental values are listed in Table 5.2:

Table 5.2: Computational and experimental flow resistances and separation impedences for tested geometries

	Φ_{CFD}	Φ_{exp} (± 10)	$h_{min,CFD}$	$h_{min,exp}$ (± 0.1)	E_{min} (CFD)	E_{min} (Exp)
Schwartz Primitive	450	392	0.42	1.76	81	1208
Schoen IWP	791	216	0.40	3.64	126	2866
Schoen Gyroid	217	413	0.37	0.58	30	139
Schwartz Diamond	317	356	0.10	0.58	3	118
Spheres, Face-centered Cubic	1211	1092	0.32	3.56	122	13802

The CFD and experimental flow resistance values in Table 5.2 are broadly in agreement, with the exception of the IWP structure, which displays a significantly higher flow resistance in CFD simulations than in the experimental tests. As seen with other stationary phases, comparisons of absolute flow resistances are different to those reported in other studies but the comparisons between TPMS geometries remain consistent. Importantly, the flow resistances of all TPMS geometries are significantly lower than the tested sphere packing.

The minimum separation impedences of the geometries, E_{min} were also calculated, where

$$E_{min} = \Phi\, h_{min}^2 \qquad \textbf{Eq. 5.6}$$

Due to the lower minimum plate heights in the computational studies of the geometries, the minimum impedences are also significantly lower than the experimental values. In both computational and experimental results, the two geometries with $\Delta\varepsilon_{CS} = 0$ (The Gyroid and Schwartz Diamond) display significantly lower E_{min} values than other geometries.

The main difference between the 3D-printed and computational models is the presence of surface roughness in the form of striations, depicted in Fig. 5.3. As improvements in printer resolutions are made, the relative effects of these striations on the overall structure can be expected to decrease. Even with the presence of surface roughness, the macro-level effects of TPMS geometries greatly increases permeability compared to a packed bed of smooth spheres reported both in CFD and experimental studies.

5.3.3 Effects of Flow Orientation and Tortuosity

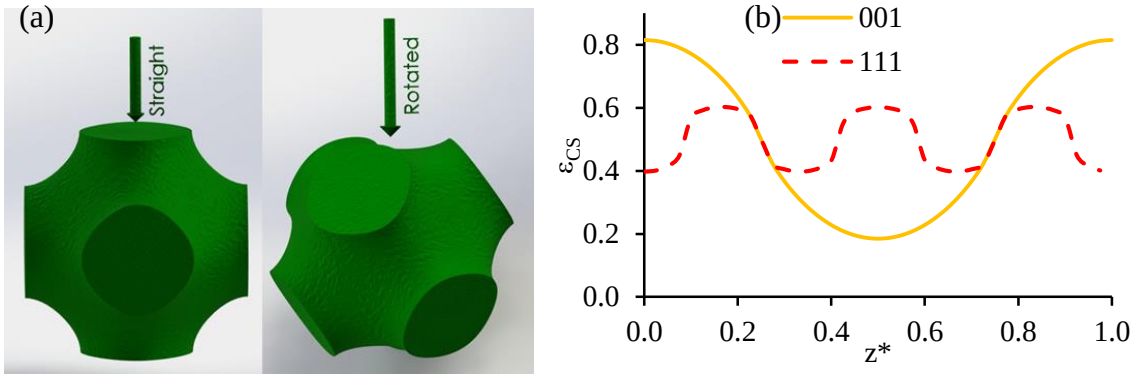

Figure 5.7: (a) The two flow orientations studied in the Schwartz Primitive geometry, Straight [001] and Rotated [111] and (b) cross-sectional porosity, $\Delta\varepsilon_{CS}$, as a function of z-depth, z* = z/L

In the TPMS geometry with the lowest tortuosity, the Schwartz Primitive, the structure contains parallel channels along the axial direction. In the 1-mm unit cell used in this study, this channel diameter is 0.50 mm. Clearly, this geometry is prone to back-mixing, stagnant regions in the transverse connecting channels and poor lateral mixing with the fluid flow oriented in the [001] direction. However, the performance could potentially be improved if the fluid flow followed the [111] direction because there would be a corresponding increase in tortuosity. To test this, a CAD model was produced with the S Primitive geometry rotated to the [111] orientation, as shown in Fig. 5.7 a. All other design parameters were identical to the initial model with the [001] orientation.

Significant changes can be observed in the cross-sectional porosity profiles between the two orientations, , with the variation in 2D porosity reduced from $\Delta\varepsilon_{CS} = 0.63$ to $\Delta\varepsilon_{CS} = 0.20$ (Fig. 5.7b), while the tortuosity τ was increased from $\tau = 1.03$ to $\tau = 1.28$, similar to those of the two best performing TPMS models, the Gyroid and Schwartz Diamond. The dispersion performance of the [111] S Primitive was dramatically improved to give a similar minimum experimental reduced plate height ($h_{min} = 0.54$) to those of the Gyroid and Diamond, as seen in Fig. 5.8.

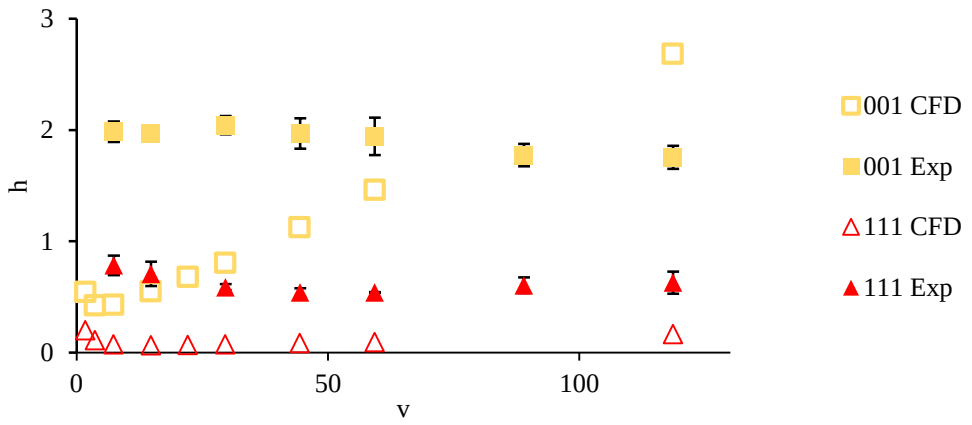

Figure 5.8: Reduced plate heights plotted against reduced velocity, v for Schwartz Primitive structure in the two tested flow orientations (a) Computational results, (b) Experimental RTD results from 3D-printed models

The substantial differences in experimental plate heights between the two Schwartz Primitive geometries, seen in Fig. 5.8 in both the CFD and experimental models underlines the importance of tortuosity and radial mixing in stationary phase structures. Tortuosity is particularly important in physical columns, with imperfect inlet distribution (as opposed to the homogenous inlet velocity profile used in CFD simulations), where high tortuosity and radial dispersion can more effectively continue to distribute the flow upon entry than in porous beds that have a relatively one-dimensional flow aligned with the major flow axis[187].

Despite the three-fold reduction in experimental h_{min}, there was only a marginal increase in flow resistance (Φ_{exp} = 573) with rotation of the structure from the [001] orientation (Φ_{exp} = 392). This resulted in almost an order of magnitude reduction in the experimental separation impedance (E_{min} = 167), indicating that performance gains in terms of lower dispersion significantly outweigh increases in backpressure when tortuosity is increased in TPMS structures.

However, while the S Primitive [111] had a similar tortuosity, its experimental h_{min} (0.54), was marginally lower than those of the Gyroid and Diamond TPMS geometries (h_{min} = 0.58 and 0.58 respectively). This shows that while increasing the tortuosity of a TPMS structure is clearly beneficial, it may not fully explain the behaviours of the tested geometries. The amplitude of the local cross-sectional porosity variation for the rotated [111] S Primitive was $\Delta\varepsilon_{CS}$ = 0.20, whereas it was zero for the two other columns. This shows that $\Delta\varepsilon_{CS}$ plays an important role in determining dispersion performance, possibly by reflecting local variations in tortuosity through the unit cell length.

More generally, there have long been questions on the exact role of tortuosity in determining the dispersion characteristics (plate height) of various porous geometries. In a conventional random packed bed, τ is often used as an indicator to predict, amongst other parameters, the column porosity and bed homogeneity. This clearly does not apply to the ordered geometries studied in this investigation but τ still has a significant effect on plate height, as the dramatic improvement in column performance by a simple rotation of a geometry to increase τ shows.

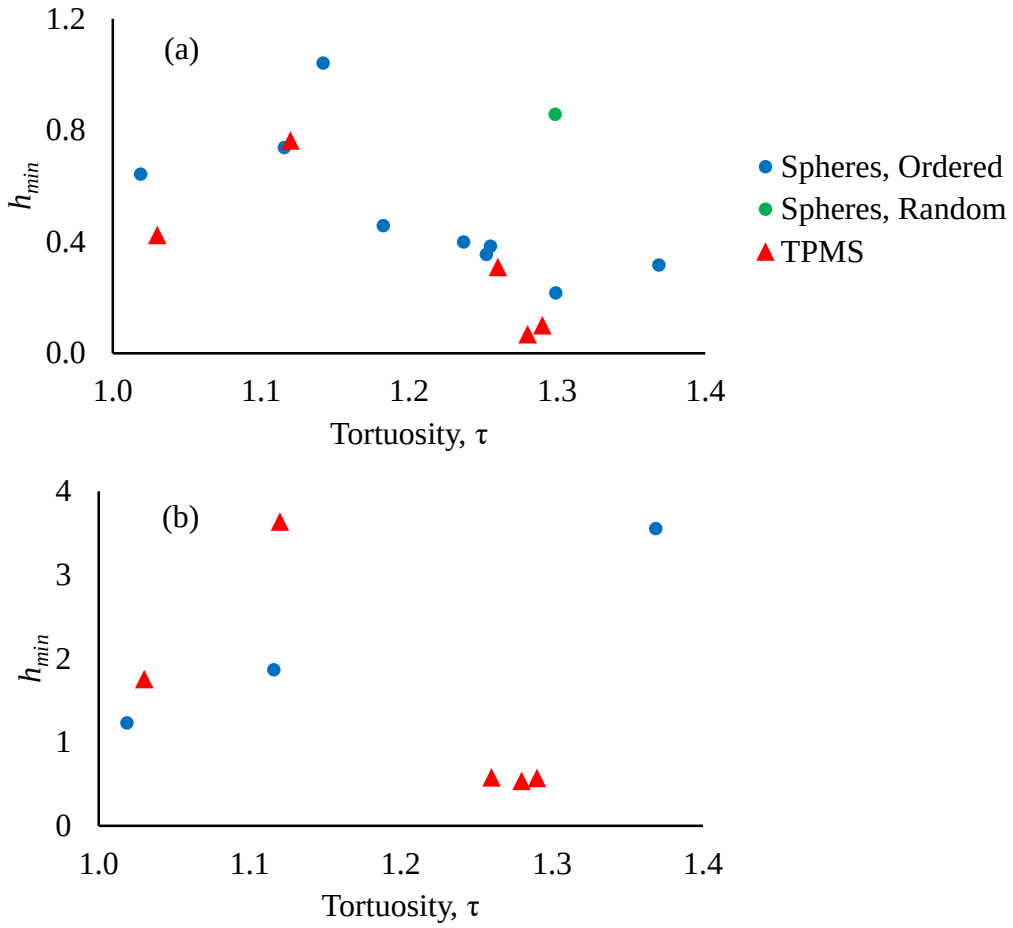

Figure 5.9: Minimum plate height h_{min} as a function of tortuosity τ for sphere packings and TPMS structures. (a) CFD data corroborated from Dolamore *el al.*[187] and (b) experimental results corroborated from Nawada *et al.*[162]

Figure 5.9 shows the effects of τ on column performance in ordered, periodic geometries, for both CFD and experimental values of reduced plate height from this and a previous study[187]. This compares the effect of tortuosity in TPMS structures to its effects on sphere packings. It is worth noting that the tortuosity is only determined computationally for both sets of data. In both cases, identical methods were used to obtain the plate height data for sphere packings and TPMS geometries.

A key consideration with this comparison is the characteristic dimension used to calculate the reduced plate heights. In computational studies, a strong correlation between tortuosity and

reduced plate height was observed with sphere packings[187], with higher tortuosities resulting in lower reduced plate heights. While a similar trend is also seen with TPMS geometries, comparing the two sets of geometries is a direct result of the characteristic dimension used. In a comparison of experimentally tested columns, the trend holds true for TPMS geometries. The same trend is also observed for the sphere packings if the characteristic dimension used in Chapter 3.2 is used. However, if the hydraulic diameter as defined in Eq 5.4 is used, the trend reverses. Tortuosity can therefore be said to indicate a reduction in h_{min} within a single category of geometries, with comparisons of different categories of geometries being dependent on the method used to arrive at a reduced pate height.

While clearly important, tortuosity, as calculated here, is not an *a-priori* geometrical characteristic of a structure and CFD simulations must be performed to determine τ. The two parameters tested here; τ and $\Delta\varepsilon_{CS}$, are necessary but not sufficient explanations for the differences observed between the ordered geometries.

5.3.7 Minimal Surface Sheets

For preliminary studies, TPMS structures in its most rudimentary geometrical form; i.e. network TPMS were tested. This section describes the variants of minimal surface geometries that can be created and fine-tuned using 3D-printing. To demonstrate the variants in which structures containing triply periodic minimal surfaces can be constructed, we use the example of a gyroid, which can be approximated as follows:

$$\sin(x)\cdot\cos(y)+\sin(y)\cdot\cos(z)+\sin(z)\cdot\cos(z)=0 \qquad \textbf{Eq. 5.7}$$

For simplicity, the equation is referred to as $Gyr(x,y,z) = 0$. In this form, it is only an infinitely thin surface, as shown in Fig. 5.10a and cannot be physically constructed. To create a network gyroid, as in this study, we introduce the following inequality:

$$Gyr(x,y,z) < t \qquad \textbf{Eq. 5.8}$$

with $t = 0$ for this study, as shown in Fig. 5.10b, with t representing the porosity of the network. For the purposes of this study, this value was uniform (at $\varepsilon = 0.50$) throughout the column and for all TPMS geometries. To divide the space into two separate channel networks, we define the following inequality:

$$|Gyr(x,y,z)| < m \qquad \textbf{Eq. 5.9}$$

The thickness of the separating wall defined by the constant *t*. A unit-cell of sheet TPMS is shown in Fig. 5.10c. The two flow units are separated by a wall with a uniform thickness (as long as $m < 1$). Each flow channel can be defined as $|Gyr(x,y,z)| > m$ for balanced TPMS and is geometrically identical to a network TPMS with $Gyr(x,y,z) < m$. Sheet TPMS are especially promising where controlled heat or mass transfer between the two flow units is required through the dividing wall.

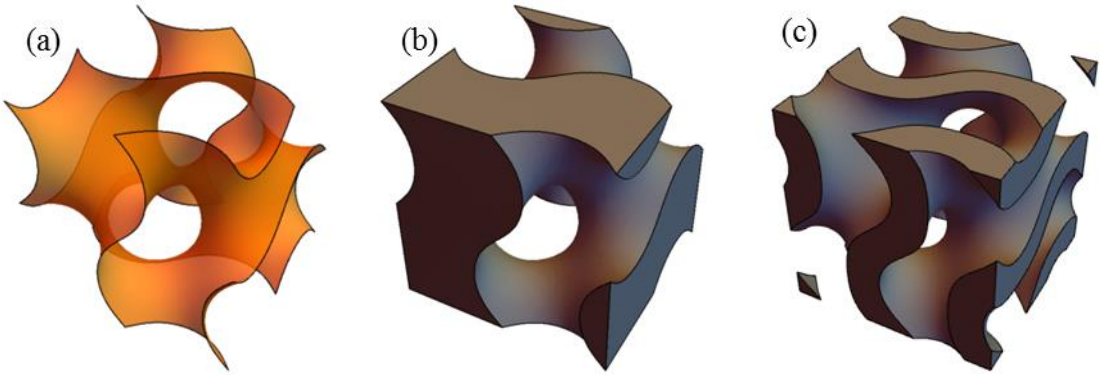

Figure 5.10: (a) basic gyroid surface, (b) network gyroid with $t = 0$, and (c) sheet gyroid with two interwoven flow channels and surface with thickness $m = 1$

This section describes dispersion studies performed on four sheet TPMS geometries. These tests can be used to establish the congruence of the two flow units and establish a working set of solutions for issues such as flow distribution. The material used to print these models was the impermeable resin used in the previous chapters. Invariably, the smallest and most challenging feature to 3D-print are the sheets themselves. The unit-cells used here were therefore 3.6 mm, compared to the 1 mm unit-cells used for the network TPMS. The sheet thickness *t* was set to $2\pi/9$, thereby creating walls with a thickness of 0.4 mm.

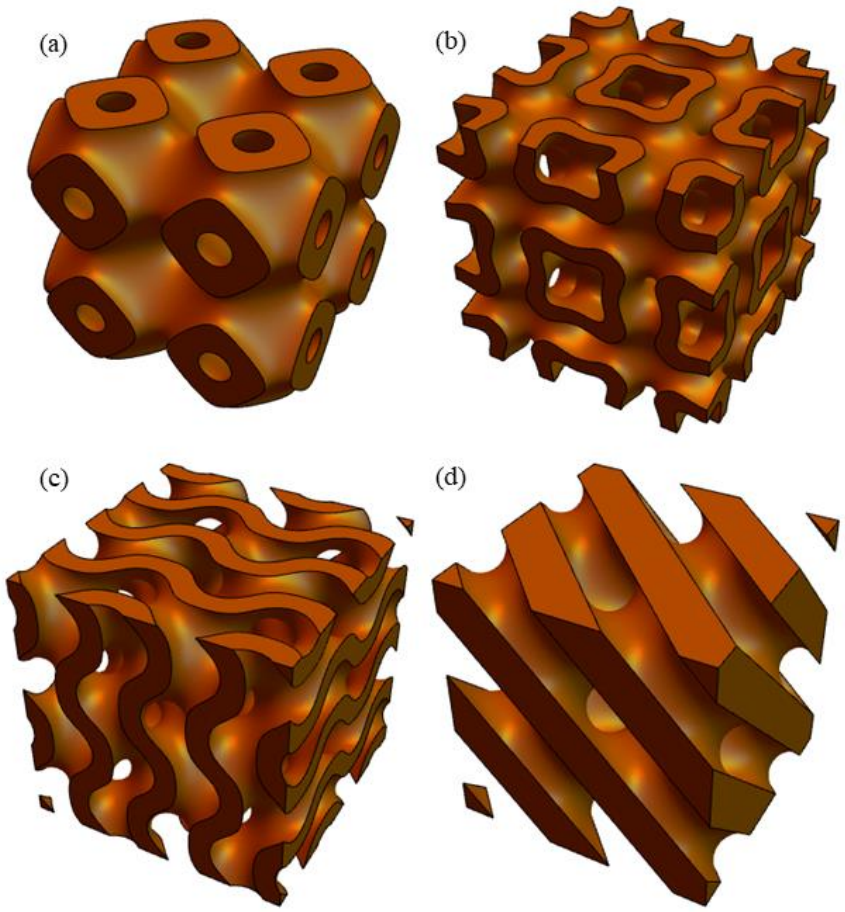

Figure 5.11: Sheet TPMS with *m* = 2π/9 (a) SP, (b) IWP, (c) SG and (d) SD

Figure 5.11 shows 2 × 2 × 2 unit-cells of the tested geometries. The unit-cells contain two sets of curved surfaces with a thin wall separating the two flow units. The presence of two curved surfaces mean that the .stl file created and exported using the parametric equations described in Eq. 5.9 were considerably larger than the network TPMS models (up to 500kB/unit-cell compared to 20 kB/unit-cell). This means that the patterning and assembly on the CAD software (Solidworks 2013) were significantly more computationally intensive. The printed models contained 8 × 8 × 20 unit-cells of the TPMS models. Creating models with a greater number of unit-cells using traditional CAD packages and desktop PCs (Intel i7 4790 Processor in this case) using this method would require impractically long computation times. Custom solutions to create the internal geometries, column walls and flow distributors would have to be created.

Sheet TPMS also pose very unique challenges with respect to flow distribution and collection. Two distributors must evenly distribute the two inlet flows only into their respective flow units without interfering with the other flow unit and distributor. The distributor setup used in

Chapter 3.2 and in the network TPMS study cannot be used here, as it does not allow for the selective flow into one flow unit or the interweaving of two identical distributors. The planar Mandelbrot H-tree distributor (used in Chapter 2) cannot be used directly if the two distributors are placed on an identical x-y plane. Furthermore, the two sets of inlet points for each flow units are offset by differing distances for each TPMS geometry. If l is the length of a unit-cell, the two sets of inlet points differ by $[\sqrt{l/2}, \sqrt{l/2}]$ in an x, y plane for the Schwartz Primitive and IWP sheets. For the Gyroid and Schwartz Diamond sheets, this offset is [0, l/2].

For the offset of $[\sqrt{l/2}, \sqrt{l/2}]$, a modified version of the H-tree described previously was designed, where the branches were angled to keep the two distributors separate, as seen in Fig. 5.12a. This arrangement does not suit the [0, l/2] offset. Therefore, I created an analogous distributor network with an X-tree which can be used for the Gyroid and Schwartz Diamond models. This does however, require a vertical offset of l/2 for one of the distributors (in red in Fig. 5.12b).

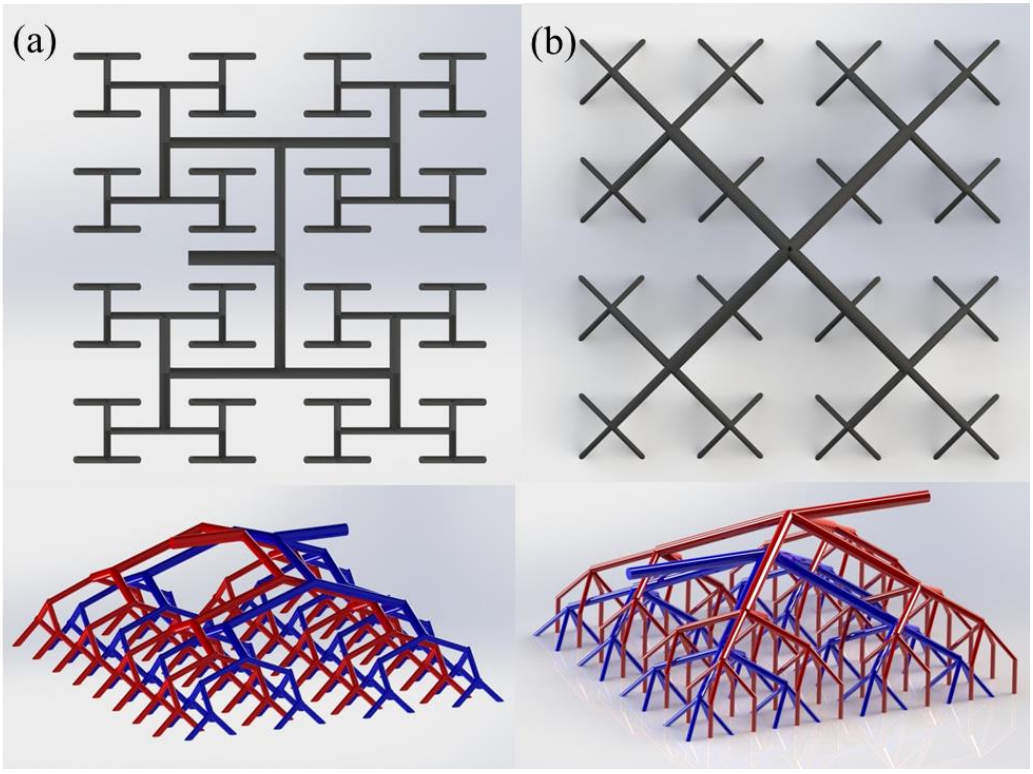

Figure 5.12: Fractal distributor templates for the proposed two-unit columns (a) Mandelbrot H-tree and (b) X-tree configurations. top: single branch top view, bottom: two interwoven branching networks

Due to the distributor designs, the columns were printed with a square cross-section in contrast to the cylindrical TPMS columns described previously. Four sets of standard 10-32 FPLC fittings were attached to the distributors. The resulting models are shown in Fig. 5.13.

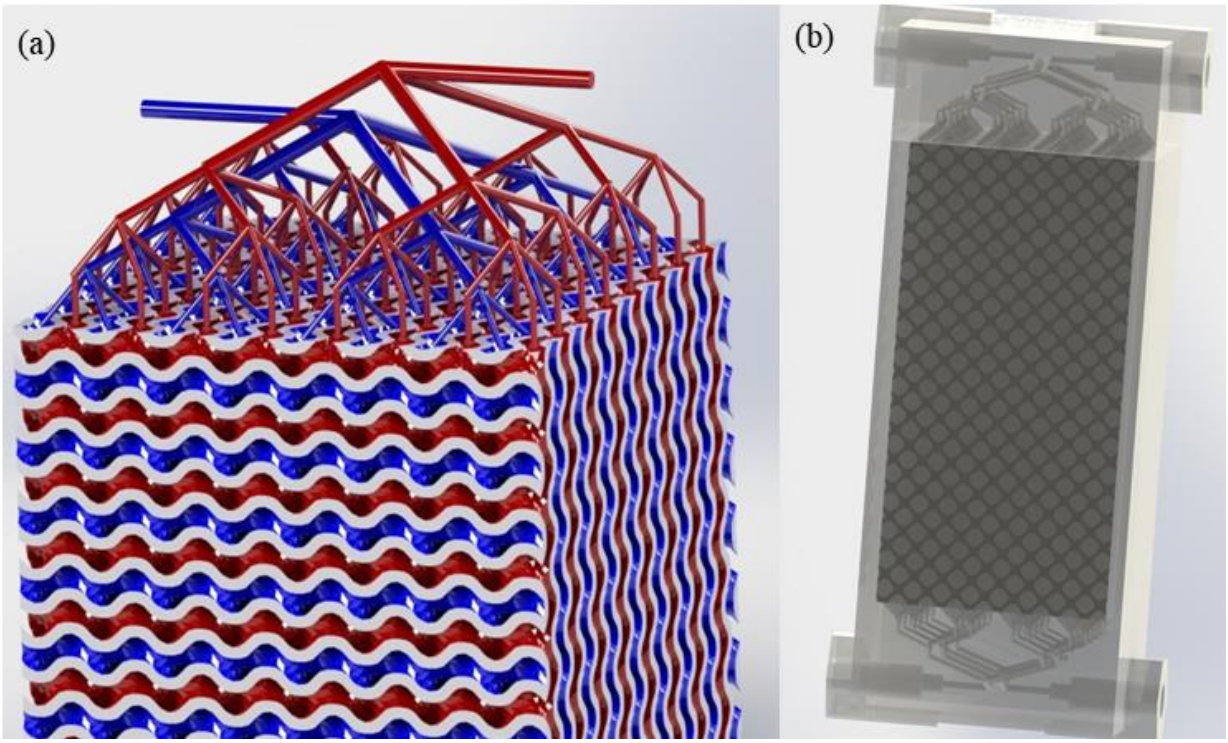

Figure 5.13: CAD model of a sheet gyroid column with interwoven X-tree distributors (a) the two separate flow systems (red and blue) and (b) final single piece model with 10-32 FPLC fittings

It is worth noting that unlike the previous tests, this was not a comparison of geometries with otherwise identical columns, but rather a comparison of both the geometry and its distributor. Additionally, the large characteristic dimensions (almost four-fold increase in hydraulic diameter compared to network TPMS) mean that B-term effects could not be observed in reasonable timeframes. By extension, the h_{min} values of each of the geometries were also unknown. However, the C-term effects of the columns and the congruence of the two flow channels could be tested. As with the previous studies, extra-column band broadening was accounted for by creating a control piece with the relevant interweaving distributor and subtracting the moments from the tracer curves. The Van Deemter curves for such sheet TPMS columns are shown in Fig. 5.14.

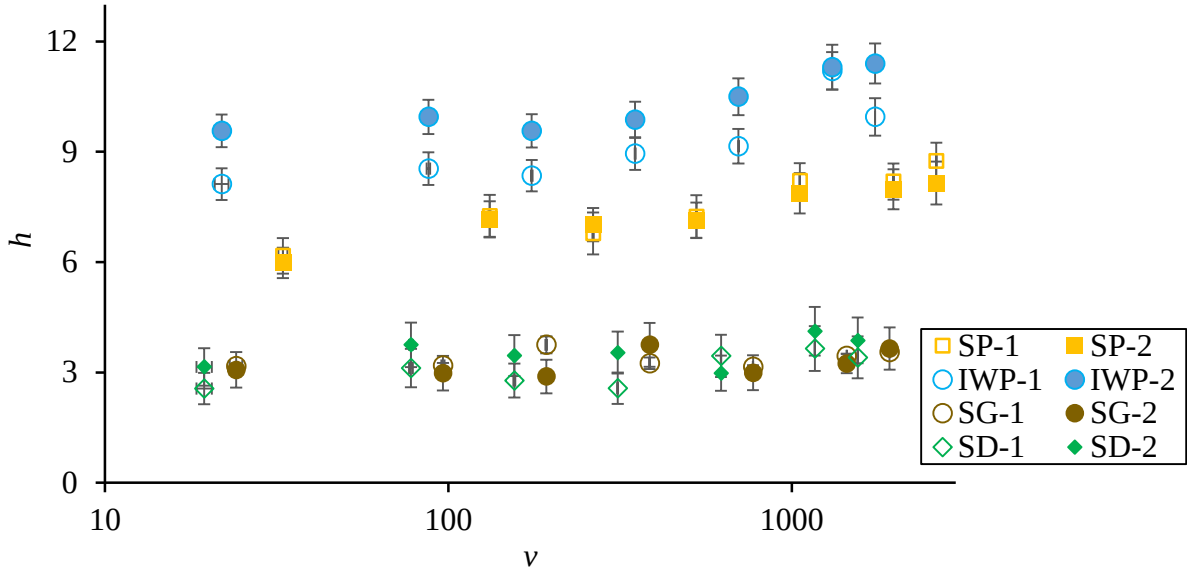

Figure 5.14: Van-Deemter curves of the sheet TPMS columns in flow units 1 (hollow) and 2 (filled).

The most noticeable difference between the sheet TPMS and the network TPMS is the significant increase in plate height. A potential reason for this increase is the square cross-section of the column, compared to the circular cross-section columns tested in the previous sections. However, the relative performance of the TPMS geometries mirror those found in network TPMS models.

For the P-G-D family of 'balanced' TPMS, the plate heights of the two flow units are nearly identical. This means that the printing process could meaningfully replicate the void geometries on both sides of the minimal surface sheets. The notable exception is the IWP geometry, where the two flow units differ significantly (τ = 1.14 and 1.04 for the two flow units). In computational tests performed by Fabian Dolamore, large differences in plate heights and flow resistances between $IWP(x,y,z) > G$ and $IWP(x,y,z) < G$ were found.

The implications of having two interconnected but separate flow channels with identical dispersion properties in liquid chromatography do not necessarily involve TPMS as stationary phases themselves. Possible uses of this geometry could involve the reduction of viscous heating effects in wide bore (4.6 mm ID) HPLC columns. Under very high back-pressures (> 1000 bar), the effects of viscous heating are proportional to D_C^2, where D_C is the column diameter[122,194]. The detrimental effects of heating related band-broadening has prevented the use of ultra-high performance liquid chromatography (UHPLC) for preparative scale separations.

Sheet TPMS columns with identical dispersion characteristics in both flow units could provide a range of solutions as column housings rather than stationary phases. One possible approach is using one flow unit for separations with packed particles and using the other flow unit for a coolant or a heating stream to maintain a set temperature. A wall-to-wall distance of 300-400 µm, possible with a range of current printing methods, would mean that radial temperature gradients within the packed part of the column would be negligible.

An alternative approach that exploits the identical dispersion properties would be to split the mobile phase and sample into two streams and flow the two streams counter-current to one another in the two flow-units. The counter-current flow could therefore mitigate axial temperature gradients for both flow-units while doubling the loading capacity of the column compared to the previous arrangement. Similar band-broadening profiles of the two flow-units mean that the two eluent streams could then be merged into a single stream for detection and fractionation.

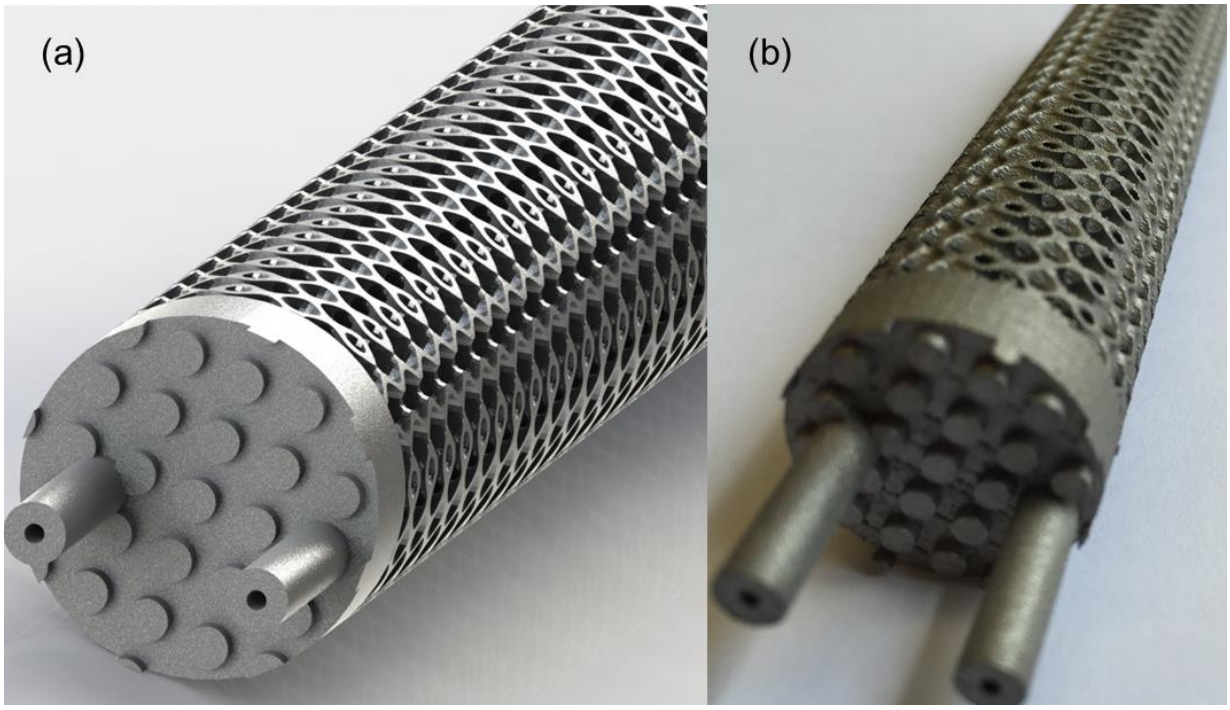

Figure 5.15: Schwartz primitive 20 mm ID heat exchanger, (a) CAD model and (b) 3D-printed model in stainless steel 316

A process unit that further exploits the geometrical characteristics of sheet TPMS is a heat exchanger. Here, the TPMS sheet is a dividing wall between two streams of hot and cold flow streams. TPMS geometries can facilitate radial mixing within each flow stream and therefore more radially homogenous temperature profiles, compared to conventional shell and tube heat exchangers. As a side project, I have designed TPMS heat exchangers to be 3D-printed

using selective laser melting (SLM) from Rapid Advanced Manufacturing (Tauranga, New Zealand). Figure 5.15 shows the CAD design and the final printed artefact. To remove the residual powder that results from the SLM process, heat exchangers were printed without walls and were later covered with ShrinkWrap tape to serve as walls. Experiments of the TPMS heat exchangers performed by Stefan Warnaar showed significantly higher heat transfer coefficients compared to literature values of shell and tube heat exchangers at only modest increases in pressure drops.

5.3.8 Other Variants of TPMS Geometries

Additive manufacturing also allows for the production of other such variants of TPMS structures. Each have their own implications, in liquid chromatography and in other process engineering applications. A variation of Eq. 5.9 can be used to define a double TPMS network with the structure that arises from:

$$|Gyr(x,y,z)| > t \qquad \textbf{Eq. 5.10}$$

Here, t defines the thickness of the void between two solid TPMS networks. The two solids would be congruent in their geometries and would be separated by a void zone with a uniform flat-to-flat distance between the two networks (shown in Fig. 5.16 a-c as green and red). In this case, a single flow unit with a single flow distributor is necessary.

If the two networks are printed with electrically conductive materials, the networks can be set to two different polarities to create a constant electrical field between the two surfaces. This can be used to achieve two simultaneous separations: one in time across the axial direction of the column (as in conventional chromatography) and a spatial separation towards one of the two networks (i.e. in the transverse direction). Two flow interweaving flow collectors, shown in Fig. 5.13 can be used to collect the analytes that have migrated closer to each network.

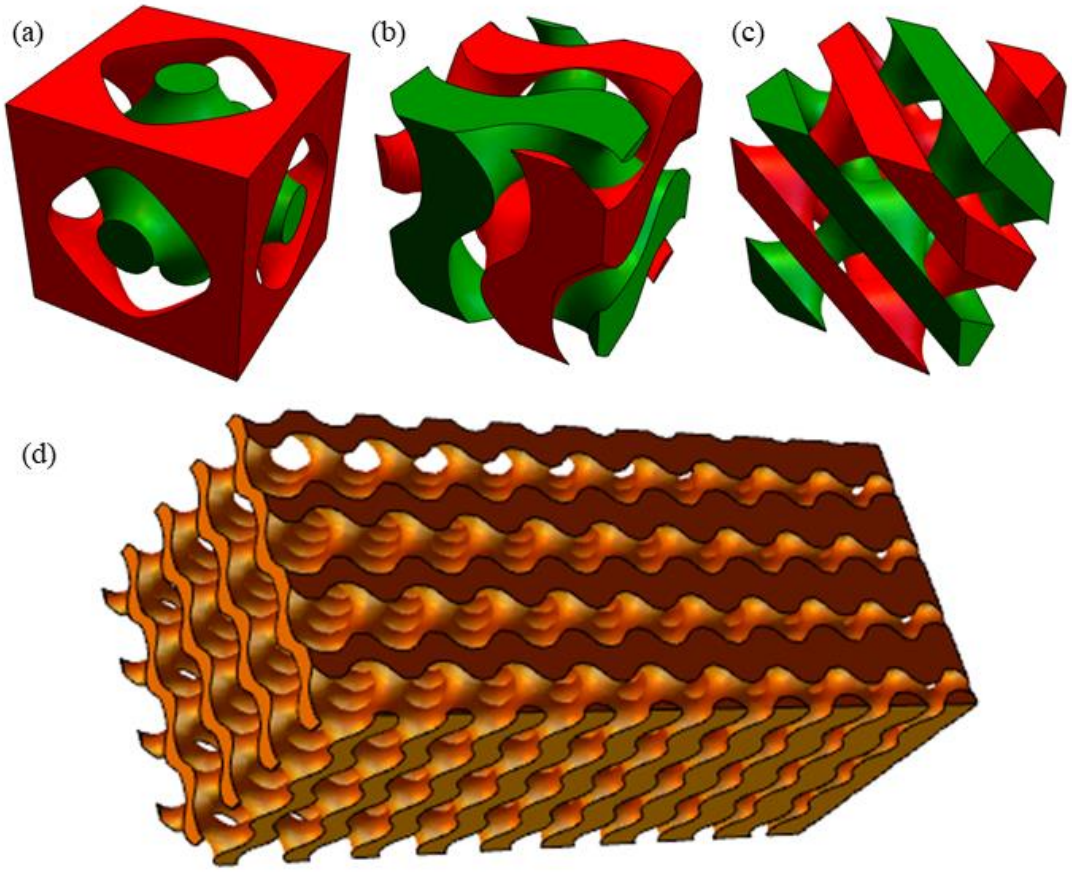

Figure 5.16: Double TPMS arrangements for (a) SP, (b) SG and (c) SD and (d) network gyroid with a porosity gradient

Further variations of TPMS geometries can be created by modifying the equations described in Eq 5.1. Instead of a constant such as *G* or *t*, this value in the equation can be related to the x, y or z position. The local porosity of a given region can therefore be defined by its x, y or z co-ordinates. An example that is relevant to liquid chromatography involves the creation of a porosity gradient across the axial direction of the column. This can be created as follows:

$$sin(x)\,cos(y) + sin(y)\,cos(z) + sin(z)\,cos(x) < k\,z + c, \qquad \textbf{Eq. 5.11}$$

where *k* and *c* define the porosity gradient along the z direction. A column with such a porosity gradient can be particularly useful in solid capture steps where a process analogous to size exclusion chromatography can be performed.

If the network is printed using a thermally conductive material for catalysis or affinity-based separations, a porosity gradient can create a gradient in heat flux across the column. This can also be used to negate undesirable temperature gradients due to viscous heating in liquid chromatography or exothermic reactions in catalyst porous beds.

More broadly, the variants of TPMS geometries discussed in this chapter have a wide variety of uses in process engineering. The homogenous geometries and lower flow resistances lend themselves to a broad range of applications where packed beds are currently used. The most significant advantage that 3D-printed TPMS structures provides is not necessarily its superior performance (in plate heights and flow resistance properties) but versatility and ability to tailor the geometry to specific separation needs.

5.4 Conclusions

The 3D-printed TPMS structures were reproduced with good fidelity at the tested scales. Both CFD and experimental results broadly agree as methods to compare the relative performances of the tested geometries. Furthermore, several column geometries were shown to exhibit lower plate heights than the best known spherical arrangement. However, significant differences were found between computational and experimental plate heights of the printed TPMS columns. The most substantial improvements were seen in the flow resistance properties of the minimal surfaces, with the overall separation impedances being significantly lower than sphere packed columns.

In particular, the Schoen Gyroid and the Schwartz Diamond geometries produced the least dispersion as well as the Schwartz Primitive geometry, when rotated to increase tortuosity. Therefore, the P-G-D family of minimal surfaces were shown to be the most favourable amongst the tested geometries.

This is the first attempt to characterize the performance of TPMS structures in the context of chromatography in either an experimental or a computational study. The findings can also potentially be applicable in a range of other unit operations where packed bed homogeneity and low flow resistances are desirable (e.g. process intensification). Further studies on retention and separations would be necessary to provide a more complete understanding of minimal surfaces in liquid chromatography.

The full range of implications of TPMS geometries in process engineering as a whole are only beginning to be explored. Further work on these geometries would involve using TPMS geometrical features to produce internally porous stationary phases with homogenous diffusion profiles. The results also underline the possibilities, enabled by 3D-printing, to shift from producing merely homogenous to optimized stationary and mobile phase geometries.

6. Conclusions and Future Perspectives

6.1 Concluding Remarks

As shown in the previous chapters, additive manufacturing or 3D-printing is a highly promising approach to create stationary phase geometries for liquid chromatography. The following conclusions can be drawn from the work described here:

- The majority of 3D-printing technologies do not currently offer the resolution that is necessary to build FPLC or HPLC-scale elements. However, a few technologies such as projection micro-stereolithography (photopolymerization) and micro selective laser melting (metal printing) have begun to approach the necessary resolution and part sizes in recent years.
- For characterization of porous micro-structures however, current inkjet 3D-printers offer acceptable resolutions (for solids capture applications i.e. > 200 µm) and structural robustness. Single-piece columns containing porous beds, column walls, distributors and FPLC fittings can be printed using this printing method. Residence time distribution studies indicate that flow distribution was just as important in reducing band-broadening as the porous bed micro-structure. A fractal bifurcating distributor proved to be most effective in reducing peak tailing.
- In comparing different ordered geometries, studies with elements with differing degrees of overlap showed that contrary to regular packed columns, a decrease in porosity does not result in narrower and more symmetrical peaks. Non-spherical (tetrahedral) particles were shown to out-perform spherical particles when placed in a simple cubic arrangement. Amongst particle arrangements, the face-centered cubic structure was shown to produce the least dispersion amongst the three main cubic crystal structures, supporting several computational findings.
- 3D-printing also enabled studies of columns with well-defined, deliberately introduced defects in the porous structures. Using such studies, it was possible to quantify the deleterious effects of line defects as a function of the defect size and determine the extent of radial dispersion into the line defect channel within different porous bed and defect geometries.
- In addition to creating ordered lattices of particle-like elements, whole monolithic networks can be 3D-printed to serve as porous beds. In particular, networks consisting

of triply periodic minimal surfaces were shown to produce significant reductions in plate height and column back-pressures. The reductions in overall experimental separation impedences of several orders of magnitude compared to the face-centered cubic spheres were found.

The conclusions listed above represent significant steps towards the creation of 3D-printed liquid chromatography columns and a comprehensive understanding of the effects of micro-structures on a column's final performance. However, several other studies can be performed to determine optimal geometries that would determine the final forms of the 3D-printed columns. Sections 6.2 and 6.3 described two recommendations for future experiments and research themes.

6.2 Cubic Voxel as a Unit Element

The plate height of a liquid chromatography column, H can be described as follows:

$$H = h\,d \qquad \textbf{Eq 6.1}$$

; where h is the non-dimensional plate height and d is the characteristic dimension of the geometry. Typically, d represents the particle diameter as the most dominant characteristic dimension used in LC. Any LC column can therefore be seen as consisting of building blocks or unit-elements that are discrete spheres, due to their ease of packing and the ease of manufacturing spherical beads with high precision. With spherical elements, it is widely established that a face-centered cubic arrangement is optimal for minimizing dispersion and achieving uniform flow throughout the column packing[26,138,145].

Given the practical limitations with printer resolutions (feature sizes 150 - 400 μm with common printing techniques), the relevant challenge to address is determining a geometry with the lowest possible characteristic dimension. The challenge can be defined by calculating the plate height H as a product of the 3D-printer's resolution as follows:

$$H = h\,b \qquad \textbf{Eq 6.2}$$

; where b is the minimum feature size that the 3D-printer can build. The aim for practical applicability of 3D-printers with limited resolution is to minimize the value b while maintaining a reasonably low h value. This is in contrast to the work presented in the previous chapters where the aim was to reduce h while non-dimensionalizing the plate heights with large characteristic dimensions (often > 500 μm). While such studies provide

insights into the relative advantages of various micro-structures, the usability of 3D-printing as a production technique for LC column depends on printed solid and void dimensions being as small as the printer can produce.

While a packed LC column consists of spherical unit-elements, any 3D-printed piece can be assumed to consist of a set of three-dimensional pixels, or voxels. The resolution of any printer can be quantified by the size of the voxels it can produce.

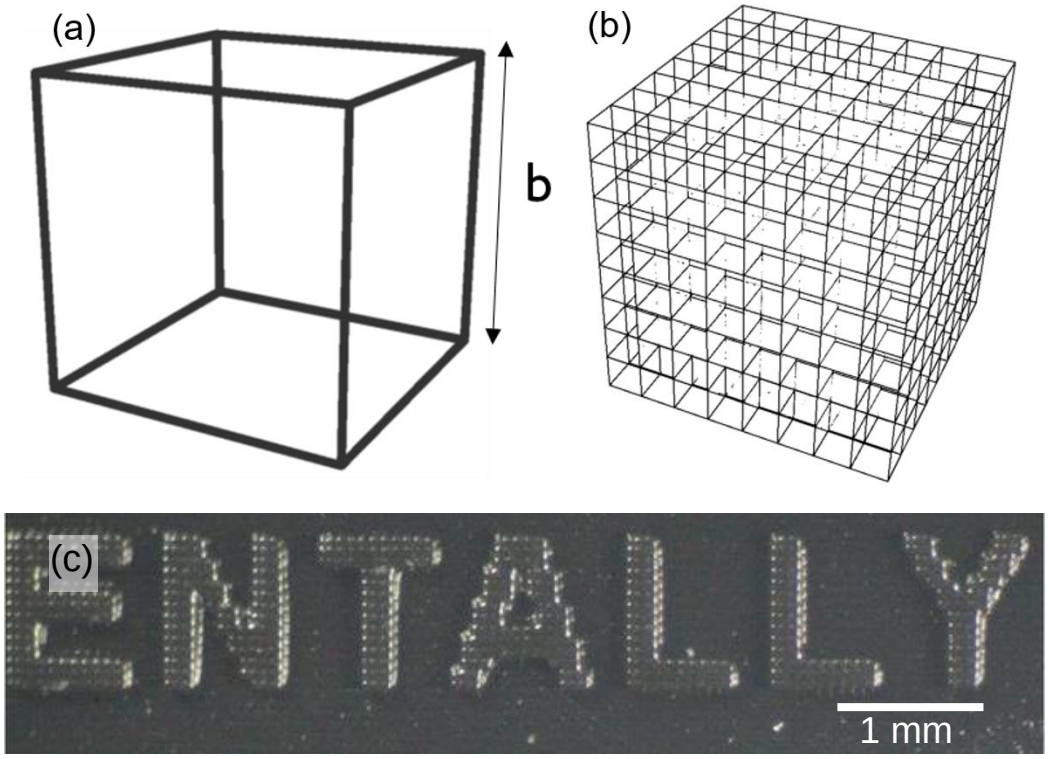

Figure 6.1: (a) cubic unit-element with a length *b*, (b) voxel array arrangement as a representation of the design space of a 3D-printer and (c) DLP printed piece showing the pixelation produced by its projector screen[195]

As a rough approximation, the unit-element can be assumed to be cubic voxel with a length *b* (Fig. 6.1a). Each voxel in a 3D-printed structure could be in two states: solid or void. The design space of any 3D-printer can therefore be assumed to be a three-dimensional matrix of voxels with each voxel in one of two states.

In reality, the shape of a voxel would be subtly different depending on the exact printing technology that is used. For example, in a multi-jet system used to create the columns studied in chapters 2 - 5, the voxel dimensions are based on the extruder's precision in the x and y directions (measured in dots per inch) and layer thickness in the z direction. The 3D-printer used to manufacture the majority of the models in the previous chapters has a nominal voxel size of 34 × 34 × 29 µm[90]. For a digital light projection (DLP) based system, the x-y

pixelation is clearly visible, as seen in Fig. 6.1c. For the purposes of this chapter, a voxel x, y and z can be assumed to be equal.

Regardless of the optimal geometries in the abstract (i.e. assuming an infinitely small voxel size), the aim that is relevant to 3D-printing is to discover the optimal arrangement of cubic voxels of a given size that achieves uniform flows and minimizes dispersion.

The properties of the two different geometries are significantly different. With cubic elements, contact between elements is surface-to-surface, as opposed to point-to-point (found in sphere packings). A surface-to-surface area of b^2 would create a more structurally robust geometry. Retaining frits are therefore not necessary to operate such packed beds at high flow-rates. The number of solid connecting faces, *cfs* and void connecting faces, *cfv* can be defined for each cell. Each 3D structure will therefore have a characteristic histogram for *cfs* and *cfv*. To build a porous stationary phase structure, the following geometrical requirements must be fulfilled:

- Each solid voxel must be connected to a minimum of two other solid voxels ($cfs \geq 2$ for all solid cells) to create a mechanically robust structure.
- To allow flow through void cells, an analogous condition should be applied to void voxels; i.e. $cfv \geq 2$ for all void cells.
- All solid voxels must form a single, interconnected, monolithic structure to prevent islands within the structure. An analogous condition must be applied to void voxels to prevent enclosed loops separate from the main flow channels.
- To ensure flow through the stationary phase structure, a continuous set of connecting void voxels along the z-direction (i.e. between the inlet and outlet of the column) must be present.

The parameters to be optimized are solid and void dimensions, *ds* and *dv*, specific surface area *s* and cross-sectional porosity, ε_{cs}. Other metrics related to the structural robustness and fluid permeability can also be defined by targeting a specific distribution of solid or void connecting faces.

Comparisons between different geometries can be made by studying the level of pixelation or voxelation that is necessary to fulfill the criteria described above. Figure 6.2 shows a comparison of three different voxelated geometries: A simple cubic grid, a highly voxelated gyroid and a face-centered cubic sphere unit-cell. The unit-cell length L_U (and consequently,

the extent of pixelation) was chosen as the minimum value for which the geometrical constraints on solid and void connecting faces and throughflow were fulfilled.

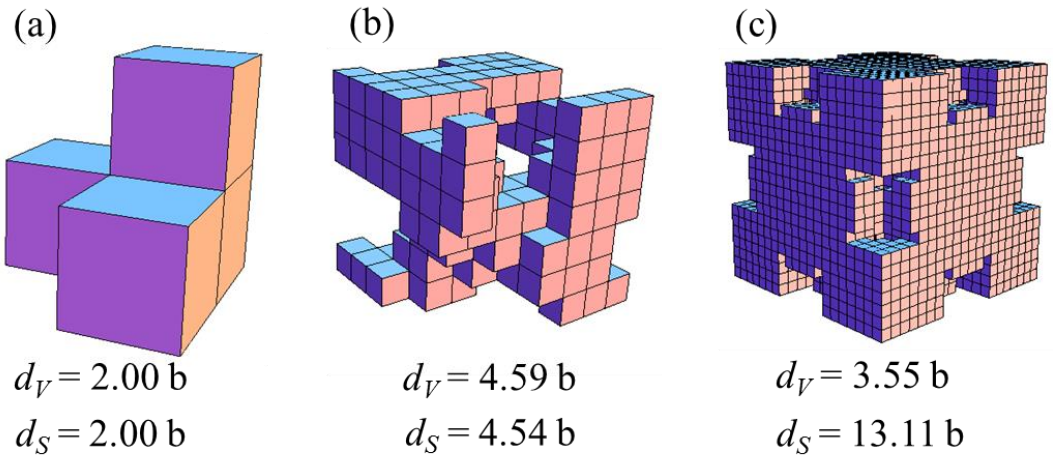

Figure 6.2: Pixelated unit-cells of (a) Simple cubic grid, (b) Network gyroid and (c) FCC Spheres.

Characteristic dimensions for the solid and void regions were calculated using the definition of a hydraulic diameter used in Chapter 5 (Eq 5.4). The solid cross-sectional areas were used to determine the solid characteristic dimension. The most apparent difference between the geometries are the d_v and d_s values that could be reasonably printed with a given printing resolution or voxel size b. For a printer with a defined b value printing at its maximum possible resolution, the characteristic void dimensions of a simple cubic grid would be roughly a half of the other two geometries. Therefore, marginal increases in reduced plate height suffered by the simple cubic arrangement may be preferable to the larger d_v values of the other two geometries.

Furthermore, the simple cubic grid can be defined by 2 × 2 × 2 voxels as opposed to 7 × 7 × 7 and 14 × 14 × 14 voxels (i.e. a 43 and 343-fold increase) for the gyroid and FCC sphere arrangements respectively. The radial and axial aspect ratios (i.e. number of repeating elements in a column) would be significantly lower for more spatially complex geometries such as those shown in Fig. 6.2b and c. A comparison of these geometries indicates that voxel arrangements that can reach low characteristic dimensions can be preferable to more 'optimal' (i.e. lower reduced plate heights) geometries that require larger printed features and a larger number of voxels.

6.3 Cellular Automata Based Structures

An interesting family of geometries that could serve as suitable voxel arrangements are geometries that take the form of cellular automata. The concept of cellular automaton (CA) was originally devised by John Von Neumann as a form of binary computation to create and study emergent phenomenon[196,197]. Typical CAs consist of two states (1 or 0) with a defined rule-sets. Each rule is an if-then statement that describes the output state for the next generation based on the arrangement of the previous generation. Figure 6.3 shows a common CA rule-set known as Rule 90[198]. In this case, each generation is visualized as a new layer. Given a certain initial arrangement or conditions, a myriad of geometries can be created.

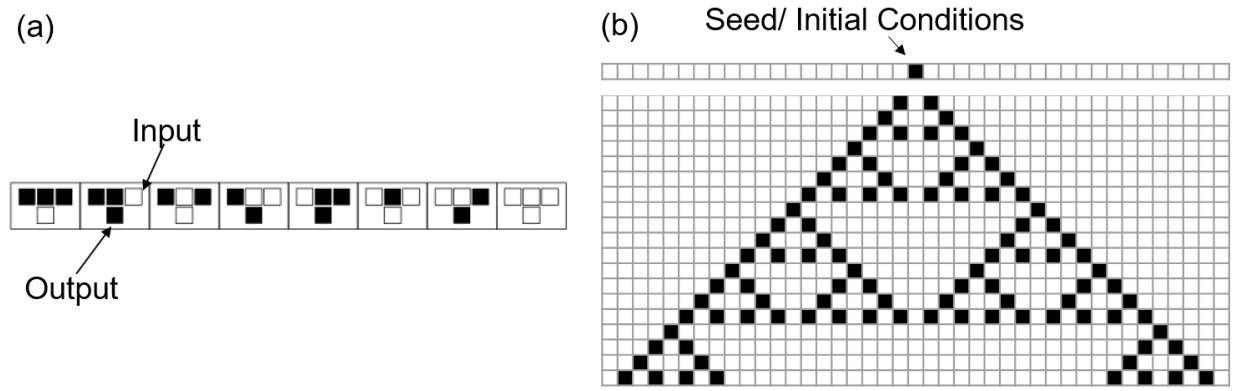

Figure 6.3: (a) Rule-set 90 with input cells above and the subsequent generation (output) below (b) applying rule-set to a single-seed initial condition

CAs have been used for a wide variety of applications, including simulating biological phenomenon[199], drug discovery[200] and cryptography[201,202] amongst many others. Some CA rule-sets have been shown to create stable, semi-ordered geometries[203,204]. If porous CA structures (i.e. combinations of rule-sets and initial conditions) with low d_s and d_v values and high tortuosities could be discovered, these could prove to be beneficial as voxel arrangements for LC columns.

Creating porous beds using CAs first requires creating three-dimensional structures based on the principles described above. This means that the format of the rule-set must be changed accordingly. A range of two-dimensional formats exist for such CAs but a simple 2 × 2 format is shown in Fig. 6.4, in which both the inputs and outputs are defined in a square consisting of four elements. A three-dimensional CA porous structure can be created where each generation is represented by a new layer of elements in which solid and void voxels can be defined.

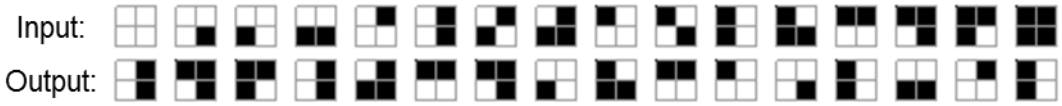

Figure 6.4: Cellular automata with (2×2) → (2×2) rule-set

The key challenge with CAs to create porous structures are to create rule-sets that ensure that the final geometry fulfil the requirements listed in the previous section (i.e. regarding number of connecting faces and preventing islanding of solid or void cells). As an exploratory study, a trial-and-error algorithm was created on Wolfram Mathematica 7.0 (Wolfram Research, Champaign, Illinois) to discover rule-sets which fulfilled the criteria listed above. Amongst these, the algorithm scouted for rule-sets that produced the lowest d_s and d_v values (1.52b and 1.55b respectively). The rule-set presented in Fig. 6.4 produced the lowest d_s and d_v values while still creating a monolithic block of solid cells and interconnected set of void cells with no islanding.

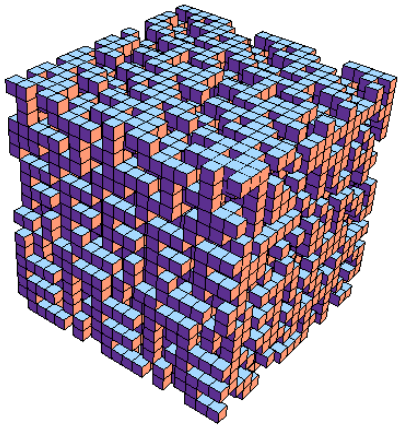

Figure 6.5: 20×20×20 structure created using a random seed and ruleset described in Fig. 6.4

The resulting geometries (an example shown in Fig. 6.5) are one of many geometries that can be created using a single rule-set, with scope for optimization of both the rule-set and initial conditions. Cellular automata are therefore an interesting category like many other to explore as a stationary phase geometry. 3D-printing will remain the enabling technology to investigate these and numerous other stationary phase microstructures.

References

1. Snyder, L. R. & Kirkland, J. J. Introduction to Modern Liquid Chromatography. 3rd Edition, *Materials Technology* 2-4 (1979).

2. Kazakevich, Y. & McNair, H. M. *HPLC for Pharmaceutical Scientists. Basic Liquid Chromatography* **8,** 13-44 (1996).

3. Carta, G. & Jungbauer, A. *Protein Chromatography: Process Development and Scale-Up*. *Protein Chromatography: Process Development and Scale-Up,* 20-22 (2010). doi:10.1002/9783527630158

4. Levinson, R. 5. Chromatography. *Modern Chemical Techniques* **34**, 117-159 (2001).

5. Poppe, H. *Fundamentals and Applications of Chromatography and Related Differential Migration Methods - Fundamentals and Techniques.* **69,** 12-24 (1992).

6. Grushka, E. Preparative chromatography. *Chromatographia* **8** (2) 53-58 (1975). doi:10.1007/BF02284348

7. Martin, A. J. P. & Synge, R. L. M. A new form of chromatogram employing two liquid phases. 1. A theory of chromatography 2. Application to the micro-determination of the higher monoamino-acids in proteins. *Trends in Biochemical Sciences* **2,** (1977).

8. Peters W. A., The Efficiency and Capacity of Fractionating Columns. *Journal of Industrial and Engineering Chemistry* **14,** 476–479 (1922).

9. Giddings, C. in *Part I. Principles and Theory* 2nd Edition, 335-336 (1965). *Dynamics of Chromatography*

10. Klinkenberg, A. & Zuiderweg, F. J. Longitudinal diffusion and resistance to mass transfer as causes of nonideality in chromatography. *Chemical Engineering Science* **5,** 271–289 (1956).

11. Knox, J. H. Practical aspects of LC theory. *Journal of Chromatographic Science* **15,** 352–364 (1977).

12. Horvath, C. & Lin, H. J. Movement and band spreading of unsorbed solutes in liquid chromatography. *Journal of Chromatography A* **126,** 401–420 (1976).

13. Billen, J. Rules to Improve Packing Structures Used in Liquid Chromatography. (PhD Thesis. Vrije Universiteit Brussel, 2008).

14. Darcy, H. Les fontaines publiques de la ville de Dijon. *Recherche* **5,** 256–258 (1856).

15. Kozeny, J. über kapillare Leitung des Wassers im Boden. *Sitzungsber Akademische Wissenschaft Wien* **136**(2a) 271–306 (1927).

16. Carman, P. C. Fluid flow through granular beds. *Chemical Engineering Research and Design.* **75,** S32–S48 (1997).

17. Ergun, S. *Fluid flow through packed columns*. *Chemical Engineering Progress* (1952). doi:citeulike-article-id:7797897

18. Gritti, F. & Guiochon, G. Mass transfer kinetics, band broadening and column efficiency. *Journal of Chromatography A* **1221,** 2–40 (2012).

19. Golay, M. Theory of chromatography in open and coated tubular columns with round and rectangular cross sections. in *Gas Chromatography 1958: Proceedings of the Second Symposium* 36–55 (1958).

20. Schisla, D. K., Ding, H., Carr, P. W. & Cussler, E. L. Polydisperse tube diameters compromise multiple open tubular chromatographyw. *AIChE Journal.* **39,** 946–953 (1993).

21. Regnier, F. E. Microfabricated monolith columns for liquid chromatography: Sculpting supports for liquid chromatography. *Journal of high resolution chromatography* **23,** 19–26 (2000).

22. He, B. & Regnier, F. Microfabricated liquid chromatography columns based on collocated monolith support structures. *Journal of Pharmaceutical and Biomedical Analysis* **17,** 925–932 (1998).

23. He, B., Tait, N. & Regnier, F. Fabrication of Nanocolumns for Liquid Chromatography. *Analytical Chemistry* **70,** 3790–3797 (1998).

24. Knox, J. H. Band dispersion in chromatography - A universal expression for the contribution from the mobile zone. *Journal of Chromatography A* **960** (1-2) 7-18 (2002). doi:10.1016/S0021-9673(02)00240-6

25. Schure, M. R., Maier, R. S., Kroll, D. M. & Davis, H. T. Simulation of packed-bed chromatography utilizing high-resolution flow fields: Comparison with models. *Analytical Chemistry* **74,** 6006–6016 (2002).

26. Schure, M. R., Maier, R. S., Kroll, D. M. & Davis, H. T. Simulation of ordered packed beds in chromatography. *Journal of Chromatography A* **1031,** 79–86 (2004).

27. Gzil, P., Vervoort, N., Baron, G. V. & Desmet, G. Advantages of Perfectly Ordered 2-D Porous Pillar Arrays over Packed Bed Columns for LC Separations: A Theoretical Analysis. *Analytical Chemistry* **75,** 6244–6250 (2003).

28. Gzil, P. De Smet, J. Vervoort, N. Verelst, H. Baron, G. V. Desmet, G. Computational study of the band broadening in two-dimensional etched packed bed columns for on-chip high-performance liquid chromatography. *Journal of Chromatography A* **1030,** 53–62 (2004).

29. De Smet, J. Gzil, P. Vervoort, M. Verelst, H. Baron, G. V. Desmet, G.. Influence of the pillar shape on the band broadening and the separation impedance of perfectly ordered 2-D porous chromatographic media. *Analytical Chemistry* **76,** 3716–3726 (2004).

30. De Smet, J. Gzil, P. Vervoort, N. Verelst, H. Baron, G. V. Desmet, G. On the optimisation of the bed porosity and the particle shape of ordered chromatographic separation media. in *Journal of Chromatography A* **1073,** 43–51 (2005).

31. Daneyko, A., Khirevich, S., Höltzel, A., Seidel-Morgenstern, A. & Tallarek, U. From random sphere packings to regular pillar arrays: Effect of the macroscopic confinement on hydrodynamic dispersion. *Journal of Chromatography A* **1218,** 8231–8248 (2011).

32. Li, L., Yan, X., Yang, J. & Wang, Q. Numerical investigation on band-broadening characteristics of an ordered packed bed with novel particles. *Appied. Energy* **185,** 2168–2180 (2017).

33. Deridder, S., Vanmessen, A., Nakanishi, K., Desmet, G. & Cabooter, D. Experimental and numerical validation of the effective medium theory for the B-term band broadening in 1st and 2nd generation monolithic silica columns. *Journal of Chromatography A* **1351,** 46-55 (2014). doi:10.1016/j.chroma.2014.04.099

34. Gzil, P., Baron, G. V. & Desmet, G. Computational fluid dynamics simulations yielding guidelines for the ideal internal structure of monolithic liquid chromatography columns. in *Journal of Chromatography A* **991,** 169–188 (2003).

35. Billen, J. & Desmet, G. Understanding and design of existing and future chromatographic support formats. *Journal of Chromatography A* **1168,** 73–99 (2007).

36. Baur, J. E., Kristensen, E. W. & Wightman, R. M. Radial Dispersion from Commercial High-Performance Liquid Chromatography Columns Investigated with Microvoltammetric Electrodes. *Analytical Chemistry* **60,** 2334–2338 (1988).

37. Reising, A. E., Schlabach, S., Baranau, V., Stoeckel, D. & Tallarek, U. Analysis of packing microstructure and wall effects in a narrow-bore ultrahigh pressure liquid chromatography column using focused ion-beam scanning electron microscopy. *Journal of Chromatography A* **1513,** 172–182 (2017).

38. Yew, B. G., Ureta, J., Shalliker, R. A., Drumm, E. C. & Guiochon, G. Mechanics of column beds: II. Modeling of coupled stress-strain-flow behavior. *AIChE Journal*. **49,** 642–664 (2003).

39. Daneyko, A., Hlushkou, D., Khirevich, S. & Tallarek, U. From random sphere packings to regular pillar arrays: Analysis of transverse dispersion. *Journal of Chromatography A* **1257,** 98–115 (2012).

40. Smits, W., Deridder, S. & Desmet, G. The impact of flow distribution on column performance: A computational fluid dynamics study. *Journal of Chromatography A* **1369,** 125–130 (2014).

41. Lode, F. G., Rosenfeld, A., Yuan, Q. S., Root, T. W. & Lightfoot, E. N. Refining the scale-up of chromatographic separations. in *Journal of Chromatography A* **796,** 3–14 (1998).

42. Vangelooven, J. & Desmet, G. Computer aided design optimisation of microfluidic flow distributors. *Journal of Chromatography A* **1217,** 6724–6732 (2010).

43. Yamada, M., Hirano, T., Yasuda, M. & Seki, M. A microfluidic flow distributor generating stepwise concentrations for high-throughput biochemical processing. *Lab on a Chip* **6,** 179–184 (2006).

44. Davydova, E., Deridder, S., Eeltink, S., Desmet, G. & Schoenmakers, P. J. Optimization and evaluation of radially interconnected versus bifurcating flow distributors using computational fluid dynamics modelling. *Journal of Chromatography A* **1380,** 88–95 (2015).

45. Liekens, A. Billen, J, Sherant R, Ritchie H, Denayer J, Desmet, G. High performance liquid chromatography column packings with deliberately broadened particle size distribution: Relation between column performance and packing structure. *Journal of Chromatography A* **1218,** 6654–6662 (2011).

46. Jespers, S., Deridder, S. & Desmet, G. A microfluidic distributor combining minimal volume, minimal dispersion and minimal sensitivity to clogging. *Journal of Chromatography A* **1537,** 75–82 (2018).

47. Mandelbrot, B. B. *The Fractal Geometry of Nature*. *American Journal of Physics* **51**(3) 286-290 (1983). doi:10.1017/CBO9781107415324.004

48. Luo, L. & Tondeur, D. Multiscale optimization of flow distribution by constructal approach. *China Particuology* **3,** 329–336 (2005).

49. Wang, L., Fan, Y. & Luo, L. Lattice Boltzmann method for shape optimization of fluid distributor. *Computers and Fluids* **94,** 49–57 (2014).

50. Pistoresi, C., Fan, Y. & Luo, L. Numerical study on the improvement of flow distribution uniformity among parallel mini-channels. *Chemical Engineering and Processing: Process Intensification* **95,** 63–71 (2015).

51. Luo, L. & Tondeur, D. Optimal distribution of viscous dissipation in a multi-scale branched fluid distributor. *International Journal of Thermal Sciences* **44,** 1131–1141 (2005).

52. Yue, J. Boichot R, Luo L, Gonthier Y, Chen G, Yuan Q, Flow distribution and mass transfer in a parallel microchannel contactor integrated with constructal distributors. *AIChE Journal.* **56,** 298–317 (2010).

53. Wouters, B. Davydova E, Wouters S, Vivo-Truyols G, Schoenmakers PJ, Eeltink S. Towards ultra-high peak capacities and peak-production rates using spatial three-dimensional liquid chromatography. *Lab on a Chip* **15,** 4415–4422 (2015).

54. Kearney, M. M., Peterson, K., Vervloet, T. & Mumm, M. W. US5354460A, Fluid transfer system with uniform fluid distributor, Amalgamated Sugar Co (1994).

55. Seibert, A. F., Lewis, J. L. & Fair, J. R. Mass Transfer Efficiency of a Packed Bed Utilizing the Fractal Distributor. *Separations Research Program* (2002).

56. Park, Y. J., Yu, T., Yim, S. J., You, D. & Kim, D. P. A 3D-printed flow distributor with uniform flow rate control for multi-stacked microfluidic systems. *Lab on a Chip* **18,** 1250–1258 (2018).

57. Op de Beeck, J., De Malsche, W., Tezcan, D. S., De Moor, P. & Desmet, G. Impact of the limitations of state-of-the-art micro-fabrication processes on the performance of pillar array columns for liquid chromatography. *Journal of Chromatography A* **1239,** 35–48 (2012).

58. De Malsche, W., Op De Beeck, J., De Bruyne, S., Gardeniers, H. & Desmet, G. Realization of 1 × 10 6 theoretical plates in liquid chromatography using very long pillar array columns. *Analytical Chemistry* **84,** 1214–1219 (2012).

59. De Malsche, W. De Bruyne S, Op De Beek J, Sandra P, Gardeniers H, Desmet G, Lynen F, Capillary liquid chromatography separations using non-porous pillar array columns. *Journal of Chromatography A* **1230,** 41–47 (2012).

60. Op De Beeck, J. Callewaert M, Ottevaere H, Gardeniers H, Desmet G, De Malsche W, On the advantages of radially elongated structures in microchip-based liquid chromatography. *Analytical Chemistry* **85,** 5207–5212 (2013).

61. De Pra, M. Kok, W. Th, Gardeniers, J. G.E.,Desmet, G.,Eeltink, S.,Van Nieuwkasteele, J. W., Schoenmakers, P. J. Experimental study on band dispersion in channels structured with micropillars. *Analytical Chemistry* **78,** 6519–6525 (2006).

62. De Malsche, W. Eghbali H, Clicq D, Vangelooven J, Gardeniers H, Desmet G. Pressure-Driven Reverse-Phase Liquid Chromatography Separations in Ordered Nonporous Pillar Array Columns. *Analytical Chemistry* **79,** 5915–5926 (2007).

63. Callewaert, M. De Beeck, J., Ottevaere, H., Gardeniers, H., Desmet, G., De Malsche, W. Integration of uniform porous shell layers in microfabricated pillar array columns by electrochemical anodization. in *2013 Transducers and Eurosensors XXVII: The*

17th International Conference on Solid-State Sensors, 1997–2000 (2013). doi:10.1109/Transducers.2013.6627188

64. Sandra, K. Vandenbussche J, T'Kindt R, Claerebout B, De Beeck J, De Malsche W, Desmet G, Sandra P. Evaluation of micro-pillar array columns (µPAC) combined with high resolution mass spectrometry for lipidomics. *LC GC Spec. Issues* **30,** 6–13 (2017).

65. Eghbali, H., de Malsche, W., Clicq, D., Gardeniers, H. & Desmet, G. Pressure-driven Chromatography in Perfectly Ordered Pillar Array Columns. *LC-GC Europe.* **20,** 208–222 (2007).

66. De Malsche, W. Zhang L, Op De Beeck J, Vangelooven J, Hiraoka M, Yamashita I, Majeed B, Op de Beeck, Fiorini P, Desmet G. Ion-pair reversed phase liquid chromatography of DNA in deep-UV patterned silicon pillar arrays. *Proceedings 14th International Conference on Miniaturized Systems for Chemistry and Life Sciences* **1408,** 1736–1738 (2010).

67. Illa, X. De Malsche W, Bomer J, Gardeniers H, Eijkel J, Morante JR, Romano-Rodríguez A, Desmet G, An array of ordered pillars with retentive properties for pressure-driven liquid chromatography fabricated directly from an unmodified cyclo olefin polymer. *Lab on a Chip* **9,** 1511–1516 (2009).

68. Op De Beeck, J., De Malsche, W., De Moor, P. & Desmet, G. Hydrodynamic chromatography separations in micro- and nanopillar arrays produced using deep-UV lithography. *Journal of Separation Science***35,** 1877–1883 (2012).

69. Vervoort, N., Billen, J., Gzil, P., Baron, G. V. & Desmet, G. Importance and reduction of the sidewall-induced band-broadening effect in pressure-driven microfabricated columns. *Analytical Chemistry* **76,** 4501–4507 (2004).

70. Op De Beeck, J. Callewaert M, Ottevaere H, Gardeniers H, Desmet G, De Malsche W. Suppression of the sidewall effect in pillar array columns with radially elongated pillars. *Journal of Chromatography A* **1367,** 118–122 (2014).

71. De Malsche, W., Desmet, G. & Devenyns, J. PharmaFluicis - Products. Available at: https://www.pharmafluidics.com/. (Accessed: 4th July 2018)

72. Maikin, D. S., Wel, B., Fogiel, A. J., Staats, S. L. & Wirth, M. J. Submicrometer plate heights for capillaries packed with silica colloidal crystals. *Analytical Chemistry* **82,** 2175–2179 (2010).

73. Wu, Z., Wei, B., Zhang, X. & Wirth, M. J. Efficient Separations of Intact Proteins Using Slip-Flow with Nano-Liquid Chromatography–Mass Spectrometry. *Analytical Chemistry* **86,** 1592–1598 (2014).

74. Yan, X. & Wang, Q. Numerical investigation into the effects of ordered particle packing and slip flow on the performance of chromatography. *Journal of Separation Science* **36,** 1524–1529 (2013).

75. Rogers, B. J. & Wirth, M. J. Slip Flow through Colloidal Crystals of Varying Particle Diameter. *ACS Nano* **7,** 725–731 (2013).

76. Wu, Z., Rogers, B. J., Wei, B. & Wirth, M. J. Insights from theory and experiments on slip flow in chromatography. *Journal of Separation Science* **36,** 1871–1876 (2013).

77. Liao, T., Guo, Z., Li, J., Liu, M. & Chen, Y. One-step packing of anti-voltage photonic crystals into microfluidic channels for ultra-fast separation of amino acids and peptides. *Lab on a Chip* **13,** 706–713 (2013).

78. Pawlowski, S. Nayak, N., Meireles, M., Portugal, C.A.M., Velizarov, S., Crespo, J.G., CFD modelling of flow patterns, tortuosity and residence time distribution in monolithic porous columns reconstructed from X-ray tomography data. *Chemical Engineering Journal*. **350,** 757–766 (2018).

79. Healthcare, G. E. Ion Exchange Chromatography & Chromatofocusing: Principles and Methods. (2007). Available at: https://www.sigmaaldrich.com/content/dam/sigma-aldrich/docs/Sigma-Aldrich/General_Information/1/ge-ion-exchange-chromatography.pdf. (Accessed: 3rd August 2018)

80. Ascentis® Express C18, 2 Micron UHPLC Column. (2018). Available at: Ascentis® Express C18, 2 Micron UHPLC Column%0A. (Accessed: 3rd June 2018)

81. Bird, S. S. & Kristal, B. S. Serum Lipidomics Profiling using an Ascentis Express Fused - Core C18 Column. 1–4 (2014). Available at: https://www.sigmaaldrich.com/technical-documents/articles/reporter-

us/serumlipidomics-profilingfusedcore-c18column.html. (Accessed: 3rd June 2018)

82. Healthcare, G. E. Ion Exchange Chromatography & Chromatofocusing: Principles and Methods. (2007).

83. Product Catalogue - Ascentis® Express C18, 2 Micron UHPLC Column. (2018).

84. Wessarges, Y. Hagemann R, Gieseke M, Noelke C, Kaierle S, Schmidt WP, Schmitz K, Haferkamp H, Additive Manufacturing of Vascular Implants by Selective Laser Melting. *Biomedical Engineering / Biomedizinische Technik* **59,** (2014).

85. Inc., S. Product Catalogue: Turnkey Metal Additive Manufacturing Systems for Production Parts, Prototypes, & Part Repairs. (2018). Available at: http://www.sciaky.com/additive-manufacturing/metal-additive-manufacturing-systems. (Accessed: 4th July 2018)

86. Sandron, S. Heery, B., Gupta, V.,Collins, D., Nesterenko, E P.,Nesterenko, P N., Talebi, M.,Beirne, S., Thompson, F., Wallace, G G., Brabazon, D., Regan, F., Paull, B 3D-printed metal columns for capillary liquid chromatography. *Analyst* **139,** 6343–6347 (2014).

87. Gupta, V., Beirne, S., Nesterenko, P. N. & Paull, B. Investigating the Effect of Column Geometry on Separation Efficiency using 3D Printed Liquid Chromatographic Columns Containing Polymer Monolithic Phases. *Analytical Chemistry* **90,** 1186–1194 (2018).

88. Gupta, V. Talebi M, Deverell J, Sandron S, Nesterenko PN, Heery B, Thompson F, Beirne SW, Gordon G, Paull B. 3D printed titanium micro-bore columns containing polymer monoliths for reversed-phase liquid chromatography. *Analytica Chimica Acta* **910,** 84–94 (2016).

89. Stratsys. Product Catalogue: Objet350 and Objet500 Connex3. *System Specifications* (2016). Available at: http://www.stratasys.com/~/media/Main/Files/Machine_Spec_Sheets/PSS_PJ_Connex3.ashx.

90. 3DSystems. Product Catalogue: ProJet® 3500 SD & HD. *ProJet SD & HD Printers* (2013). Available at:

https://www.3Dsystems.com/sites/default/files/projet_3500_plastic_0115_usen_web.pdf. (Accessed: 4th June 2018)

91. CustomPartnet. Jetted Photopolymer. (2015). Available at: http://www.custompartnet.com/wu/jetted-photopolymer. (Accessed: 10th May 2015)

92. Macdonald, N. P., Currivan, S. A., Tedone, L. & Paull, B. Direct Production of Microstructured Surfaces for Planar Chromatography Using 3D Printing. *Analytical Chemistry* **89,** 2457–2463 (2017).

93. Bertsch, A. & Renaud, P. in *Stereolithography: Materials, Processes, and Applications* 47–54 (2011). doi:10.1007/978-0-387-92904-0

94. Bertsch, A., Jézéquel, J. Y. & André, J. C. Study of the spatial resolution of a new 3D microfabrication process: the microstereophotolithography using a dynamic mask-generator technique. *Journal of Photochemistry and Photobiology A: Chemistry* **107,** 275–281 (1997).

95. RP Technologies. (2014). Available at: https://uni.edu/~rao/rt/major_tech.htm. (Accessed: 6th July 2014)

96. Zheng, X. Deotte J, Alonso MP, Farquar GR, Weisgraber TH, Gemberling S, Lee H, Fang N, Spadaccini CM. Design and optimization of a light-emitting diode projection micro-stereolithography three-dimensional manufacturing system. *Review of Scientific Instruments* **83,** (2012).

97. Macdonald, N. P. Cabot JM, Smejkal P, Guijt RM, Paull B, Breadmore MC, Comparing Microfluidic Performance of Three-Dimensional (3D) Printing Platforms. *Analytical Chemistry* **89,** 3858–3866 (2017).

98. Bae, C. J. & Halloran, J. W. Integrally cored ceramic mold fabricated by ceramic stereolithography *International Journal of Applied Ceramic Technology*. **8,** 1255–1262 (2011).

99. Corcione, C. E., Greco, A., Montagna, F., Licciulli, A. & Maffezzoli, A. Silica moulds built by stereolithography. *Journal of Materials Science* **40,** 4899–4904 (2005).

100. Kirihara, S. Additive manufacturing of ceramic components using laser scanning stereolithography. *Welding in the World* **60,** 697–702 (2016).

101. Hinczewski, C., Corbel, S. & Chartier, T. Ceramic suspensions suitable for stereolithography. *Journal of the European Ceramic Society* **18,** 583–590 (1998).

102. Griffith, M. L. & Halloran, J. W. Freeform Fabrication of Ceramics via Stereolithography. *Journal of the American Ceramic Society* **79,** 2601–2608 (2005).

103. Kotz, F, Arnold K, Bauer W, Schild D, Keller N, Sachsenheimer K, Nargang TM, Richter C, Helmer D, Rapp BE,. Three-dimensional printing of transparent fused silica glass. *Nature* **544,** 337–339 (2017).

104. Tumbleston, J. R. Shirvanyants, D., Ermoshkin, N. Janusziewicz, R., Johnson, A. R., Kelly, D., Chen, K., Pinschmidt, R., Rolland, J. P., Ermoshkin, A., Samulski, E. T., DeSimone, J. M.Continuous liquid interface production of 3D objects. *Science (80).* **347,** 1349–1352 (2015).

105. Janusziewicz, R., Tumbleston, J. R., Quintanilla, A. L., Mecham, S. J. & DeSimone, J. M. Layerless fabrication with continuous liquid interface production. *Proceedings of the National Academy of Sciences of the United States of America* **113,** 11703–11708 (2016).

106. Johnson, A. R. Caudill CL, Tumbleston JR, Bloomquist CJ, Moga KA, Ermoshkin A, Shirvanyants D, Mecham S, Luft JC, De Simone J M.. Single-step fabrication of computationally designed microneedles by continuous liquid interface production. *PLoS One* **11**(9)**,** (2016).

107. Bertsch, A. & Renaud, P. in *Three-Dimensional Microfabrication Using Two-Photon Polymerization* **2** 20–24 (2016). doi:10.1016/B978-0-323-35321-2/00002-9

108. Han, D., Lu, Z., Chester, S. A. & Lee, H. Micro 3D Printing of a Temperature-Responsive Hydrogel Using Projection Micro-Stereolithography. *Scientific Reports.* **8** 1963-1968 (2018).

109. Lee, H. & Fang, N. X. Micro 3D Printing Using a Digital Projector and its Application in the Study of Soft Materials Mechanics. *Journal of Visualized Experiments* **69** 4457-4460 (2012). doi:10.3791/4457

110. Sun, C. & Zhang, X. The influences of the material properties on ceramic micro-stereolithography. *Sensors Actuators, A Phys.* **101,** 364–370 (2002).

111. Wu, S., Serbin, J. & Gu, M. Two-photon polymerisation for three-dimensional micro-fabrication. *Journal of Photochemistry and Photobiology A: Chemistry* **181,** 1–11 (2006).

112. Doraiswamy, A. Jin, C., Narayan, R. J., Mageswaran, P., Mente, P., Modi, R., Auyeung, R., Chrisey, D. B., Ovsianikov, A., Chichkov, B. Two photon induced polymerization of organic-inorganic hybrid biomaterials for microstructured medical devices. *Acta Biomaterialia.* **2,** 267–275 (2006).

113. Kawata, S., Sun, H. B., Tanaka, T. & Takada, K. Finer features for functional microdevices. *Nature* **412,** 697–698 (2001).

114. Sun, H. B. Suwa T, Takada K, Zaccaria RP, Kim MS, Lee KS, Kawata S, Shape precompensation in two-photon laser nanowriting of photonic lattices. *Applied Physics Letters* **85,** 3708–3710 (2004).

115. Serbin, J. Egbert, A., Ostendorf, A., Chichkov, B. N., Houbertz, R., Domann, G., Schulz, J., Cronauer, C., Fröhlich, L., Popall, M. Femtosecond laser-induced two-photon polymerization of inorganic–organic hybrid materials for applications in photonics. *Optics Letters* **28,** 301 (2003).

116. Wu, S., Serbin, J. & Gu, M. Two-photon polymerisation for three-dimensional micro-fabrication. *Journal of Photochemistry and Photobiology A: Chemistry* **181,** 1–11 (2006).

117. Obata, K., El-Tamer, A., Koch, L., Hinze, U. & Chichkov, B. N. High-aspect 3D two-photon polymerization structuring with widened objective working range (WOW-2PP). *Light: Science & Applications* **2** e116 (2013).

118. Matheuse, F., Vanderheyden, Y., Vanmol, K., Van Erps, J., De Malsche, W., Ottevaere, H., Desmet, G. Possibilities of advanced 3D printing to produce chromatographic supports with 1-micron resolution. in *HPLC 2017* (2017).

119. Paull, B., Macdonald, N. P., Gupta, V. & Currivan, S. A. 12 Months Closer to 3D-Printed Columns. in *HPLC 2017* (2017).

120. Vanderlinden, K., Broeckhoven, K., Vanderheyden, Y. & Desmet, G. Effect of pre- and post-column band broadening on the performance of high-speed chromatography

columns under isocratic and gradient conditions. *Journal of Chromatography A* **1442,** 73–82 (2016).

121. Gritti, F. & Guiochon, G. Band broadening in fast gradient high-performance liquid chromatography: Application to the second generation of 4.6mm I.D. silica monolithic columns. *Journal of Chromatography A* **1238,** 77–90 (2012).

122. Gritti, F. & Guiochon, G. On the extra-column band-broadening contributions of modern, very high pressure liquid chromatographs using 2.1mm I.D. columns packed with sub-2μm particles. *Journal of Chromatography A* **1217,** 7677–7689 (2010).

123. Levenspiel, O. in *Tracer Technology - Modeling the Flow of Fluids,* E1-E7 5–7 (Springer Verlag, 2011).

124. Beisler, A. T., Schaefer, K. E. & Weber, S. G. Simple method for the quantitative examination of extra column band broadening in microchromatographic systems. *Journal of Chromatography A* **986,** 247–251 (2003).

125. Verstraeten, M., Liekens, A. & Desmet, G. Accurate determination of extra-column band broadening using peak summation. *Journal of Separation Science* **35,** 519–529 (2012).

126. Shirazi, S. F. S. Gharehkhani S, Mehrali M, Yarmand H, Metselaar HSC, Adib Kadri N, Abu Osman, NA, A review on powder-based additive manufacturing for tissue engineering: Selective laser sintering and inkjet 3D printing. *Science and Technology of Advanced Materials* **16,** 1878-1884 (2015).

127. Lee, J. M., Zhang, M. & Yeong, W. Y. Characterization and evaluation of 3D printed microfluidic chip for cell processing. *Microfluidics and Nanofluidics* **20,** 1–15 (2016).

128. Sherman, T. F. On connecting large vessels to small. The meaning of Murray's law. *The Journal of General Physiology* **78,** 431–453 (1981).

129. Fee, C., Nawada, S. & Dimartino, S. 3D printed porous media columns with fine control of column packing morphology. *Journal of Chromatography A* **1333,** 18–24 (2014).

130. Lottes, F., Arlt, W., Minceva, M. & Stenby, E. H. Hydrodynamic impact of particle shape in slurry packed liquid chromatography columns. *Journal of Chromatography A*

1216, 5687–5695 (2009).

131. Verzele, M., Dewaele, C. & Duquet, D. Observations and ideas on slurry packing of liquid chromatography columns. *Journal of Chromatography A* **391,** 111–118 (1987).

132. Keller, H. P., Ernl, F., Linder, H. R. & Frei, R. W. Dynamic Slurry-Packing Technique for Liquid Chromatography Columns. *Analytical Chemistry* **49,** 1958–1963 (1977).

133. Gritti, F. & Guiochon, G. The current revolution in column technology: How it began, where is it going? *Journal of Chromatography A* **1228,** 2–19 (2012).

134. Lee, B. H. & Lee, S. K. Effects of specific surface area and porosity on cube counting fractal dimension, lacunarity, configurational entropy, and permeability of model porous networks: Random packing simulations and NMR micro-imaging study. *Journal of Hydrology* **496,** 122–141 (2013).

135. Khirevich, S., Daneyko, A., Höltzel, A., Seidel-Morgenstern, A. & Tallarek, U. Statistical analysis of packed beds, the origin of short-range disorder, and its impact on eddy dispersion. *Journal of Chromatography A* **1217,** 4713–4722 (2010).

136. Ehlert, S., Rösler, T. & Tallarek, U. Packing density of slurry-packed capillaries at low aspect ratios. *Journal of Separation Science* **31,** 1719–1728 (2008).

137. Nawada, S., Dimartino, S. & Fee, C. The effects of bead overlap on chromatographic performance in 3D printed packed bed columns. April Edition, *International Labmate* (2014).

138. Rogers, B. A. Wu Z, Wei B, Zhang X, Cao X, Alabi O, Wirth MJ, Submicrometer Particles and Slip Flow in Liquid Chromatography. *Analytical Chemistry* **87,** 2520–2526 (2015).

139. Li, L., Yan, X., Yang, J. & Wang, Q. Numerical investigation on band-broadening characteristics of an ordered packed bed with novel particles. *Applied Energy* **185,** 2168–2180 (2017).

140. Yan, X. & Wang, Q. Numerical investigation into the effects of ordered particle packing and slip flow on the performance of chromatography. *Journal of Separation Science* **36,** 1524–1529 (2013).

141. Guiochon, G. The limits of the separation power of unidimensional column liquid chromatography.**1126** 6-49, *Journal of Chromatography A* (2006). doi:10.1016/j.chroma.2006.07.032

142. Kirkland, J. J., Truszkowski, F. A., Dilks, C. H. & Engel, G. S. Superficially porous silica microspheres for fast high-performance liquid chromatography of macromolecules. *Journal of Chromatography A* **890,** 3–13 (2000).

143. Kaczmarski, K. & Guiochon, G. Modeling of the mass-transfer kinetics in chromatographic columns packed with shell and pellicular particles. *Analytical Chemistry* **79,** 4648–4656 (2007).

144. Daneyko, A. Hlushkou D, Baranau V, Khirevich S, Seidel-Morgenstern A, Tallarek U, Computational investigation of longitudinal diffusion, eddy dispersion, and trans-particle mass transfer in bulk, random packings of core–shell particles with varied shell thickness and shell diffusion coefficient. *Journal of Chromatography A* **1407,** 139–156 (2015).

145. Nawada, S., Dimartino, S. & Fee, C. Dispersion behavior of 3D-printed columns with homogeneous microstructures comprising differing element shapes. *Chemical Engineerng Science* **164,** 90–98 (2017).

146. Vissers, J. P. C., Hoeben, M. A., Laven, J., Claessens, H. A. & Cramers, C. A. Hydrodynamic aspects of slurry packing processes in microcolumn liquid chromatography. *Journal of Chromatography A* **883,** 11–25 (2000).

147. Zimina, T., Smith, R. M., Highfield, J. C., Myers, P. & King, B. W. Study of the flow development during the slurry packing of microcolumns for liquid chromatography. in *Journal of Chromatography A* **728**, 33-35 (1996). doi:10.1016/0021-9673(95)01026-2

148. Eriksen, K., Toussaint, F., Maloy, J. & Semih, T. Optical Analyses of Flow in and Transformation of Deformable Porous Media. in *EGU General Assembly* (2014).

149. Colón, L. A., Maloney, T. D. & Fermier, A. M. Packing columns for capillary electrochromatography. *Journal of Chromatography A* **887,** 43–53 (2000).

150. Farrell, N. J. C. & Healy, D. Anisotropic pore fabrics in faulted porous sandstones. *Journal of Structural Geology* **104,** 125–141 (2017).

151. Farrell, N. J. C., Healy, D. & Taylor, C. W. Anisotropy of permeability in faulted porous sandstones. *Journal of Structural Geology* **63,** 50–67 (2014).

152. Schure, M. R. & Maier, R. S. How does column packing microstructure affect column efficiency in liquid chromatography? *Journal of Chromatography A* **1126,** 58–69 (2006).

153. Rumble, J. R. CRC Handbook of Chemistry and Physics, 98th Edition. *CRC Handbook of Chemistry and Physics, 98th Edition* (2017).

154. Stute, B., Krupp, V. & Von Lieres, E. Performance of iterative equation solvers for mass transfer problems in three-dimensional sphere packings in COMSOL. *Simulation Modelling Practice and Theory* **33,** 115–131 (2013).

155. Pursch, M., Wegener, A. & Buckenmaier, S. Evaluation of active solvent modulation to enhance two-dimensional liquid chromatography for target analysis in polymeric matrices. *Journal of Chromatography A* **1562,** 78–86 (2018).

156. Shalliker, R. A., Catchpoole, H. J., Dennis, G. R. & Guiochon, G. Visualising viscous fingering in chromatography columns: High viscosity solute plug. *Journal of Chromatography A* **1142,** 48–55 (2007).

157. Catchpoole, H. J., Andrew Shalliker, R., Dennis, G. R. & Guiochon, G. Visualising the onset of viscous fingering in chromatography columns. *Journal of Chromatography A* **1117,** 137–145 (2006).

158. Guiochon, G., Shirazi, D. & Felinger, A. *Fundamentals of Preparative and Nonlinear Chromatography*. 223-225 (1994).

159. Garcia, X., Akanji, L. T., Blunt, M. J., Matthai, S. K. & Latham, J. P. Numerical study of the effects of particle shape and polydispersity on permeability. *Phys. Rev. E - Stat. Nonlinear, Soft Matter Phys.* **80,** (2009).

160. Yazdchi, K., Srivastava, S. & Luding, S. Microstructural effects on the permeability of periodic fibrous porous media. *International Journal of Multiphase Flow* **37,** 956–966 (2011).

161. Billi, A., Salvini, F. & Storti, F. The damage zone-fault core transition in carbonate rocks: Implications for fault growth, structure and permeability. *Journal of Structural*

Geology. **25,** 1779–1794 (2003).

162. Nawada, S., Dimartino, S. & Fee, C. Dispersion behavior of 3D-printed columns with homogeneous microstructures comprising differing element shapes. *Chemical Engineering Science*. **164,** 90–98 (2017).

163. Meusnier, J. Mémoire sur la courbure des surfaces. in *Mém. des savans étrangers 10* **10,** 477–510 (1776).

164. Schwartz, H. A. Fortsetzung der Untersuchung über Minimalflächen. *Monatsbericht, K. Akad. Wiss.* 855–856 (1866).

165. Schwarz, H. A. in *Gesammelte Mathematische Abhandlungen: Erster Band* 1–5 (Springer Berlin Heidelberg, 1890). doi:10.1007/978-3-642-50665-9_1

166. Neovius, E. . in *Akademische Abhandlungen, 1* (1883).

167. Schoen, A. *Three dimensional Euclidean space partitioned into interpenetrating labyrinths by infinite periodic minimal surfaces without self intersections*. (1970).

168. Almsherqi, Z., Hyde, S., Ramachandran, M. & Deng, Y. Cubic membranes: a structure-based design for DNA uptake. *Journal of the Royal Society Interface* **5,** 1023 LP-1029 (2008).

169. Almsherqi, Z., Margadant, F. & Deng, Y. A look through 'lens' cubic mitochondria. *Interface Focus* **2,** 539 LP-545 (2012).

170. Hsueh, H.-Y., Yao, C.-T. & Ho, R.-M. Well-ordered nanohybrids and nanoporous materials from gyroid block copolymer templates. *Chemical Society Reviews* **44,** 1974–2018 (2015).

171. Hsueh, H.-Y. Huang YC, Ho RM, Lai CH, Makida T, Hasegawa H, Nanoporous Gyroid Nickel from Block Copolymer Templates via Electroless Plating. *Advanced Materials*. **23,** 3041–3046 (2011).

172. Cheng, C.-F. Hsueh HY, Lai CH, Pan CJ, Hwang BJ, Hu CC, Ho RM, Nanoporous gyroid platinum with high catalytic activity from block copolymer templates via electroless plating. *NPG Asia Mater* **7,** e170 (2015).

173. Saranathan, V. Osuji CO, Mochrie SGJ, Noh H, Narayanan S, Sandy AD, Eric R,

Prum, RO. Structure, function, and self-assembly of single network gyroid (I4132) photonic crystals in butterfly wing scales. *Proceedings of the National Academy of Sciences of the United States of America* **107,** 11676–11681 (2010).

174. Singer A, Boucheron L, Dietze SH, Jensen KE, Vine D, McNulty ID, Eric R, Prum RO, Mochrie SGJ, Shpyrko OG Domain morphology, boundaries, and topological defects in biophotonic gyroid nanostructures of butterfly wing scales. *Science Advances* **2,** (2016).

175. Michielsen, K., De Raedt, H. & Stavenga, D. G. Reflectivity of the gyroid biophotonic crystals in the ventral wing scales of the Green Hairstreak butterfly, Callophrys rubi *Journal of the Royal Society Interface***,** 765 LP-771 (2010).

176. Kapfer, S. C., Hyde, S. T., Mecke, K., Arns, C. H. & Schröder-Turk, G. E. Minimal surface scaffold designs for tissue engineering. *Biomaterials* **32,** 6875–6882 (2011).

177. Guest, J. K. & Prévost, J. H. Design of maximum permeability material structures. *Computer Methods in Applied Mechanics and Engineering*. **196,** 1006–1017 (2007).

178. Jung, Y., Chu, K. T. & Torquato, S. A Variational Level Set Approach for Surface Area Minimization of Triply-periodic Surfaces. *Journal of Computional Physics.* **223,** 711–730 (2007).

179. Jung, Y. & Torquato, S. Fluid permeabilities of triply periodic minimal surfaces. *Phys. Rev. E - Stat. Nonlinear, Soft Matter Phys.***72**(5) (2005). doi:10.1103/PhysRevE.72.056319

180. Abueidda, D. W. Abu Al-Rub RK, Dalaq AS, Younes HA, Al Ghaferi AA, Shah, TK. Electrical conductivity of 3D periodic architectured interpenetrating phase composites with carbon nanostructured-epoxy reinforcements. *Composites Science and Technology*. **118,** 127–134 (2015).

181. Dalaq, A. S., Abueidda, D. W. & Abu Al-Rub, R. K. Mechanical properties of 3D printed interpenetrating phase composites with novel architectured 3D solid-sheet reinforcements. *Composites Part A: Applied Science and Manufacturing* **84,** 266–280 (2016).

182. Qin, Z., Jung, G. S., Kang, M. J. & Buehler, M. J. The mechanics and design of a lightweight three-dimensional graphene assembly. *Science Advances.* **3,** e1601536 (2017).

183. Yoo, D. J. Porous scaffold design using the distance field and triply periodic minimal surface models. *Biomaterials* **32,** 7741–7754 (2011).

184. Blanquer, S. B. G. Werner M, Hannula M, Sharifi S, Lajoinie GPR, Eglin D, Hyttinen J, Poot AA, Grijpma DW, Surface curvature in triply-periodic minimal surface architectures as a distinct design parameter in preparing advanced tissue engineering scaffolds. *Biofabrication* **9**(2)**,** (2017).

185. Femmer, T., Kuehne, A. J. C., Torres-Rendon, J., Walther, A. & Wessling, M. Print your membrane: Rapid prototyping of complex 3D-PDMS membranes via a sacrificial resist. *Journal of Membrane Sciences.* **478,** 12–18 (2015).

186. Femmer, T., Kuehne, A. J. C. & Wessling, M. Estimation of the structure dependent performance of 3-D rapid prototyped membranes. *Chemical Engineering Journal.* **273,** 438–445 (2015).

187. Dolamore, F., Fee, C. & Dimartino, S. Modelling ordered packed beds of spheres: The importance of bed orientation and the influence of tortuosity on dispersion. *Journal of Chromatography A* **1532,** 150–160 (2018).

188. Dolamore, F. In Silico analysis of flow and dispersion in ordered porous media. (PhD Thesis: University of Canterbury, 2017).

189. Gandy, P. J. F., Bardhan, S., Mackay, A. L. & Klinowski, J. Nodal surface approximations to the P, G, D and I-WP triply periodic minimal surfaces. *Chemical Physics Letters.* **336,** 187–195 (2001).

190. von Schnering, H. G. & Nesper, R. Nodal surfaces of Fourier series: Fundamental invariants of structured matter. *Zeitschrift für Physik B Condensed Matter* **83,** 407–412 (1991).

191. Quinn, H. M., Quinn, H. M., Quinn & M., H. A Reconciliation of Packed Column Permeability Data: Column Permeability as a Function of Particle Porosity *Journal of Materials Science.* **2014,** 1–22 (2014).

192. Hahn, R. & Jungbauer, A. Peak Broadening in Protein Chromatography with Monoliths at Very Fast Separations. *Analytical Chemistry* **72,** 4853–4858 (2000).

193. Vervoort, N., Gzil, P., Baron, G. V. & Desmet, G. A correlation for the pressure drop in monolithic silica columns. *Analytical Chemistry* **75**(4) 843-850 (2003). doi:10.1021/ac0262199

194. Broeckhoven, K. & Desmet, G. Considerations for the use of ultra-high pressures in liquid chromatography for 2.1 mm inner diameter columns. *Journal of Chromatography A* **1523,** 183–192 (2017).

195. Instructables. Ember Printer: Using Pattern Mode for Finer Details. (2017). Available at: https://www.instructables.com/id/Ember-Printer-Using-Pattern-Mode-for-Finer-Details/. (Accessed: 17th July 2017)

196. Ilachinski, A. *Cellular Automata: A Discrete Universe*. *Cellular Automata: A Discrete Universe* 10-15 (2001). doi:10.1142/4702

197. Marchal, P. John von Neumann: The founding father of artificial life. *Artificial Life* **4,** 229–235 (1998).

198. Wolfram, S. Statistical mechanics of cellular automata. *Reviews of Modern Physics* **55,** 601–644 (1983).

199. Ermentrout, G. B. & Edelstein-Keshet, L. Cellular automata approaches to biological modeling. *Journal of Theoretical Biology***160,** 97–133 (1993).

200. Materi, W. & Wishart, D. S. Computational systems biology in drug discovery and development: methods and applications. *Drug Discovery Today* **12,** 295–303 (2007).

201. Nandi, S., Kar, B. K. & Chaudhuri, P. P. Theory and Applications of Cellular Automata in Cryptography. *IEEE Transactions on Computers* **43,** 1346–1357 (1994).

202. Wolfram, S. Cryptography with Cellular Automata. in *Lecture Notes in Computer Science (including subseries Lecture Notes in Artificial Intelligence and Lecture Notes in Bioinformatics)* **218 LNCS,** 429–432 (1986).

203. Packard, N. H. & Wolfram, S. Two-dimensional cellular automata. *Journal of Statistical Physics.* **38,** 901–946 (1985).

204. Cook, M. Universality in Elementary Cellular Automata. *Complex Systems*. **15,** 1–40 (2004).

Appendix A. Confocal Images of Element Shapes

Figures A- i-v show confocal images of the tested element shapes at a slice depth of z = 170 µm.

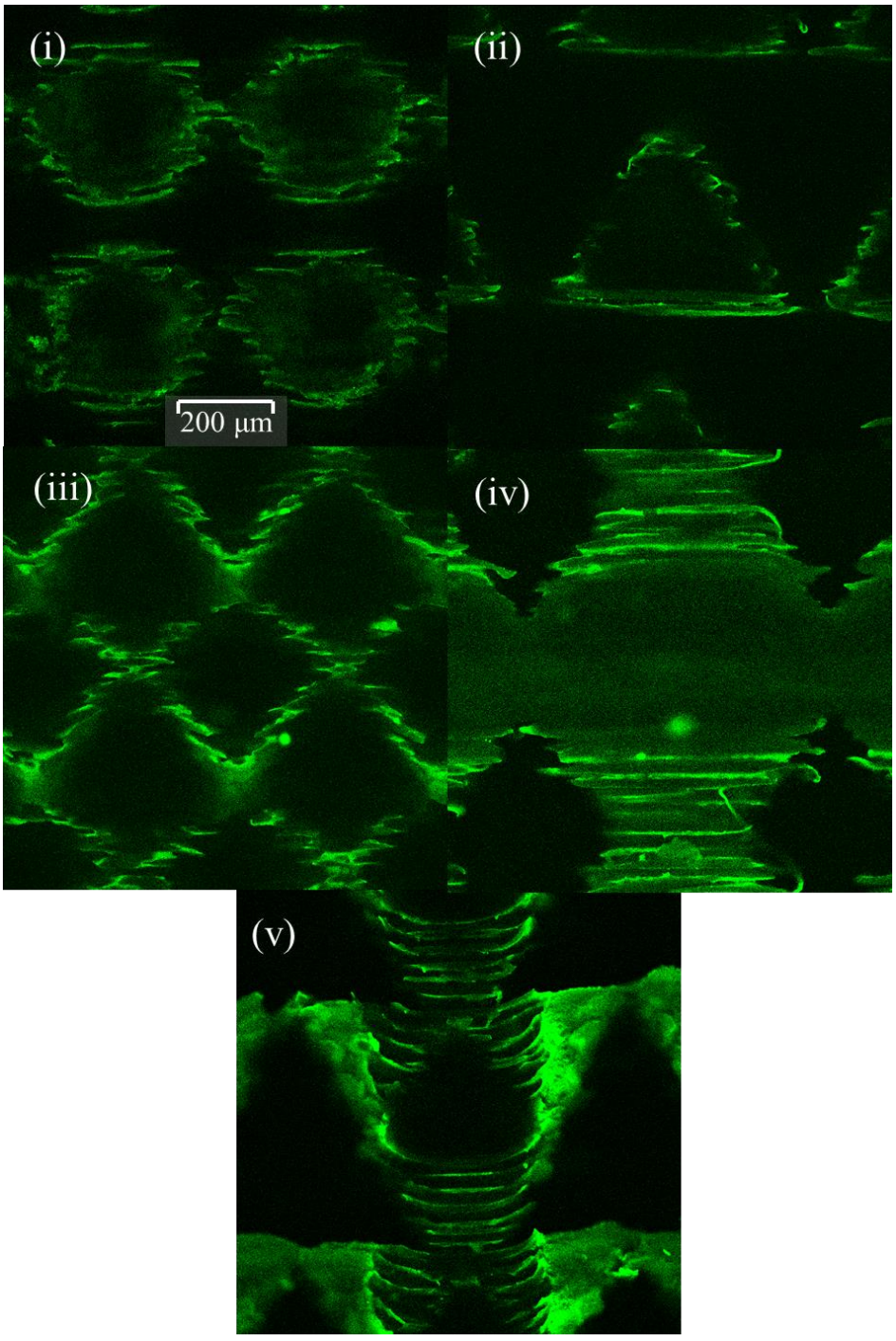

Fig A: Confocal image of tested particle shapes, printed on an x-y alignment at a slice depth of 170 µm with 10.0 x 0.40 objective (i) Spheres, (ii) Tetrahedra, (iii) Octahedra (iv) Triangular Bipyramid and (v) Stella Octangula. The scale bar shown in (a) applies to all geometries

Appendix B. CAD Design of Gyroid Columns using Wolfram Mathematica and Solidworks 2012

Curved TPMS structures can be very computationally challenging to design on a large-scale. This section of the appendix is a step-by-step manual on creating full TPMS columns with column walls and fittings in addition the porous TPMS structures using methods that can be handled by a desktop PC (Intel i7 4790 Processor in this case). The working example used here is of the Schoen Gyroid but this can be substituted for the other TPMS equations shown in Eq 5.1. First, the parametric equations are used to create a 3D-structure in Wolfram Mathematica 7.0 (described in Appendix 2.1) and the resulting 3D-structure is imported into Solidworks 2012, patterned and assembled with column casings (Appendix 2.2). It is worth noting that several aspects of the parametric equations described in Appendix 2.2 might be updated in later versions of Solidworks. Nevertheless, the basic method described here can be used to create full TPMS columns.

B.1. Mathematica

B.1.1 RegionPlot Function

In Fig B-1, we plot the most basic form of the gyroid surface: The network gyroid (one flow channel) with a void fraction of $\varepsilon = 0.5$.

$$\sin(x)\cdot\cos(y)+\sin(y)\cdot\cos(z)+\sin(z)\cdot\cos(z) > t$$

where $t = 0$.

```
In[404]:= networkgyroid = RegionPlot3D[(Sin[x] * Cos[y]) + (Sin[y] * Cos[z]) + (Sin[z] * Cos[x]) > 0,
          {x, -Pi, Pi}, {y, -Pi, Pi}, {z, -Pi, Pi}, PlotPoints → 8]
```

Out[404]=

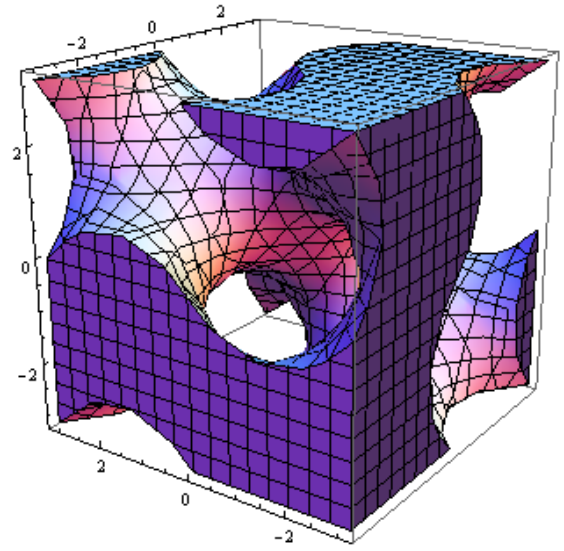

Fig B-1: RegionPlot3D of a network gyroid unitbox with G = 0

- Use name (in this case 'networkgyroid') to label the geometry
- Set plot range in x,y and z direction. A range of {-π, π} should be sufficient for most gyroid related geometries. However, some might require a range of {-2π, 2π}.
- Set surface resolution using the 'PlotPoints' function. Trade-off between surface finish and file size of the resulting .stl file
- Press Shift + Enter to produce the 3D plot.

To produce what is known as a sheet gyroid (i.e. a surface dividing the volume into two separate, interwoven flow units), the parametric equation can simply be modified to the following form where *t* is the wall thickness:

$$\left|\sin(x)\cdot\cos(y)+\sin(y)\cdot\cos(z)+\sin(z)\cdot\cos(z)\right|>t$$

```
In[394]:= sheetgyroid =
           RegionPlot3D[Abs[(Sin[x] * Cos[y]) + (Sin[y] * Cos[z]) + (Sin[z] * Cos[x])] < 0.5,
            {x, -Pi, Pi}, {y, -Pi, Pi}, {z, -Pi, Pi}, Mesh → None, Axes → None,
            PlotPoints → 20, Boxed → False]
```

Out[394]=

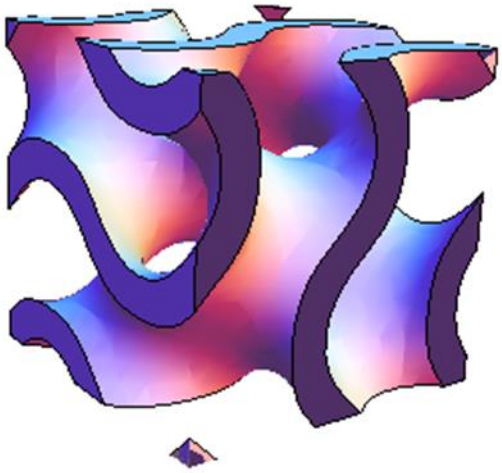

Fig B-2: Sheet gyroid with *t* = 0.5

B.1.2 Exporting the .stl file

- Specify the file location, name and format (.stl in this case) in inverted commas.
- Press Shift + Enter to create the .stl file.
- Verify that the resulting .stl file is less than 1 MB in size so that it can be recognized and processed by Solidworks. The number of PlotPoints can be reduced to ensure that the file remains under 1 MB.

```
In[388]:= Export["\\\\engcad4.canterbury.ac.nz\\shn26$\\My Desktop\\CAD Manual\\gyrbox.stl",
           networkgyroid]
Out[388]= \\engcad4.canterbury.ac.nz\shn26$\My Desktop\CAD Manual\gyrbox.stl
```

Fig B-3: The export function

B.2. Solidworks

B.2.1 Importing .stl Files

Open Solidworks, click File → Open. Choose .stl as the format when importing the file created on mathematica.

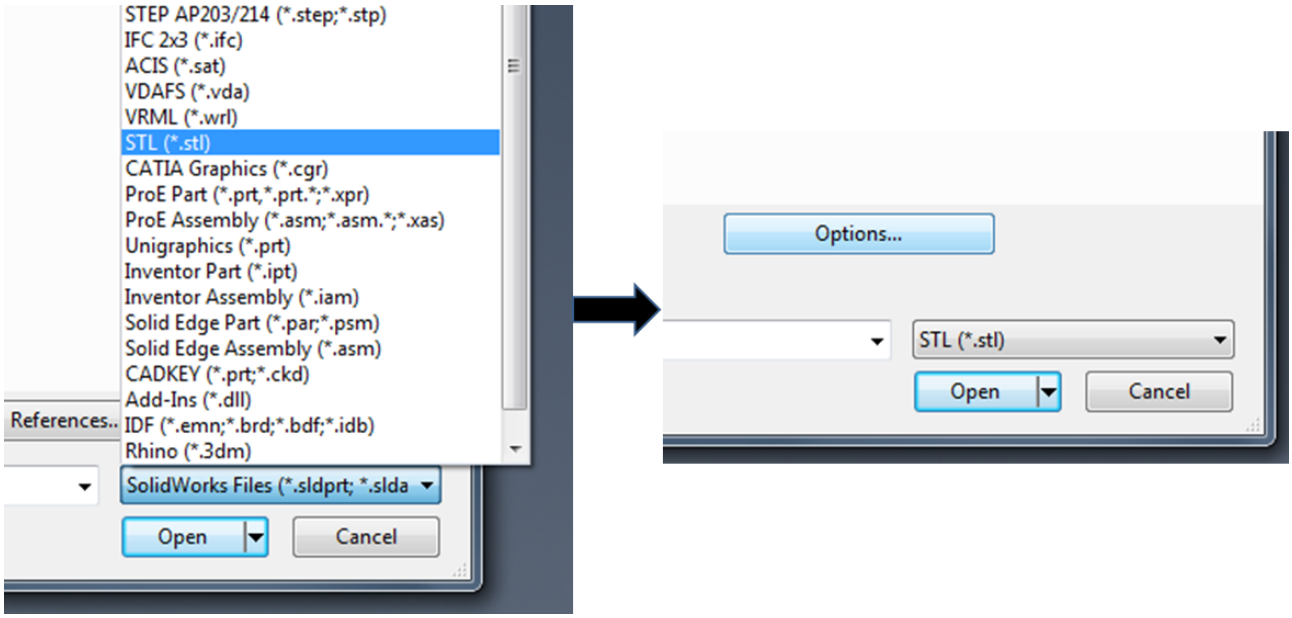

Fig B-4: .stl file import

In .stl file options, choose 'Solid Body' and in this case, millimetres as units.

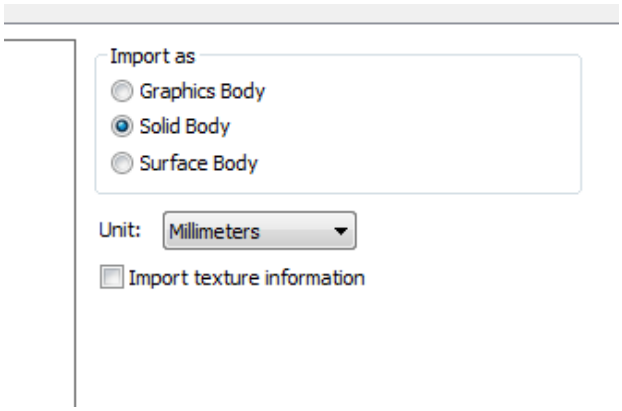

Fig B-5: Import options

Stl File Repair

At lower resolutions, Solidworks may show the following errors when importing the file:

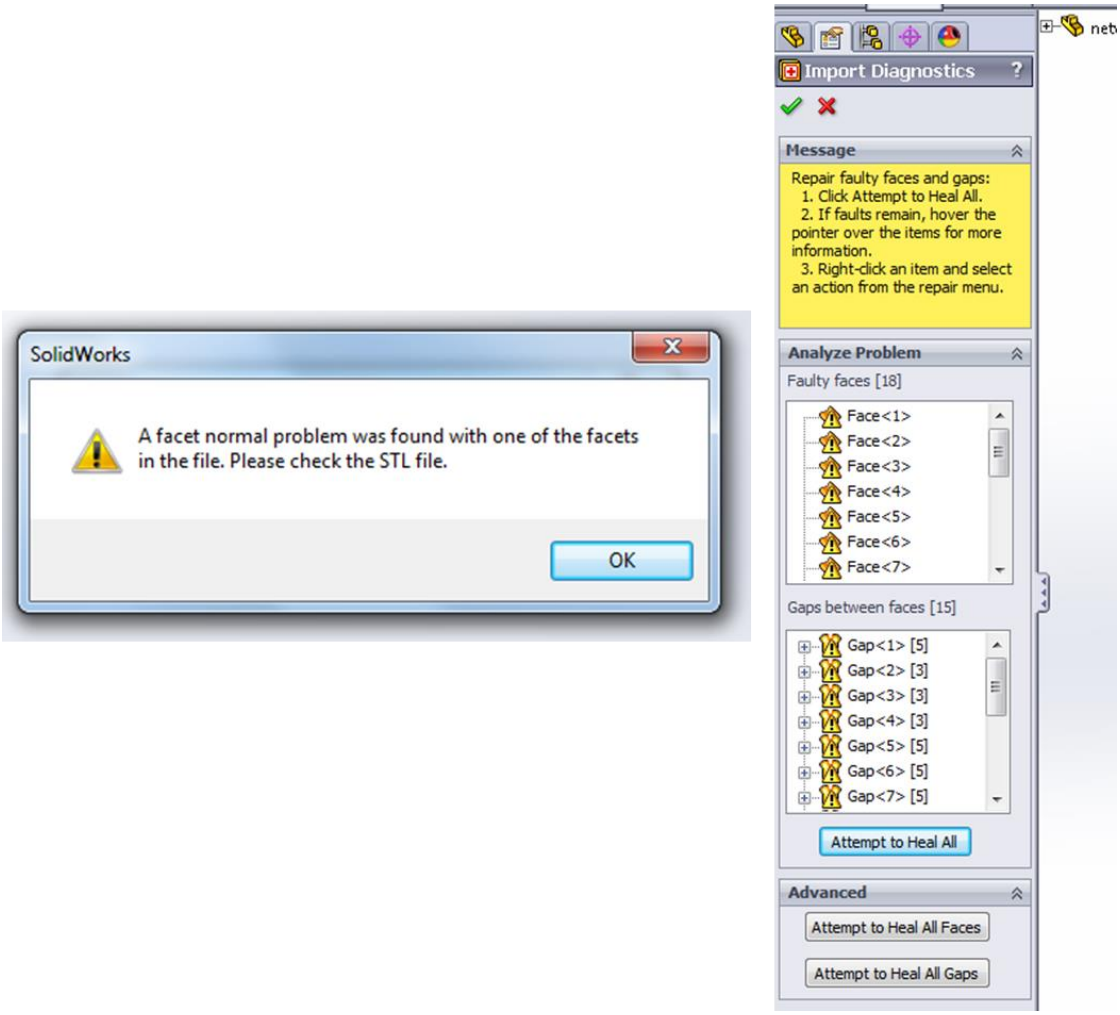

Fig B-6: .stl file import errors

This happens when the .stl file is poorly defined and contains either overlapping or underlapping triangles. If the 'Attempt to heal all' fails, it might be necessary to use a stl repair software. The following cloud based software can be used for smaller stl files:

https://netfabb.azurewebsites.net/

B.2.2 Creating a Layer Part

The first step to creating a full column after creating an error-free .stl file is to design a circular layer of the gyroid structure that is one unitbox high as shown in Fig B-7. We first re-scale the unitbox, pattern it in the x and y direction, then create a circular cross section. This

is the most important (and time consuming) component piece of the full column assembly that we will later design.

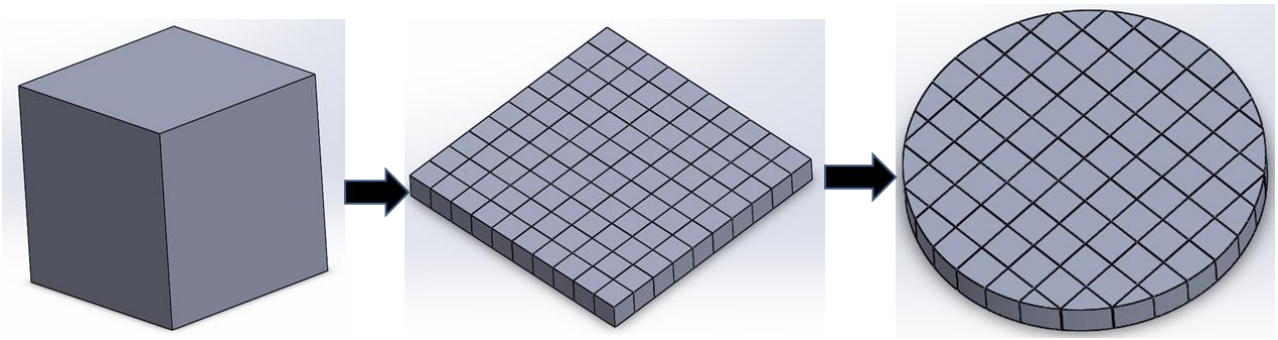

Fig B-7: Designing a layer part

Re-Scaling

The unitbox created on mathematica will be 2π x 2π x 2π mm in size if the chosen PlotRange was $\{-\pi, \pi\}$ in the x, y and z direction. It is possible to scale this object to our desired size, by using the scale function (Insert → Features → Scale).

In the case of gyroids and other triply periodic minimal surfaces, it is more convenient to use the 'Scale about the Origin' option as shown in Fig B-8. In the case of Fig B-1 (i.e. network gyroid with $G = 0$), the channel size is half the size of the unitbox itself. The target dimension to achieve 0.250 mm channels is to create a box with dimensions of 0.5 x 0.5 x 0.5 mm.

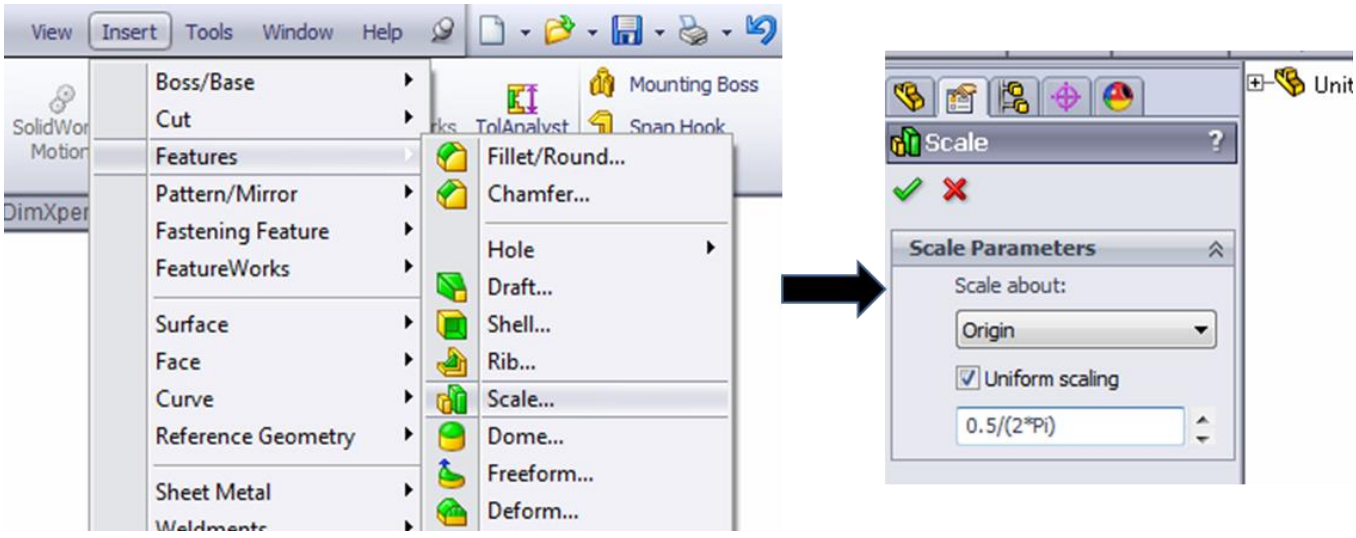

Fig B-8: Scale function

To save the re-scale, it is necessary to save the file as a .sldprt file, the default format on Solidworks.

B.2.3 Dimensions and Equations

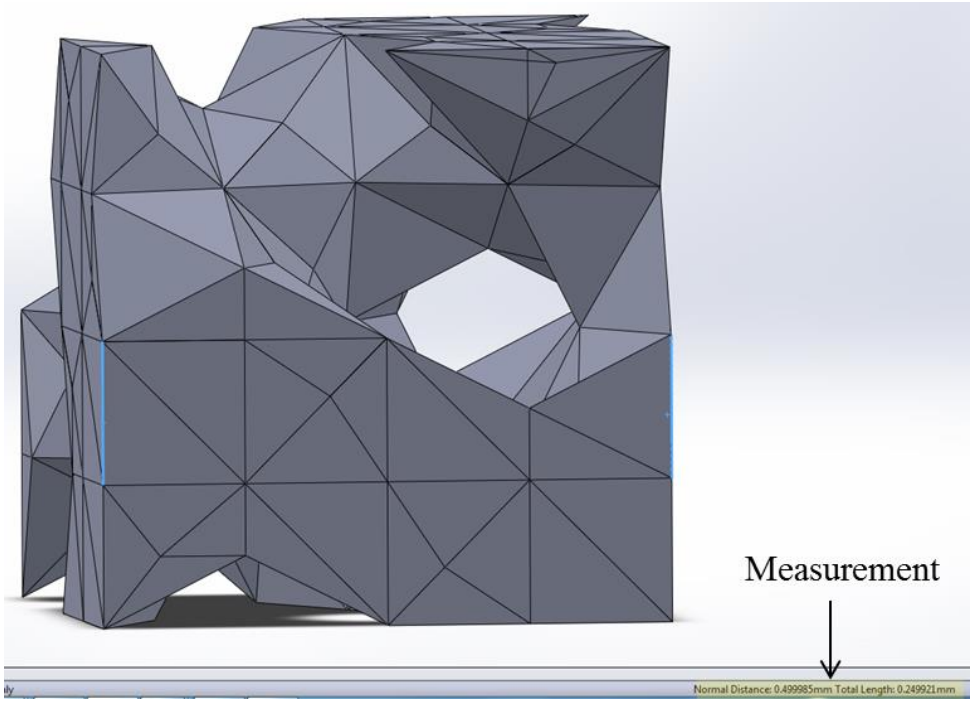

Fig B-9: Measurement of two parallel lines, marked in light blue

To verify that the unitbox is of the desired dimensions, hold Ctrl and click on two parallel lines or surfaces. The normal distance is shown on the bottom-right corner of the window. If the lines or surfaces are not completely parallel, go to Tools → Measure to calculate the distance between the two centerpoints of the lines or surfaces. The ‘Measure’ tool can also be used to calculate the surface areas of the component triangles.

In addition to simply measuring the dimensions of the gyroid, this measurement can also be used to govern other parameters in the column design using the ‘Equations’ function (Tools

→ Equations). In Fig B-10, we set up a measurement '*l*', that is the size of the unitbox:

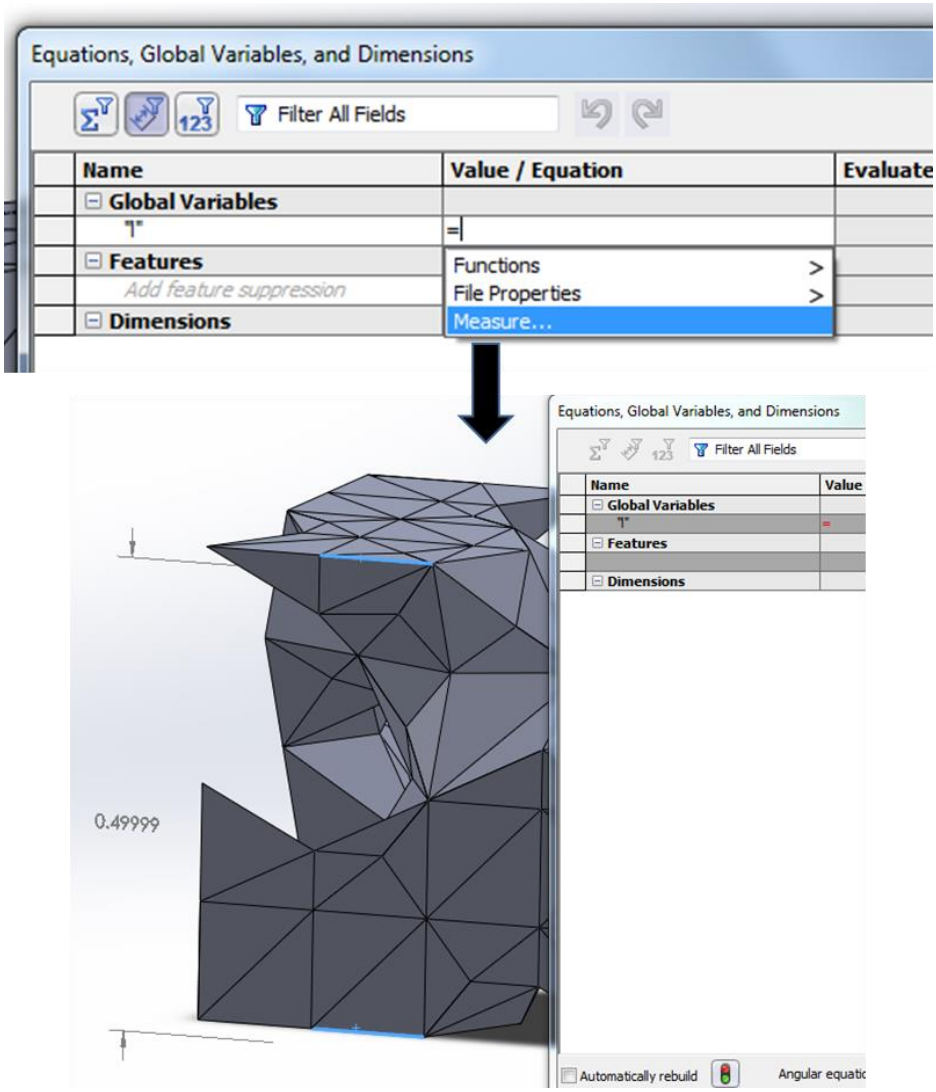

Fig B-10: Equation function with measurement of unitbox

By referring to this variable in the future, we eliminate the potential errors that could occur due to the fact that the unitbox is in this case 0.49999 mm rather than the intended 0.50000 mm in length. It is also possible to define other variables, such as the column's internal radius, 'ColumnRadius' and the number of unitboxes necessary to create a layer, '*p*':

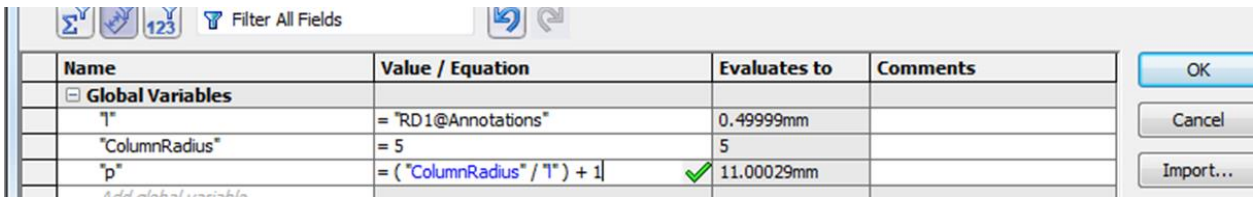

Fig B-11: Defining two new variables, ColumnRadius and p

B.2.4 X-Linear Pattern

To create a linear pattern of the unitbox, we first need to draw the sketches that the body will be patterned along. Right-click on the 'Top Plane' to first show, then take a normal view of the top plane, then click 'Sketch' to draw the pattern lines.

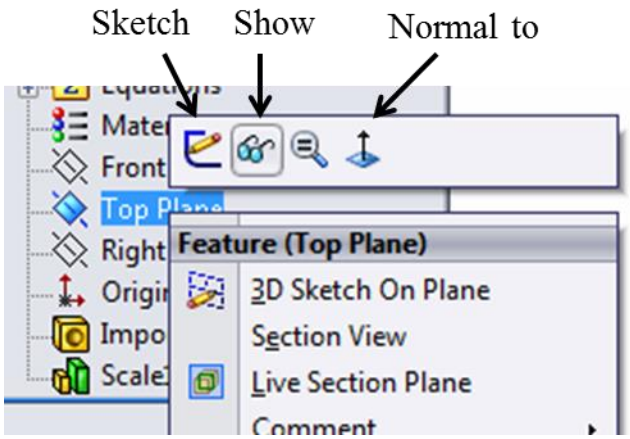

Fig B-12: Plane options

Draw two lines, the x and y direction from the origin to the outer edges of the unitbox.

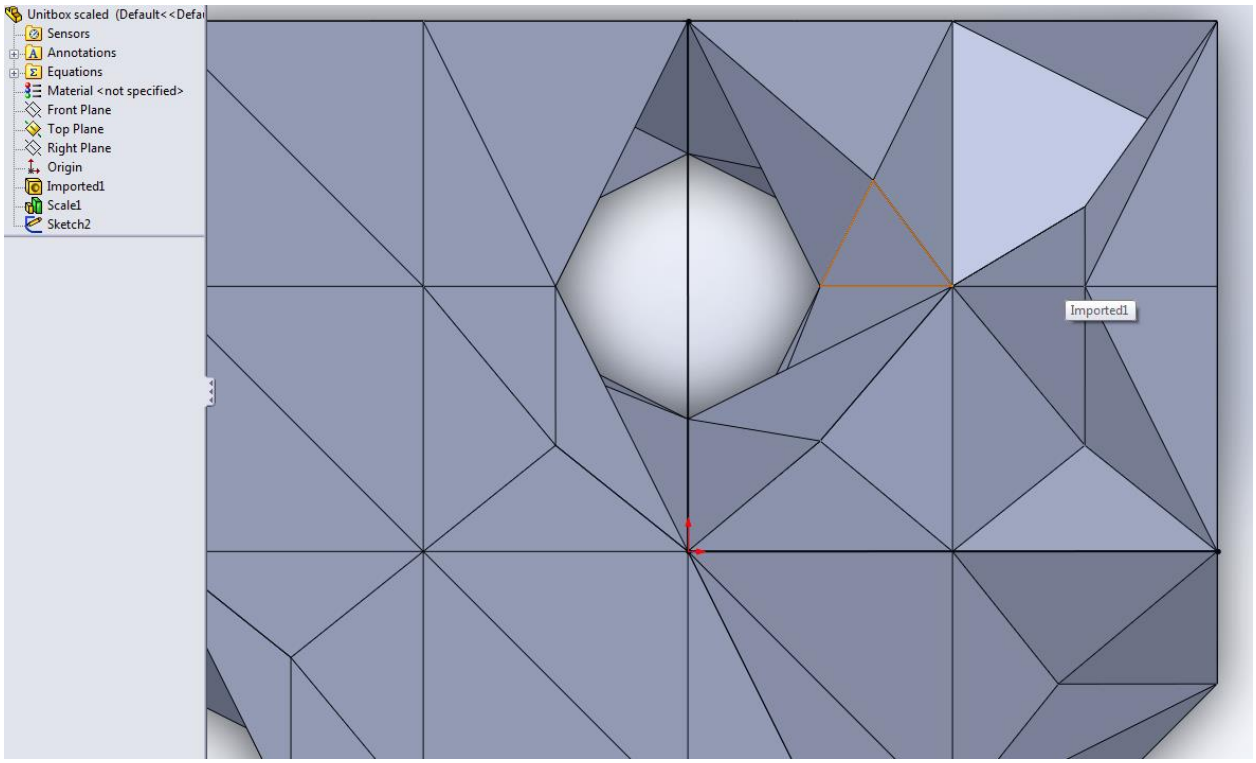

Fig B-13: Sketch of pattern lines

After drawing the two lines, exit sketch (Top left button in 'Sketch' mode) and create another sketch on the top plane. On this sketch, draw a circle with the origin as its center and an

arbitrary radius. Click on, ‘Smart Dimensions’ (top left, next to ‘exit sketch’) and click on the circle. Define the diameter of the circle as “ColumnRadius”*2 and exit sketch.

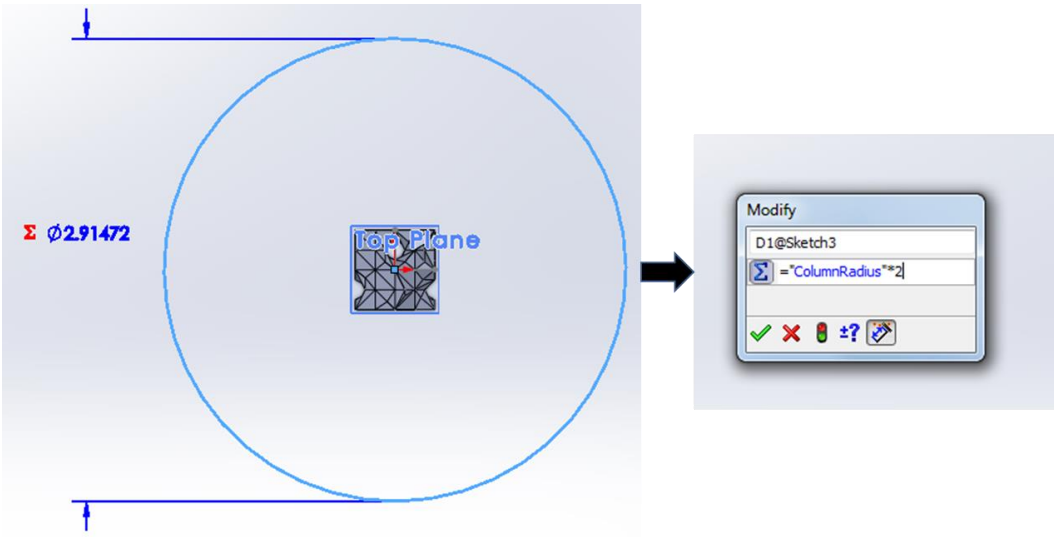

Fig B-14: Sketch of the column inner circle

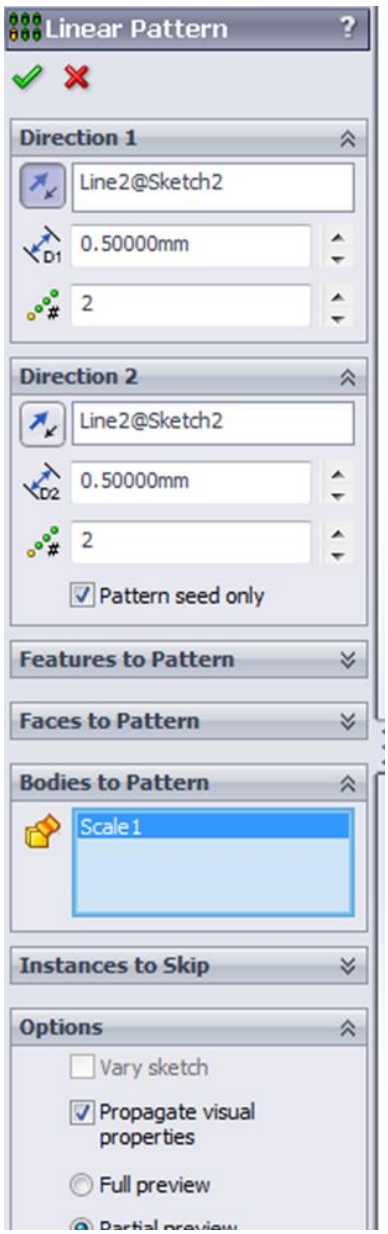

Fig B-1: Linear pattern options

To create the linear pattern, click Insert → Pattern/Mirror → Linear Pattern. Choose one of the lines sketched for patterning in the Direction 1 box and choose the same line on the Direction 2 box. However, ensure that the patterns run in opposite directions to each other by clicking on the 'reverse direction' button. Set approximate values for D1 and D2 spacing (0.5 mm in our case) and set number of instances to 2 in both directions. Then tick the 'Pattern seed only' option.

In 'Bodies to Pattern', choose the unitbox and create linear pattern (green tick, top-left in Fig B-16). The exact spacing and number of instances can be set on the equations pane.

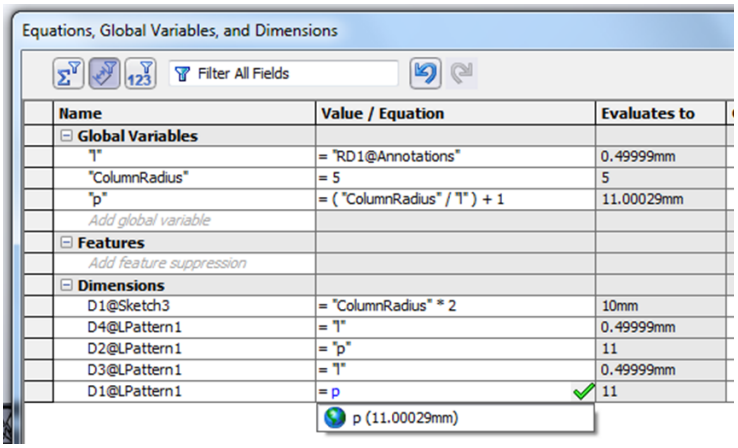

Fig B-15: Linear pattern dimensions

B.2.5 Y-Linear Pattern

Create a second linear pattern perpendicular to the first, with the only differences being the pattern lines and choosing every single body created in the x-linear pattern in 'Bodies to Pattern'. This step can be time consuming and computationally demanding, with either the program or the computer potentially crashing. After creating a second copy in either direction as in Fig B-16, it is often worth noting the computation times that were necessary to build the part so far. This can be done using Tools → Feature Statistics:

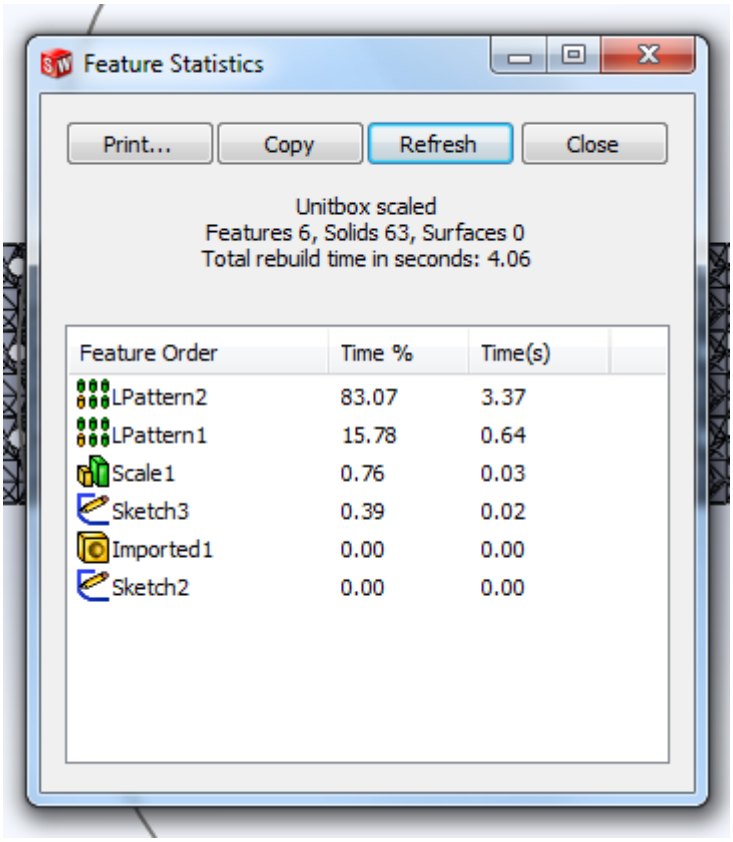

Fig B-17: Feature statistics

We can estimate that if the program takes 3.37 seconds to create two new strips in 'LPattern 2', creating 20 new stripes would take roughly 34 seconds. The geometry that we are using in this case is a simpler and computationally less demanding version of a gyroid. This step for other, more complex geometries may take up to several hours.

If either the geometry is too complex or the number of patterning instances is too high, the program might crash altogether. In these cases, instead of creating one pattern feature with all the bodies created in the x-linear pattern, it might be necessary to use several linear pattern features as shown in Fig B-18. The method of setting the number of instances to 2 in the linear pattern options (Fig B-16) and then increasing the number on the equations page is especially important here as practice has shown that this significantly reduces the computational load on the program. Due to the likelihood of the program crashing and the processing times involved, it is also especially important to regularly save the .sldprt file.

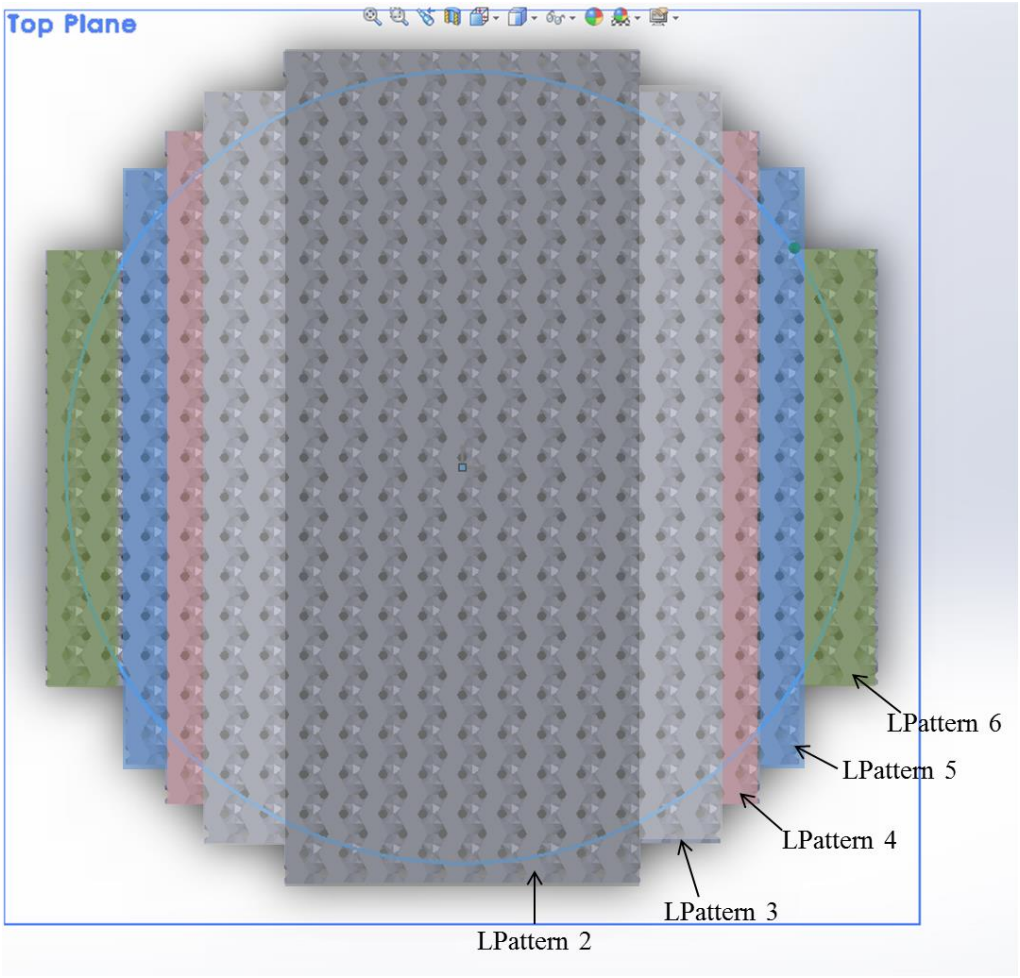

Fig B-18: Y-Linear pattern

B.2.6 Circular Cut Extrude

After patterning the geometry in both x and y directions, we can now trim the layer to a circular cross section. To do this, click on the column inner circle sketch (Fig B-14) and click Insert → Cut → Extrude. In the options for the extrude cut (Fig B-19), select 'Through All' instead of the default 'Blind' option for both direction 1 and 2. Also select the 'Thin Feature' option to only cut the outer ring (with the thickness of 10 mm in this case) surrounding the column circle sketch. In the feature scope box, select 'All Bodies' to cut through and press OK.

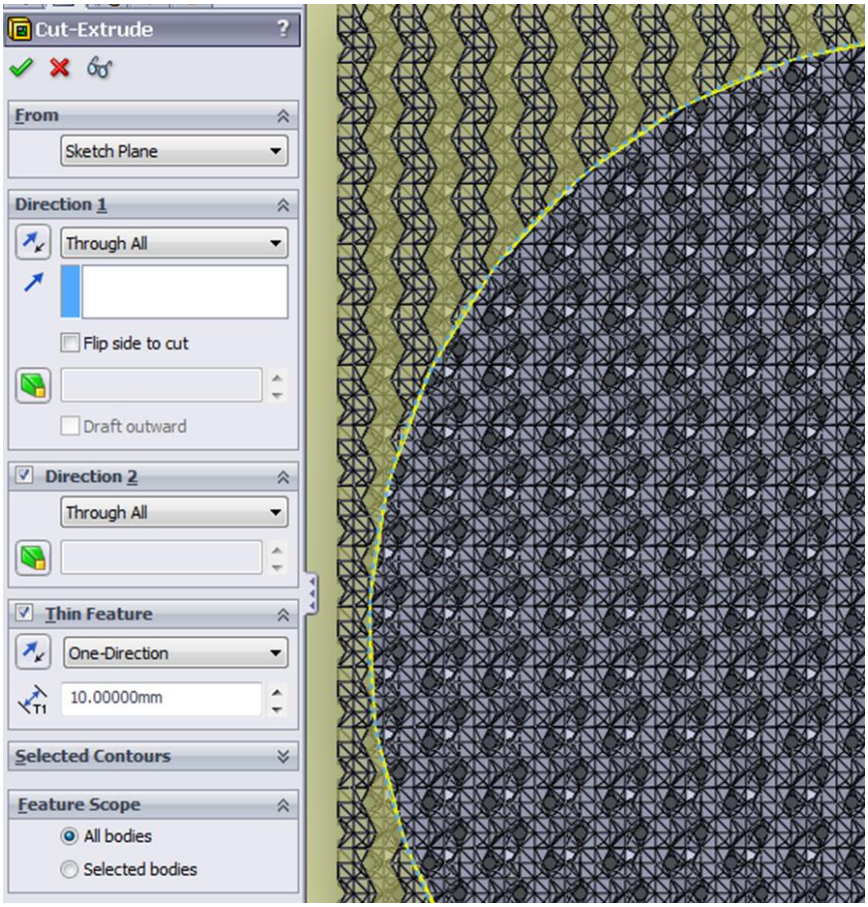

Fig B-19: Cut-extrude options

For more computationally demanding geometries, the resulting part may not always have a perfectly circular cross section as seen in Fig B-20 a. In this case, we can modify the cut-extrude feature (right click on 'Cut-Extrude-Thin1' and select 'Edit Feature').

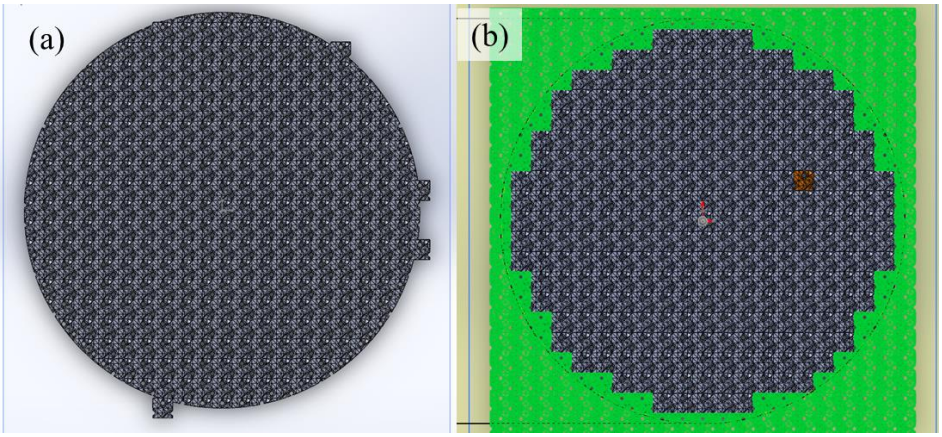

Fig B-20: (a) Cut-extrude with overhanging parts and (b) Cut-extrude with manually selected bodies, marked in green.

In the 'Feature Scope' box, we can choose 'Selected Bodies' and manually select the bodies that will be affected by the cut, as shown in Fig B-20 b. This will reduce the computational

load on the program by processing the relevant bodies (shown in green) as opposed to every body in the layer.

B.2.7 Creating a Column Casing

In this section, we design the column walls as well as a simple inlet and outlet fitting for the gyroid column. This will be designed on a new solidworks part document. On the top plane, sketch two concentric circles with the radius of the inner circle being equal to column inner circle in the gyroid layer part (10 mm in this case). Here, we build a column wall with a thickness of 2 mm:

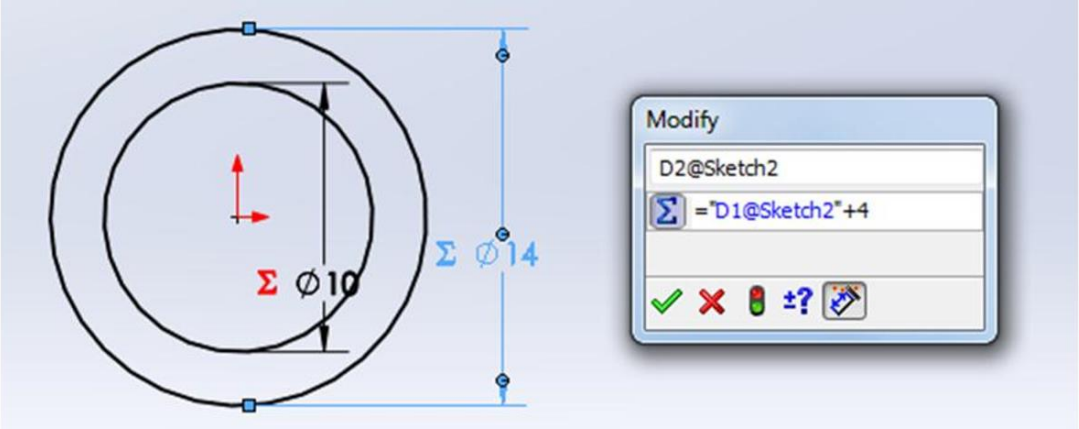

Fig B-21: Column wall sketch

After making the sketch, create a boss-extrude feature (Insert → Boss/Base → Extrude) and set the column height (40 mm in this case). Using the same sketch, accessed by clicking on the '+' sign next to 'Boss-Extrude 1', create another boss-extrude feature in the other direction and selecting the outer circle in the 'Selected Contours' option as shown in Fig B-22 b to create a column cap.

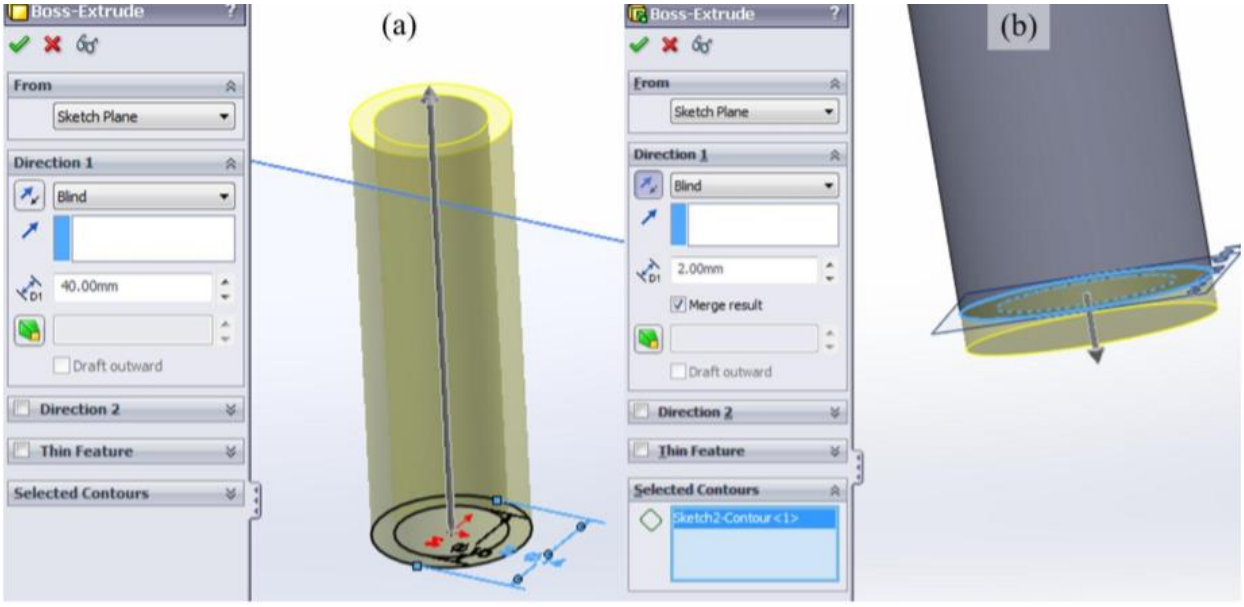

Fig B-22: Boss extrude to create (a) the column wall and (b) column cap

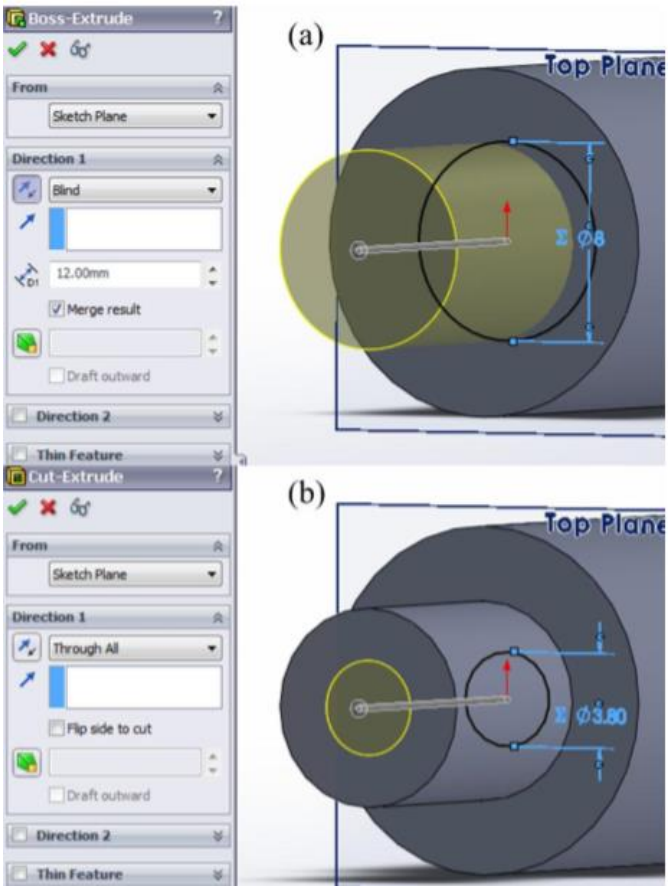

Fig B-23: Designing the column fitting with the (a) Boss-extrude and (b) Cut-extrude features

To create the fittings, we first create a boss-extrude. A diameter of 8 mm and extrude height of 12 mm are usually compatible with FPLC fittings and certain syringes for negative templating. We then create a fittinghole for the column feature from the top plane (Fig B-23 b). A diameter of 3.8 mm is compatible with commonly used 10-32 FPLC fittings.

We can then create a second cap by copying this file and use the cutextrude feature to remove the column wall.

It is worth noting that this casing does not contain any distributor branches, which can be designed using a combination of cut-extrude and revolved cut features.

B.2.8 Exporting Full Column .stl File

After creating the Solidworks assembly model of the full column, export the file as an .stl file; the most common file format used by 3D printers. To export the CAD model as an .stl, click File → Save As and select .stl as the file format. Before saving the file, open the export options window.

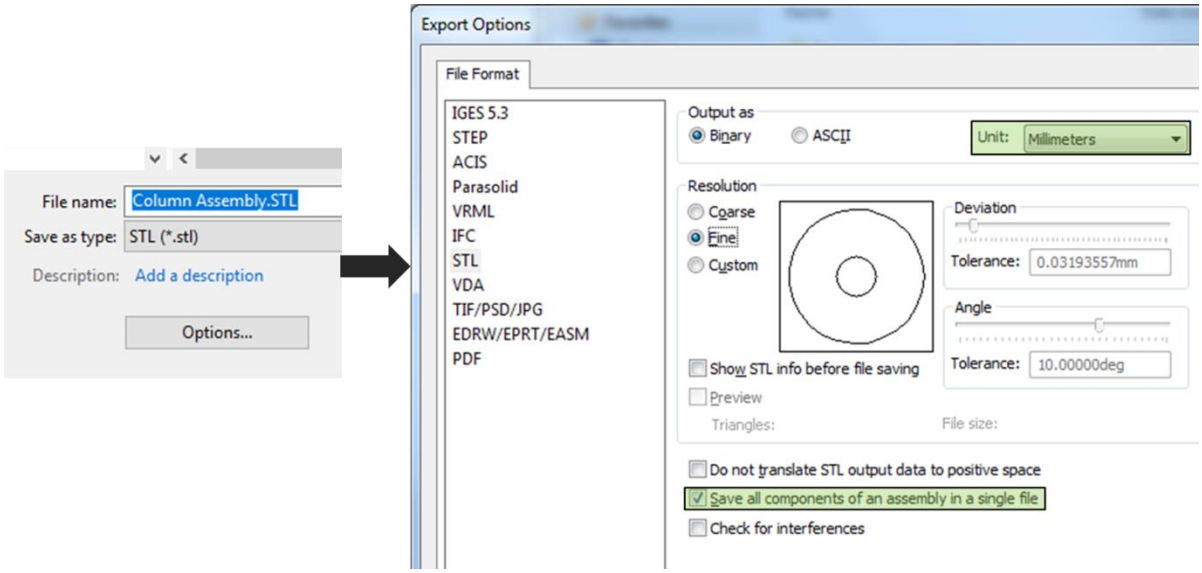

Fig. B-24: .stl export options

The two most important export options, highlighted in Fig. B-24 are the units (in this case: millimetres) and the option to save all components in a single .stl file. After choosing the two options, click OK and Save to create the .stl file.

Appendix C. Algorithms for Creating Cellular Automata

This subsection provides a general outline for creating the cellular automata structures discussed in Chapter 6.3. The entire set of functions to determine whether the final structure would conform to the listed constraints and calculating the number of connecting faces for solid and void voxels, surface area are not listed here. The most critical part of determining a suitable cellular automata structure is arriving at a rule-set that is suitable to producing favorable structures for liquid chromatography.

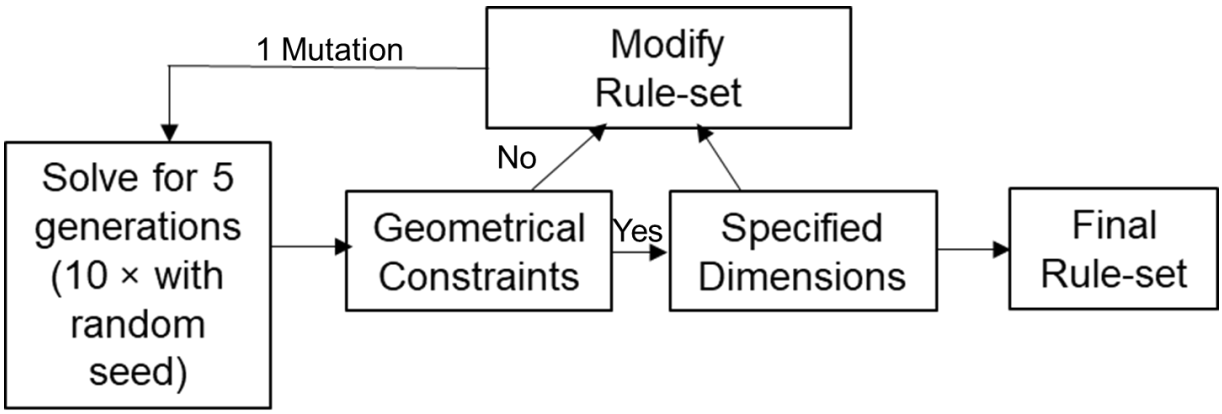

Fig C-1: Basic workflow of algorithm to choose cellular automata rule-set

A basic genetic algorithm was developed for arriving at a rule-set for a 2 × 2 input and output format as shown in Fig C-1. For a 2 × 2 format, 16 possible input and output conditions exist. These are numbered from 1-16 in Fig C-2 and inputs and outputs are paired to one another by paired lists. The final rule-set is therefore a list of pairings that produce structure that conform to the listed constraints as well as minimize the solid and channel characteristic dimensions. Figure C-2 shows the code for a random seed with the rule-set arrived at using the genetic algorithm described previously.

Rules

In[477]:=
```
bin = Tuples[{0, 1}, 4];
rules = Array[# &, {16, 2}];
rules = {{1, 6}, {2, 14}, {3, 15}, {4, 6}, {5, 8}, {6, 13}, {7, 14}, {8, 3},
   {9, 12}, {10, 13}, {11, 9}, {12, 2}, {13, 11}, {14, 4}, {15, 5}, {16, 11}};
Table[Table[ArrayPlot[ru[[rules[[n, m]]]], ImageSize → 20],
    {n, 1, Length[rules]}], {m, 1, 2}] // MatrixForm
```

Out[478]//MatrixForm=

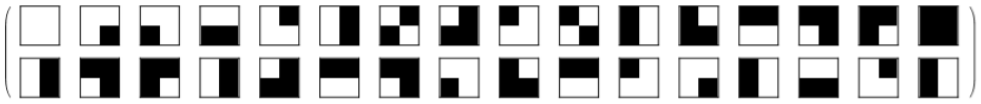

In[479]:=
```
tr = Array[# * 0 &, {h, w/2, 1/2, 4}];
tr[[1]] = Array[RandomInteger[] * (# - (# - 1)) &, {w/2, 1/2, 4}];
Table[nextgen[n], {n, 1, Length[tr] - 1}];
blist = Table[qua2[tr[[n]]], {n, 1, Length[tr]}];
```

Fig C-2: Example code displaying input (top) and output (bottom) conditions of 2 × 2 cells using a random seed